Electrical Characterization of Materials and Devices for Photovoltaic Applications

by

SEBASTIAN MIENIE

Submitted in partial fulfilment of the requirements for the degree

Magister Scientiae

In the Faculty of Natural and Agricultural Science

Department of Physics

University of Pretoria

Supervisor: Professor M. Diale

Co-Supervisor: Professor F. D. Auret

Declaration of Authorship

I, Sebastian Mienie declare that this dissertation, which I hereby submit for the degree Magister Scientiae in Physics at the University of Pretoria, is my own work and has not been previously submitted by me for a degree at this or any other tertiary institution.

Signature:…….

Date:……..

“The wise are mightier than the strong, and those with knowledge grow stronger and stronger.”

Proverbs 24:5

ACKNOWLEDGEMENTS

My sincere thanks to:

- My supervisor Prof. M. Diale for her guidance and inputs concerning the understanding of the results and her support in both financial and academic matters.
- My co-supervisor Prof. F. A. Auret for his inspiration and advice and discussions throughout the project.
- I would in particular like to thank Mr Johan Janse van Rensburg for his guidance in the Hall Effect automation program and understanding the practical setup and execution of the experiment.
- My fellow postgraduate students and colleagues for their encouragement, support and willingness to help throughout this project.
- The South African National Research Foundation (NRF) for their financial assistance during this study.
- The University of Pretoria for allowing me enabling environment for my curiosity
- My mother and fiancé for their continuous love and support throughout my studies.

ELECTRICAL CHARACTERIZATION OF MATERIALS AND DEVICES FOR PHOTOVOLTAIC APPLICATIONS

by

Sebastian Mienie

Supervisor: Prof. M. Diale

Co-Supervisor: Prof. F. D. Auret

SUMMARY

First discovered by E.T. Hall in 1879 [1], the Hall Effect is a phenomena that explains the behaviour of a material placed in a magnetic field and a current is allowed to flow through the material, producing an electric field. By measuring this electric field a transverse potential can be measured known as the Hall voltage and in turn be used to calculate the Hall coefficient. The Hall coefficient is then used to calculate the Hall mobility, the carrier density and resistivity of the sample. All these parameters are temperature dependent and their effect on the material is measured and observed in the Hall measurements experiment

In this project a LabVIEW program was designed and written, which automates Hall measurements and the temperature dependence accurately. In this project, a 25 to 300 K temperature range, a magnetic field of 0.5 T and a current of 1 mA were used throughout the temperature dependent Hall measurements (*TDH*) experiments. The inversion layer n-Si/PEDOT:PSS, solar cell, p- and n-type GaAs and the n-type Si were characterized using the TDH, current-voltage (*I-V*) and capacitance-voltage (*C-V*) measurements. The *I-V* and *C-V,* measurements were used to derive parameters to evaluate the solar cells. Using *I-V* data, we calculated the solar cell's fill-factor, efficiency, quantum efficiency, short circuit current, open circuit voltage and power. The *C-V* measurements were used to calculate the inversion phenomenon of the cell. In addition, the Schottky related-parameters of the dark current measurements were extracted from the *I-V* measurements. These are the ideality factor and the barrier height.

The TDH measurements at 300K for n-Si gave a carrier density, mobility and resistivity of $1.4\times 10^{14}\ \mathrm{cm}^{-3}$, 1400 $\mathrm{cm}^2(\mathrm{Vs})^{-1}$ and 20 Ohm.cm respectively. PEDOT:PSS was also studied and measured in this project with a carrier density, mobility and resistivity of 300 K of $9.7 \times 10^{21}\ \mathrm{cm}^{-3}$, 0.7 $\mathrm{cm}^2(\mathrm{Vs})^{-1}$ and 10^{-3} Ohm.cm respectively. The p and n-type GaAs measured mobilities of 100 $\mathrm{cm}^2(\mathrm{Vs})^{-1}$ and $25 \times 10^3\ \mathrm{cm}^2(\mathrm{Vs})^{-1}$, the carrier densities of $1 \times 10^{16}\ \mathrm{cm}^{-3}$ and $1.2 \times 10^{15}\ \mathrm{cm}^{-3}$ and finally the resistivities of 1.1 Ohm.cm and 0.2 Ohm.cm respectively. *I-V* measurements were also done using a $Oriel^{®}LCS-100^{TM}$ Small Area Sol1A solar simulator to evaluate the n-Si/PEDOT:PSS inversion layer solar cell. At an intensity of 1 sun measurements show an efficiency of 0.25 %, and fill factor of 57.33.

Contents

CHAPTER 1

INTRODUCTION

Electricity is one of the most important resources in today's age. Almost everything we own in some way requires electricity for operation. The average electrical power consumption in 2015 for South Africa alone was 25300 $MW.h.(yr)^{-1}$ [1]. For the past one hundred years, as the electrical power consumption increases, alternative methods to produce electricity has become not only a noteworthy science but a necessity. Another critical reason that renewable alternative methods to generate energy is such a crucial problem which needs to be solved in today's age is that the fuels that are used to generate most of the power used today are finite. This tell us that sooner or later these resources will run out and in the 21st century that problem is no longer something of the future by is a problem of our or the next generation. Many alternative methods and techniques have been made such as nuclear power plants, wind turbines, solar cell technology.

For the past 20 years photovoltaic technology has taken off with new techniques in design and production. An advantage of solar cell technology is the fact that they are environmentally friendly, there is no harmful waste and maintenance of some of these solar cell technologies are very cheap.

Since the 1950's silicon has been studied extensively for solar energy application because it absorbs in the visible range of the electromagnetic spectrum. It is also an abundant material on earth. The production cost of the silicon wafers used in the production of solar cells is very expensive since these devices requires high temperatures. But close to the 21st century with the advancements in science and technology many new solar cells have been discovered and developed, each bringing their own advantages and disadvantages. These new solar cells range from organic, thin film to dye sensitized solar cells. In this study, fabrication and characterization of an organic solar cell using ZnO and PEDOT:PSS, Inorganic/organic inversion layer using n-type Si and PEDOT:PSS and a perovskite solar cell was investigated. Methods such as spin coating and resistive vacuum deposition were employed in the fabrication of these solar cells.

Si solar cells limit our expectations in the generation of clean and cheap renewable energy. Si solar cell production requires high temperature techniques. These techniques are expensive and thus price per watt generated is high.

The characterization of the inversion layer solar cell and the materials used to produce them was done by using two methods. The first was the temperature dependent Hall Effect (*TDH*) measurement and the second was the current-voltage (*I-V)* measurements.

The temperature dependent Hall measurements are crucial to the understanding and characterization of the materials used to produce the solar cells because from these measurements the following parameters can be calculated or measured. These parameters include the resistivity (inverse of the conductivity), carrier concentration and mobility. This technique can also measure the effect of temperature on each of these parameters.

The *I-V* measurements are an essential part in the characterization of the final solar cell device. This technique can calculate important parameters of a solar cell, namely, the short circuit current, open circuit voltage, fill factor, shunt and series resistance and finally the efficiency of the solar cell.

1.1 MOTIVATION

Materials for solar cells have unique properties that makes them suitable for absorption of sunlight to create electricity. Each of these materials have resistivity and mobilities that affect their ability to conduct charge carriers. *TDH* is one method used to measure materials characteristics to understand charge transport.

1.2 AIM

The aim of this project was to design and program an automated temperature dependent Hall measurement system. Then using this system to characterize semiconductor and polymer materials.

1.3 OBJECTIVES

- To design and program an automated temperature dependence Hall measurement system.
- To measure *TDH* parameters of n-Si, n-and p-type GaAs, PEDOT:PSS and P3HT:PCBM
- Design and fabricate solar cells
- Measure *I-V* of the solar cells and extract solar cell parameters

1.4 LAYOUT OF DISSERTATION

- **Chapter 1** is an introduction to this study
- **Chapter 2** is dedicated to the theory of semiconductor materials for solar cells.
- **Chapter 3** discusses the types of solar cells studied in this project and parameters that are of importance for solar cell technology.
- **Chapter 4** is dedicated to the Hall Effect theory
- **Chapter 5** discusses the *I-V* characterization and techniques to characterize and investigate these solar cell and their materials.
- **Chapter 6** is dedicated to the experimental methods and theories which were used to characterize these solar cells.
- Finally the experimental results are discussed in **chapter 7**
- **Chapter 8** is dedicated to the conclusions of this project.

CHAPTER 2

SEMICONDUCTOR PROPERTIES

2.1 INTRODUCTION

When considering solid materials and their ability to conduct electricity, we can divide the materials in three groups: insulator, metal and semiconductors. In a solid material the atoms are close together and the bands overlap. The gap between the valence band and the conduction band is called the band gap. This is a discrete energy quantity that is required for an electron to be excited from the valence band to the conduction band, denoted E_g. The value of the band gap determines in which group the material falls under. Figure 2.1 offers a visual presentation of the differences of these types of solids.

2.1.1 Type of solids

1) Insulators

For a solid material to be an insulator, the band gap between the valance and conduction band should be very large such that to excite an electron from the valence band to the the conduction band requires a very large quantity of energy. The conductivity as low as 10^{-16} $(\Omega\text{cm})^{-1}$ has been measured for insulators [2].

2) Metals

Metals are well known conductors because of the arrangements of electrons in the valence/conduction band. The conduction and the valance bands of metals overlap, allowing electrons to move freely within the conduction and valance bands without additional energy. Furthermore, the conduction band can be partially filled with electrons which are free to move within the material. These electrons are known as conduction electrons. The conductivity of metals is very high and has been reported to be in the of range 10^6 $(\Omega\text{cm})^{-1}$

3) **Semiconductor**

A semiconductor is a kind of material which is a conductor at certain temperatures. In this type of material the valance band is full with electrons while the conduction band is empty, making their conductivities to range from 10^{-4} to $10^{4}\,(\Omega\text{cm})^{-1}$. Conductivity of a semiconductor is enhanced by addition of impurities known as dopands [3]. Dopants are added to the semiconductor material to allow the material to have either extra mobile electrons or holes. Due to their abundance and efficiency the three most important semiconductors are germanium (Ge), silicon (Si) and gallium arsenide (GaAs) with band gaps of 0.74 eV, 1.17 eV and 1.52 eV respectively at 0 K [9].

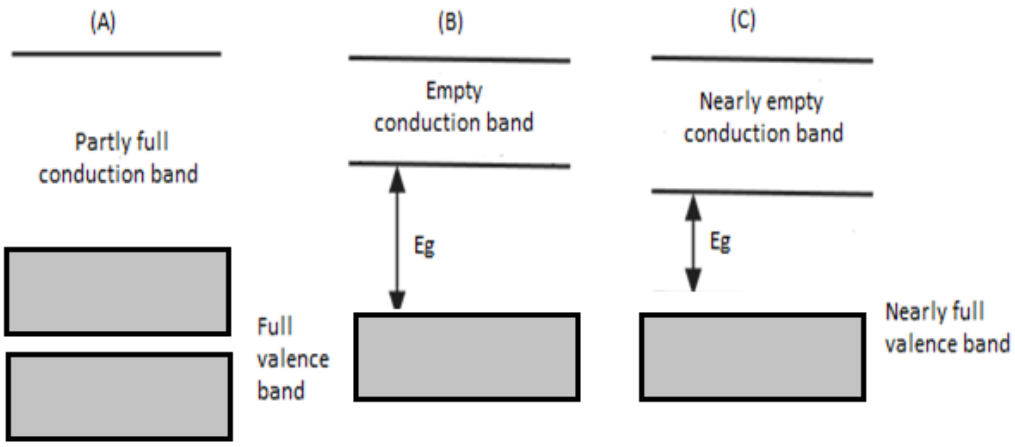

Figure 2.1: Simplified band diagram of a metal (A), insulator (B) and semiconductor (C).

2.2 PROPERTIES OF SEMICONDUCTORS

2.2.1 Crystal structure

Most semiconductors have diamond or zincblende lattice structures which have tetrahedral phase geometry. Ge and Si have a diamond structure and GaAs has a zincblende structure. Each atom in group are surrounded by four equidistant nearest neighbours, each lying at the corners of a tetrahedron. Figure 2.2 shows the zincblende and diamond lattice structures.

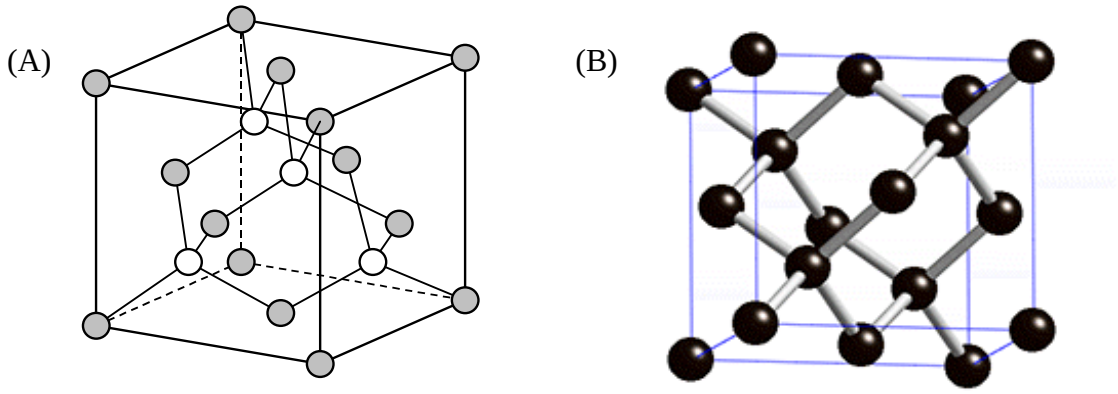

Figure 2.2: Zincblende (A) and diamond (B) lattice structure. The shaded sites are occupied by one type of ion, the unshaded by another type [9].

2.2.2 Energy gap

In semiconductors there are various energy regions above and below the band gap. The upper and lower bands are the conduction and valance bands respectively. The energy difference between the lowest conduction band and the highest valance band is known as the energy band gap E_g (Figure 2.3). This quantity is the most important parameter in semiconductor physics. The average band gap energies at room temperature under normal atmosphere are 0.66 eV for Ge, 1.12 eV for Si and 1.42 eV for GaAs at 300 K [3]. These values are for high purity materials.

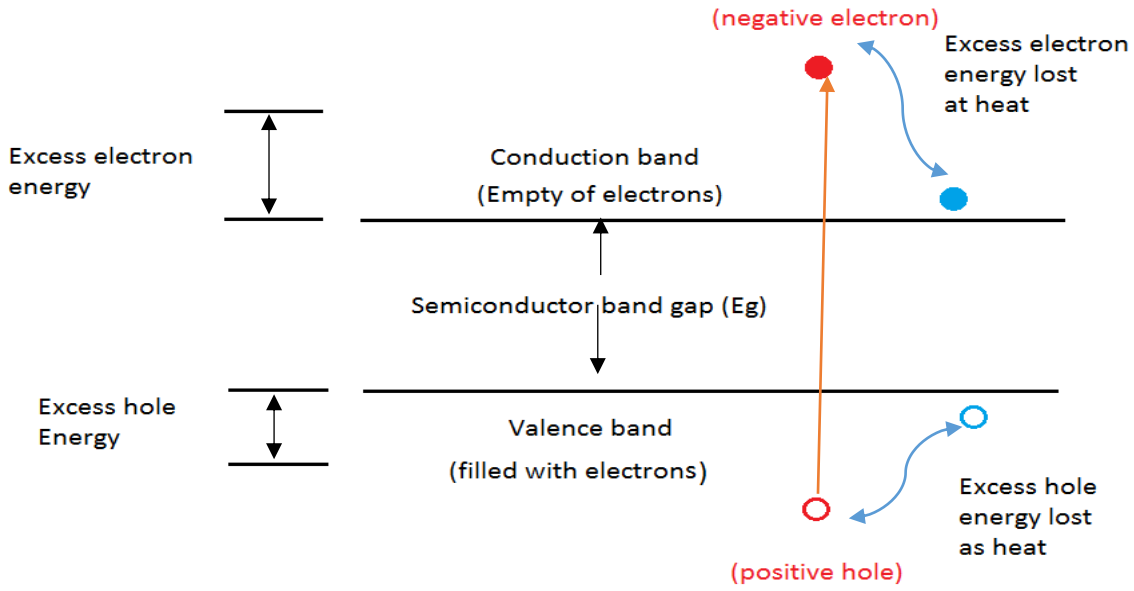

Figure 2.3: Simplified band diagram of a semiconductor material.

To obtain the band structure of a crystalline solid we need to solve the approximate one-electron Schrödinger equation [4].

$$\left[-\frac{\hbar^2}{2m}\nabla^2 + V(r)\right]\varphi_k(r) = E_k\varphi_k(r) \qquad 2.1$$

where m is the mass, ∇ is the partial derivative function and $\varphi_k(r)$ is the wave function of eigen-value k.

The Bloch theorem can be used as it states, if the potential energy $V(r)$ is periodic with the periodicity of the lattice, then the solutions to the Schrödinger equation are of the form

$$\varphi_k(r) = e^{jk.r}U_n(k,r) \qquad 2.2$$

where the term $U_n(k,r)$ is periodic and n is the band index. Using Bloch's theorem one can show that the energy is also periodic and thus $E_k = E_{k+G}$ where G is the general reciprocal lattice.

The energy band gap is also dependent on temperature. The relation between the band gap energy and temperature is given by the following formula [9]:

$$E_g(T) = E_g(0) - \frac{\alpha T^2}{(T+\beta)} \qquad 2.3$$

This shows that as the temperature increases the band gap energy of most semiconductors decreases. Using maple software a plot of the Energy band gap as a function of temperature was plotted, as shown by figure 2.4 for Si, Ge and GaAs [7].

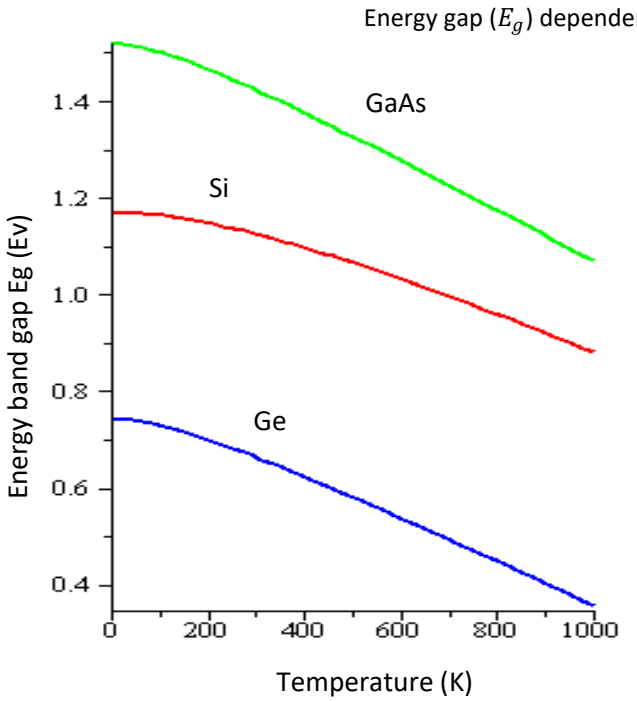

Material	Eg(0)	α (x10^-4)	β
Si	1.170	4.73	636
Ge	0.7473	4.774	235
GaAs	1.519	5.405	204

Figure 2.4: The dependence of the energy band gap on temperature for Si, Ge and GaAs plotted using maple software.

2.2.3 Carrier concentration

There are two types of semiconductors: intrinsic and extrinsic semiconductors. Extrinsic semiconductors are further divided into n-type (donor) and the p-type (acceptor) semiconductors.

1) Intrinsic semiconductors

The intrinsic semiconductor is a material that is considered pure because it contains negligible amounts of impurities. Within this type of material the number of electrons and holes are equal. The concentration of holes or electrons is called the intrinsic carrier concentration (n_i). The intrinsic carrier concentration is a function of the lattice temperature, which affects the energy of the electrons, causing them to vibrate, thus breaking the chemical bonds in the material. The intrinsic carrier concentration is also a function of the band gap energy which determines the amount of energy required to create electron-hole pairs [4]. The probability of an energy state with energy *E* being occupied by an electron in the conduction band is given by

$$f_e(E) = \frac{1}{[1+e^{(\frac{E-E_F}{kT})}]} \quad 2.4$$

where *k* is the Boltzmann constant, *T* is the temperature and E_F is the Fermi energy(see section 2.2.4). The probability of an energy state with energy *E* being occupied by a hole in the valance band is given by

$$f_h(E) = 1 - \frac{1}{[1+e^{(\frac{E_F-E}{kT})}]} \quad 2.5$$

we can approximate these Fermi-Dirac distribution functions by the Maxwell-Boltzmann formula to obtain

$$f_e(E) \approx e^{(\frac{-(E-E_F)}{kT})} \quad \text{for } E > E_F \quad 2.6$$

$$f_h(E) \approx 1 - e^{(\frac{-(E_F-E)}{kT})} \quad \text{for } E < E_F \quad 2.7$$

Using these formula the number of occupied conduction band states can be calculated and using the density of states, the concentration of electrons in the conduction band and holes in the valance band is given by

$$n = N_c e^{(\frac{-(E_c-E_f)}{kT})} \quad 2.8$$

$$p = N_v e^{(\frac{-(E_f-E_v)}{kT})} \quad 2.9$$

where N_c *is* the effective density of states in the conduction band and N_v is the effective density of states in the valance band. E_c is the energy at the bottom of the conduction band and E_v is the energy at the top of the valance band. Due to the temperature of the material, continuous vibration occurs, resulting in electrons being excited from the valence band to the conduction band, creating electron-hole pairs [7]. When an intrinsic semiconductor is in equilibrium then the following occurs

$$n_i = n = p \tag{2.10}$$

which results in

$$n_i^2 = np \tag{2.11}$$

$$n_i^2 = N_v N_c e^{(\frac{E_v - E_c}{kT})} \tag{2.12}$$

$$n_i = (N_v N_c)^{\frac{1}{2}} e^{(\frac{E_v - E_c}{2kT})} \tag{2.13}$$

where $E_v - E_c = -E_g$ and E_g is the band gap energy. Thus thermal vibration is the dominant process of carrier generation since as the temperature is increased so does the intrinsic carrier density increase.

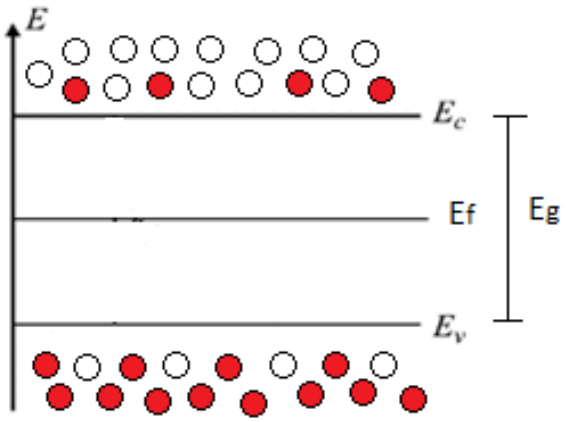

Figure 2.5: The energy band structure of an intrinsic semiconductor with the Fermi energy approximately in the middle and the electron and hole concentration are equal [9,12].

2) Extrinsic semiconductors

An n-type semiconductor has many impurities where the impurity atoms have more valance electrons than the primary material. Thus there are free electrons within the semiconductors known as donor atoms. A p-type semiconductor has many impurities where the impurity atoms in the material have less electrons in their valance band as the primary material. Consider Si as an example. To form n-type Si, the material is doped with phosphorus (P). As phosphorus has 5 valance electrons and Si has 4, doping results in an excess of electrons, which form an n-type Si. To form p-type Si an element such as boron is typically used as it has 3 valance electrons thus if B is doped into Si there is an excess of holes occurring, resulting in a p-type Si.To form one of these extrinsic types of semiconductors the material must be doped with the right impurity. When a semiconductor is doped with an impurity then impurity energy levels are formed just below the conduction band in n-type and just above the valance band for p-type materials, as shown in figure 2.6

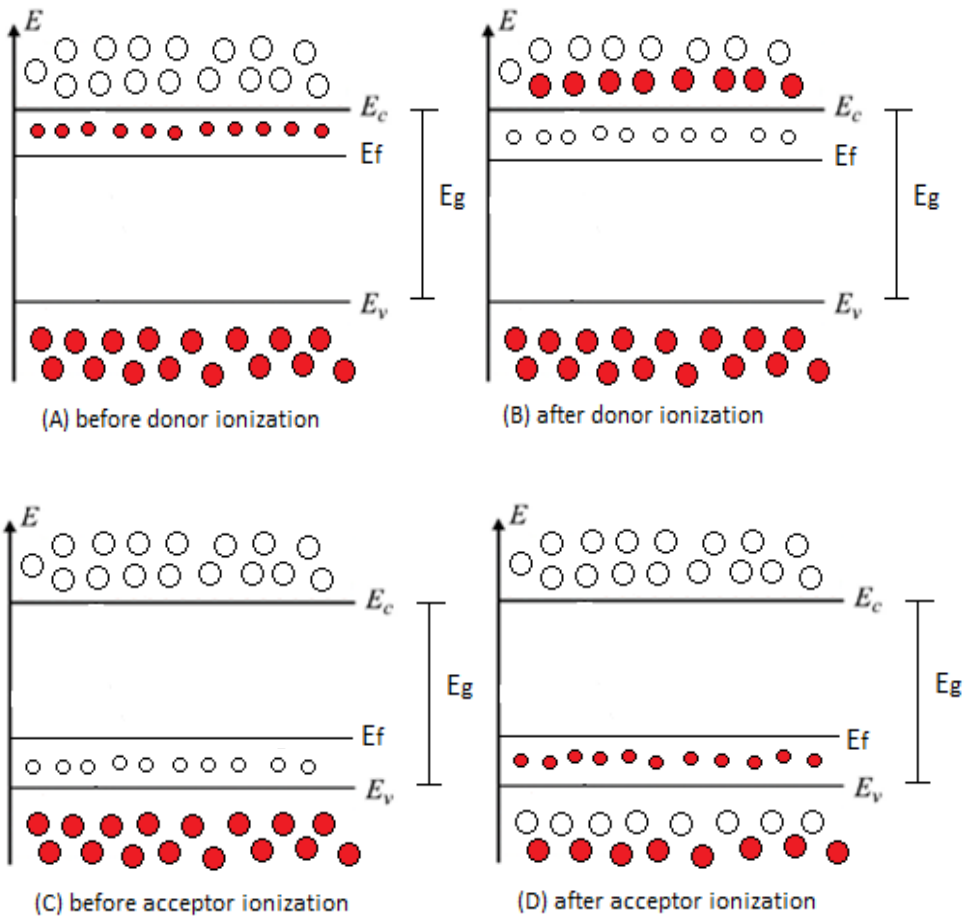

Figure 2.6: The energy band structure of an n-type semiconductor (A,B) and p-type semiconductor (C,D) [9,12].

2.2.4 The Fermi energy

The Fermi energy, denoted $\boldsymbol{E_F}$, is the highest filled electron energy level at absolute zero. It can also be seen as the energy for which the probability of occupation of the energy state by an electron is equal to exactly half. The Fermi energy is different for each type of semiconductor. For an intrinsic semiconductor the Fermi level is approximately in the middle of the band gap energy. In the presence of impurities, the Fermi level must adjust itself so that charge neutrality in the material is preserved, according to either n- or p-type material. For an n-type material there are more electrons present than holes thus the Fermi level will be closer to the conduction band compared to the valance band. For a p-type semiconductor the Fermi level will be closer to the valance band compared to the conduction band. As shown if figure 2.7.

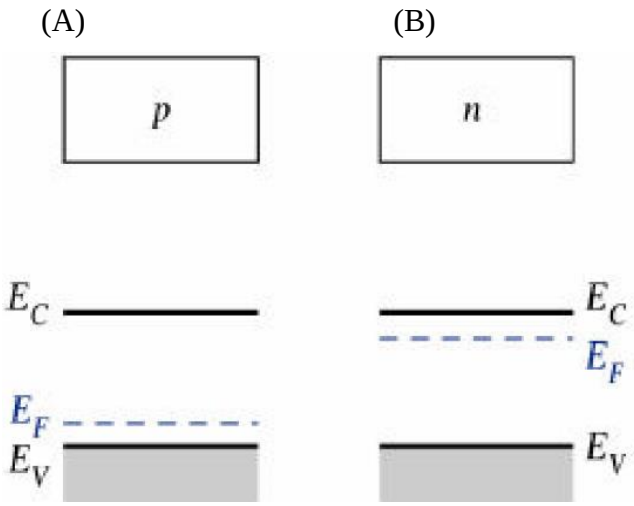

Figure 2.7: The Band diagram depicts the shift in the Fermi energy for a p-type semiconductor (A) and an n-type semiconductor (B) [7].

2.2.5 Resistivity

The resistivity is the proportionality constant between the electric field and the current density given by the following

$$E = \rho J \tag{2.14}$$

where E is the electric field, J is the current density and ρ is the resistivity. For a semiconductor the resistivity can be written as

$$\rho = \frac{1}{e(n\mu_n + p\mu_p)} \tag{2.15}$$

It is however more convenient to write the resistivity in terms of the conductivity σ where the conductivity is the reciprocal of the resistivity [7,8]. We can then write the conductivity as

$$\sigma = \frac{nev}{E} \tag{2.16}$$

where E is the electric field and v is the velocity and n is the carrier density and e the electron charge. Equation 2.16 is valid when Ohm's law is assumed (Ohm's law is defined by the $V=IR$). Since Ohm's law holds, the resistance of the material is constant. This leads to the conductivity being independent of the electric field E**,** given by the relation.

$$\sigma = ne\mu \tag{2.17}$$

where μ is the mobility of the charge carriers.

2.2.6 Mobility

The mobility influences the behaviour of the devices through its frequency response in two ways. The first way is that the carrier drift velocity is proportional to the mobility for low electric fields.

$$v_d = \mu E \tag{2.18}$$

where v_d is the drift velocity, E is a low electric field and μ is the mobility [9]. For materials with higher mobility, a higher frequency response will be measured. This is because the carriers

take less time to travel through the material. The second way is that the current of the material is dependent on the mobility, resulting in higher current in the material with higher mobility. There are several mobility's in use. The mobility quantity measured in this project is the Hall mobility. Three types of mobilities are discussed below.

1) Microscopic mobility

If we consider an n-type semiconductor with a uniform donor concentration. In the absence of an applied electric field the electrons will undergo a random thermal motion within the material and will only be interrupted by collisions with each other. After a long period of time there will be no net displacement of the electrons as shown in Figure 2.8 (A) When an electric field is applied the electrons will drift in the opposite direction, resulting in a net electric current in the material. Thus there is a net displacement of the electrons within the material as shown in Figure 2.8 (B).

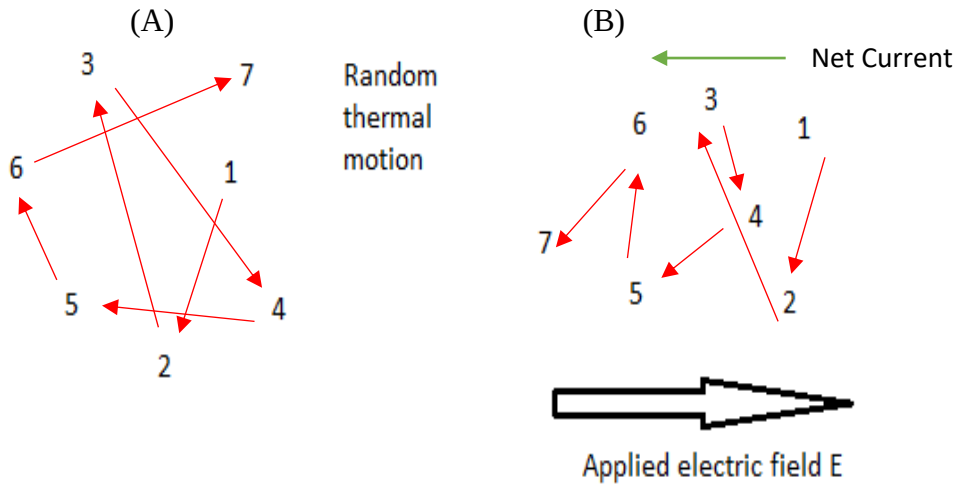

Figure 2.8: The motion of electrons in a crystal structure with no applied field (A) and applied electric field (B) resulting in a net current [7].

If it is assumed that the collisions of the electrons are random, the drift velocity v_d at a time t is given by

$$v_d(t) = at \qquad 2.19$$

and using Newton's second law to solve for the magnitude of the acceleration *a* in the above equation we obtain the following:

$$a = \frac{eE}{m^*} \tag{2.20}$$

where t_{coll} the time average between collisions and m^* as the effective mass, *E* is the electric field, *e* is the elementary charge. The effective mass is defined as the mass that a particle seems to have when responding to forces. Within these calculation the forces acting on the electrons are from the electric and magnetic fields. This results in

$$F = qE = ma \tag{2.21}$$

where $q = e$ is the elementary charge of an electron. This equation represents the force experienced by a charge in the presence of an electric field E. With these quantities the average drift velocity of the electrons is:

$$v_e = et_{coll}\frac{E}{m^*} \tag{2.22}$$

and the electron mobility is

$$\mu_e = \frac{v}{E} \tag{2.23}$$

$$= \frac{et_{coll}}{m^*} \tag{2.24}$$

the mobility is thus defined as the velocity per unit strength [8]. It can be deduced from this equation that the smaller the effective mass and the longer the time between collisions, the higher the mobility.

2) Conducting mobility

The conduction of a semiconductor with both electron and hole carriers is given by the following

$$\sigma = e(n\mu_n + p\mu_p) \tag{2.25}$$

where for an n-type semiconductor n >> p and the conducting mobility is given by

$$\mu_n = \frac{\sigma}{en} \tag{2.26}$$

and for a p-type material p>>n with a conducting mobility given by

$$\mu_p = \frac{\sigma}{ep} \tag{2.27}$$

3) Hall mobility

The Hall mobility is defined as follows [8]:

$$\mu_H = \frac{|R_H|}{\rho} = |R_H|\sigma \tag{2.28}$$

where R_H is the Hall coefficient. The Hall mobility differs to the conduction mobility since

$$\mu_H = r\mu_p \quad \text{and} \quad \mu_H = r\mu_n \tag{2.29}$$

for extrinsic p-type and n-type semiconductors [7]. These relations are derived in chapter 4.

2.3 METAL-SEMICONDUCTOR CONTACTS

2.3.1 Introduction

When there is an interface between a metal and a semiconductor, two important cases arise namely, the Schottky barrier and ohmic contacts. When the work function, $q\varphi_s$ of the n-type semiconductor material is lower than the work function, $q\varphi_m$ of the metal then a Schottky barrier is formed. If the n-type semiconductor work function is higher than the metal work function an ohmic contact will form. In this section the Schottky barrier for an n-type semiconductor metal interface, the factors that affect the Schottky barrier height (SBH) and the ohmic contacts will be discussed.

For an n-type metal semiconductor contact Schottky barrier is presented by [13]:

$$q\varphi_m > q\varphi_s \rightarrow \text{Schottky barrier}$$

$$q\varphi_m < q\varphi_s \rightarrow \text{Ohmic contact}$$

for a p-type metal semiconductor interface we have: [13]

$$q\varphi_m > q\varphi_s \rightarrow \text{Ohmic contact}$$

$$q\varphi_m < q\varphi_s \rightarrow \text{Schottky barrier}$$

2.3.2 Schottky barrier

When a metal is in contact with a semiconductor, a barrier is formed at the interface of the two materials. This barrier is known as the Schottky barrier and acts as a diode. At thermal equilibrium, the Fermi levels of these materials must be coincident, resulting in band bending.

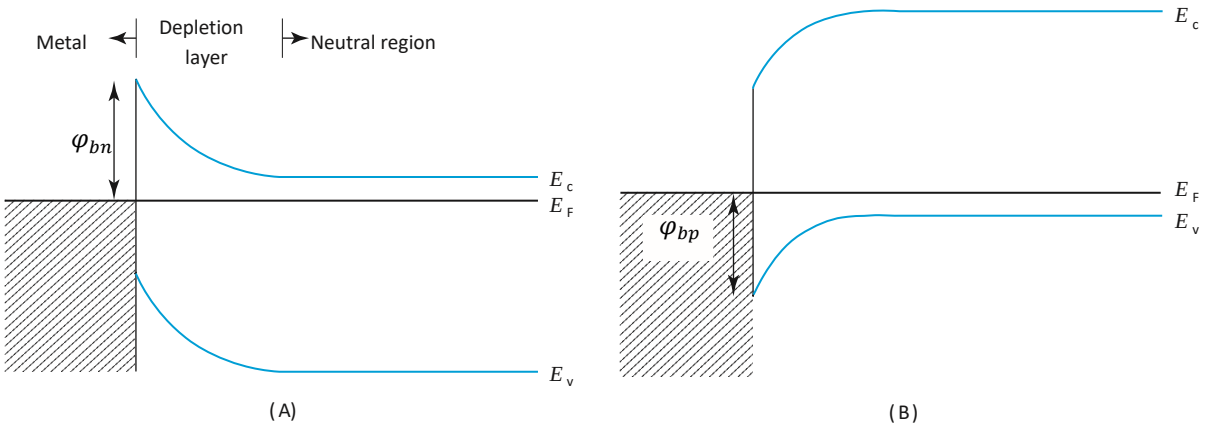

Figure 2.9: Energy-band diagram between a semiconductor and metal. φ_{bn} is the barrier height against the flow of electrons from the metal to the semiconductor(A). φ_{bp} is the barrier height against the flow of holes between the metal and semiconductor(B) [13].

Consider the case where the metal and semiconductor are at ideal contact in the absence of the surface states. When the metal and n-type semiconductor material are in contact such that the electrons will flow from the semiconductor to the metal at thermal equilibrium the Fermi levels of the two material will coincide [8]. The Fermi level of the semiconductor material will lower

by the amount equal to the difference between the two work functions of the metal and semiconductor. The work function of a material is the energy difference between the Fermi and vacuum level (The minimum energy required to remove an electron from the solid). The work function of a metal is given by:

$$q\varphi_m \tag{2.30}$$

where φ_m is in volts and for a semiconductor material the work function is:[7]

$$q\varphi_s = q(\chi_s + V_n) \tag{2.31}$$

where qV_n is the energy difference between the conduction band and the Fermi level and qx_s is the electron affinity, the energy measured from the conduction band to the vacuum band. The contact potential is then given by

$$q\varphi_m - q(\chi_s + V_n) \tag{2.32}$$

As the distance between the two materials decreases, an increase in negative charge is built up at the metal surface and an equal and positive charge exist in the semiconductor. Due to the low carrier concentration the positive charge is distributed over a barrier region near the semiconductor surface [8]. The band bending at the interface between the semiconductor and metal establishes a Schottky barrier height for electrons given by

$$\varphi_{bn} = \varphi_m - \chi_s \tag{2.33}$$

and the hole barrier height for a n-type semiconductor and metal contact is given by

$$q\varphi_{bp} = E_g - q(\varphi_m - \chi_s) \tag{2.34}$$

where E_g is the band gap of the semiconductor material. The energy-band diagram of such a contact is given by figure 2.10.

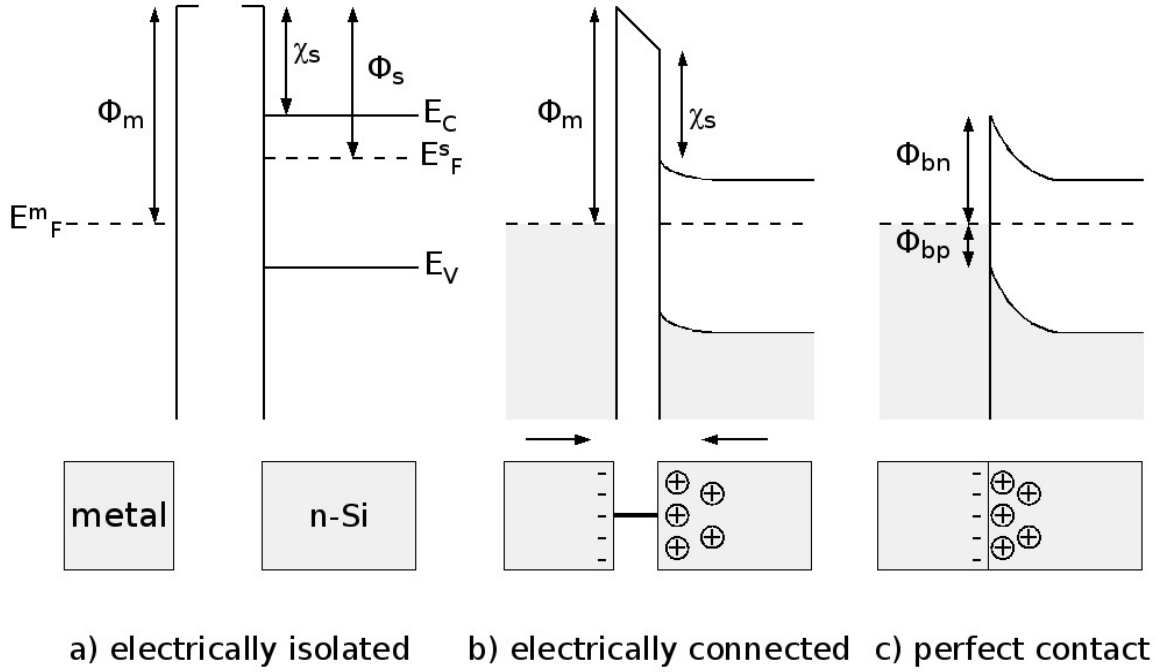

Figure 2.10: Energy-band diagram of metal n-type semiconductor contact a) electrical isolation b) electrical connected with some separation and c) perfect contact [9].

In figure 2.10 a) with the metal on the left and the n-type semiconductor on the right, isolated from each other. At this stage, Fermi energy level of the semiconductor is higher than that of the metal thus electrons in the semiconductor have more energy than those in the metal. The electrons with a higher energy seek a lower energy state to become stable and thus they tunnel into the metal to obtain this lower energy state. As the concentration of the electrons decrease in the semiconductor the Fermi level is reduced until the two Fermi levels of the semiconductor and metal align shown by figure 2.10 b. The electrons in the metal repel the electrons in the semiconductor further away from the interface and leaves positive ions near the interface as shown in figure 2.10 c [9].

The Schottky barrier can be altered in shape and height by the Schottky effect. Figure 2.10 shows the creation of the Schottky barrier when no voltage is applied, however when a voltage is applied on the Schottky barrier junction the electrostatics change. The height and shape of the barrier changes and these changes are illustrated in figure 2.11 [13]:

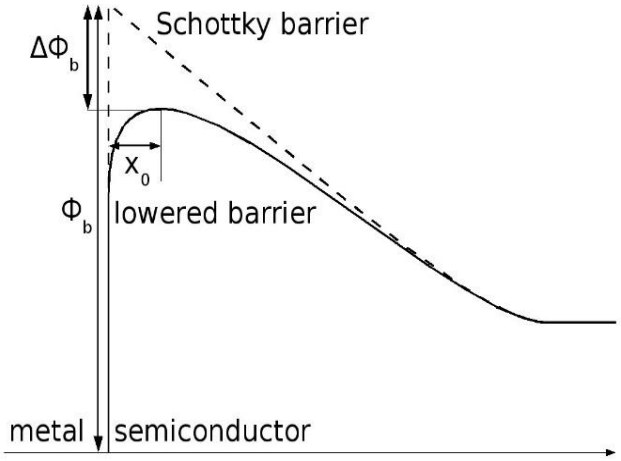

Figure 2.11: The Schottky effect on the Schottky barrier. The initial barrier (dotted line) and effective barrier (solid line) [13].

The two factors that contribute to the Schottky effect (lowering of the Schottky barrier) are the image force lowering and dipole lowering. These factors affect the carrier transport at the semiconductor-metal interface since it reduces the barrier height and in turn increases the carrier transport from one material to the other over the lowered barrier.

Image force lowering of the Schottky barrier arises when an electric field is applied to the semiconductor metal interface. Consider the following example. An electron with a charge $-q$ is located a distance x from the metal surface in the semiconductor material establishes electric field lines that terminate on the metal surface. These lines behave in such a way that there is a positive charge $+q$ located a distance of $-x$ from the metal surface (the mirror image of the electron charge). The force acting on the electron in the semiconductor material is the same as if the metal surface were replaced by an image charge of value $-q$ at a distance $-x$. Using Coulomb's force the amount at which the barrier is lowered is given by [13]:

$$\Delta\varphi = \sqrt{\frac{qE_{app}}{4\pi\varepsilon_s}} \qquad 2.35$$

where E_{app} is the applied electric field and ε_s is the permittivity of the semiconductor, and the lowering of the barrier is in volts. The position of the maximum of the barrier in cm is given by [13]:

$$\chi_m = \sqrt{\frac{q}{16\pi\varepsilon_s E_{app}}} \qquad 2.36$$

From equation 2.35 and 2.36 we note that as the applied electric field is increased, the barrier height is decreased and the position of the maximum of the barrier moves closer to the metal surface.

Experimentally it is observed that the image force lowering is sometimes not sufficient to explain the lowering of the Schottky barrier. The presence of a dipole layer at the intimate metal-semiconductor interface is responsible for the additional lowering of the barrier. The wave functions of electrons in the metal penetrate into the semiconductor and form metal induced gap states, which form a static dipole layer at the metal-semiconductor interface. This static dipole layer causes the barrier height to decrease approximately linearly with the electric field [13].

2.3.3 Ohmic contact

An ohmic contact is defined as a metal-semiconductor contact which has a negligible contact resistance compared to the bulk. A good ohmic contact should not significantly perturb the device performance and limit the flow of majority carriers between the two materials. There are two ways to form an ohmic contact. To form an ohmic contact a system must be chosen such that $q\varphi_m < q\varphi_s$ for an n-type semiconductor and $q\varphi_m > q\varphi_s$ for a p-type semiconductor. The second way is to dope the semiconductor heavily enough to allow tunnelling [13].

2.3.4 Conduction mechanism for metal-semiconductor contact

There are two emission mechanisms that occur in the conduction of electrons between the metal and semiconductor. The first is the thermionic emission which occurs when the depletion region is so wide that the only way that the electrons can overcome the potential barrier is by emission of the barriers maximum height (Figure 2.12 a).The thermionic emission mechanism dominates when the doping concentration is low in the semiconductor material. The second mechanism is the field emission where the carriers tunnel through the potential barrier. This is a result of the high doping concentration in the semiconductor material (Figure 2.12 c), for highly doped materials the field emission mechanism dominates.

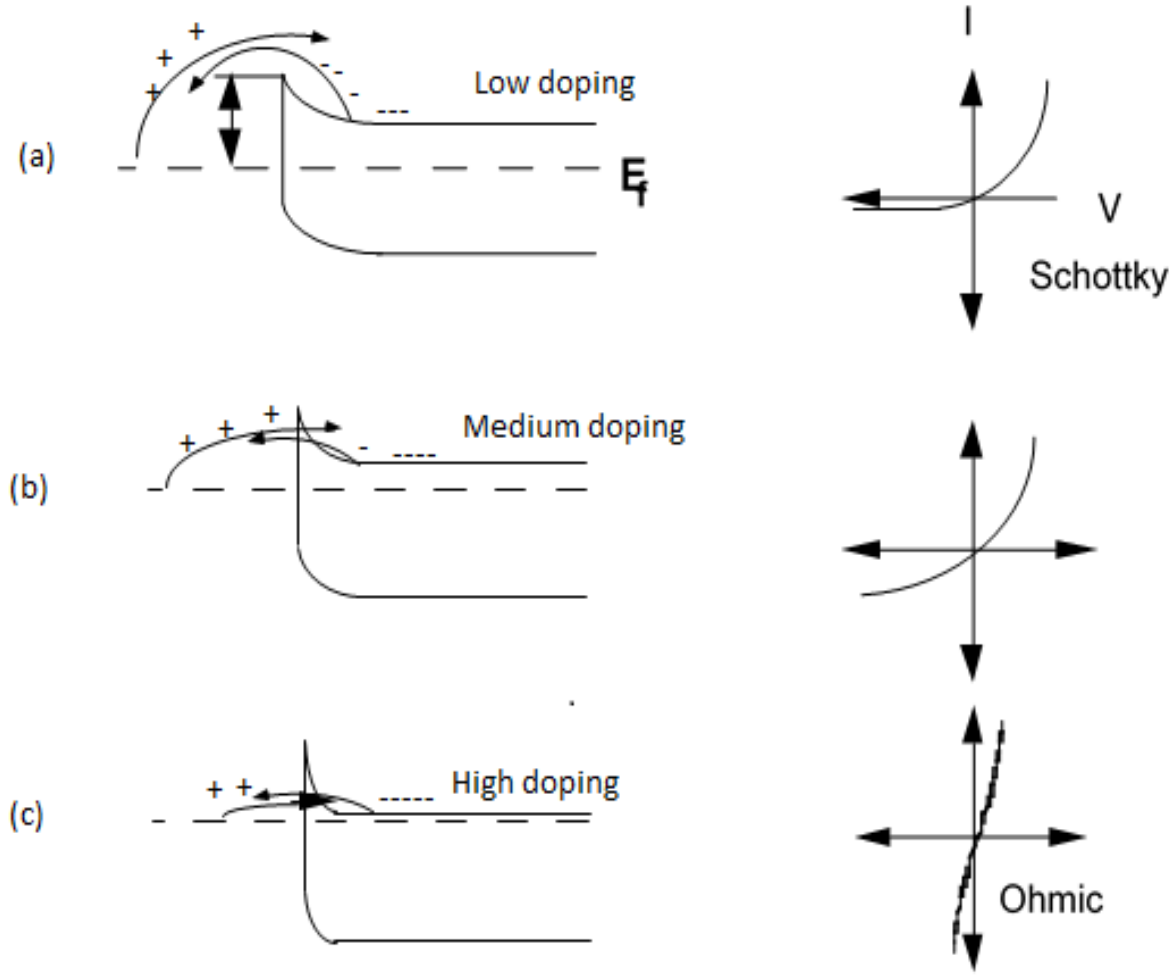

Figure 2.12: Basic illustration of conduction mechanisms for metal n-type semiconductor contact. (a) Thermionic emission (b) Thermionic-field emission (c) Field emission [18].

2.4 p-n JUNCTION DIODE

2.4.1 Introduction

A p-n junction is a two-terminal device which depends on the doping of the material, the device geometry and biasing condition. The theory of p-n junction is very important in optoelectronic applications. [9]. In this section we will discuss two important relations which contain information required for the characterization of the electrical properties of diodes. First is the depletion-layer capacitance, which contains a direct relationship to the impurity concentration. The second is the current-voltage characteristics, which is related to the diode's ideality factor, series resistance and reverse leakage current. In the case of photodiodes like the solar cell, the current-voltage measurements explains how the efficiency is affected by the ideality factor, series resistance and reverse leakage current.

2.4.2 Depletion-layer capacitance

The depletion-layer width for a one sided abrupt junction at thermal equilibrium is given by the following formula

$$W = \sqrt{\frac{2\varepsilon_s}{qN_B}(V_{bi} - \frac{2kT}{q})} \tag{2.37}$$

and the capacitance per unit area is given by

$$C = \frac{dQ_c}{dV} = \frac{\varepsilon_s}{\sqrt{2}L_D}(\beta V_{bi} \mp \beta V - 2)^{-\frac{1}{2}} \tag{2.38}$$

where dQ_c is the change in charge per unit area as a result of an incremental change in voltage. V_{bi} is the built-in potential and the plus-minus sign is determined by the forward-reverse bias conditions. L_D is known as the Debye length, which is a characteristic length for semiconductors. The Debye length is defined by:

$$L_D = \sqrt{\frac{\varepsilon_s}{qN_B\beta}} \tag{2.39}$$

Equation 2.39 can be used to obtain the impurity concentration of the substrate by plotting

$$\frac{1}{C^2} = \frac{2L_D^2}{\varepsilon_s^2}(\beta V_{bi} \mp \beta V - 2) \qquad 2.40$$

as a function of voltage (V) and related to the impurity concentration (N_B) by the following relation [9]:

$$\frac{d(\frac{1}{C^2})}{dV} = \frac{2}{q\varepsilon_s N_B} \qquad 2.41$$

2.4.3 Current-Voltage characteristics

The current-voltage measurements are used to extract information about the diode and its properties. By applying a forward bias, and plotting the logarithmic current (log (I)) as a function of voltage (V), quantities such as the ideality factor (n) and Schottky barrier height (SBH), can be extracted. The ideality factor indicates how close the diode is to the ideal case as will be discussed in section 5.2.6. The effect of the series resistance can also be examined from the current-voltage plot [22].

When the diode is forward biased very little current will flow through at the beginning as a result of the external voltage being opposed by the internal barrier of the diode. This internal voltage barrier is approximately 0.7 V for Si. As soon as this internal voltage is overcome then the current increases exponentially.

When the diode is in reverse bias the majority charge carriers are blocked and only current due to the minority charge carriers flow through the diode. As the voltage increases from zero the current reaches its saturation at a fast rate; this current is known as the leakage current [4]. The current-voltage (I-V) characteristics will be discussed further in chapter 5.

2.4.4 Formation of p-n junction

A p-n junction is formed by bringing two different types of materials together: n- and p-type materials. When contact between these two is established, a very large difference in the electron concentration exist, since an n-type material has an excess of mobile electrons and a p-type material has excess of holes. These differences in the concentration of charged carriers causes a diffusion of holes from the p-type to the n-type material and similarly the diffusion of

electrons from the n-type to the p-type material. The result of this diffusion process is a region close to the interface between the two materials becoming almost completely depleted of mobile charge carriers [4]. This gradual depletion of the charge carriers gives rise to a space charge region (SCR) created by the ionized donor and acceptor atoms that are not compensated by the mobile charges any more [4].

The region of space charge is known as the depletion region. The regions outside the depletion width, where charge neutrality is conserved are known as the quasi-neutral regions. The quasi-neutral regions gives rise to an internal electrical field. The internal electrical field forces the charge carriers to move in the opposite direction to the concentration gradient. This continues until the concentration gradient and the internal electric field compensate each other and resulting in no net current flowing through the p-n junction.

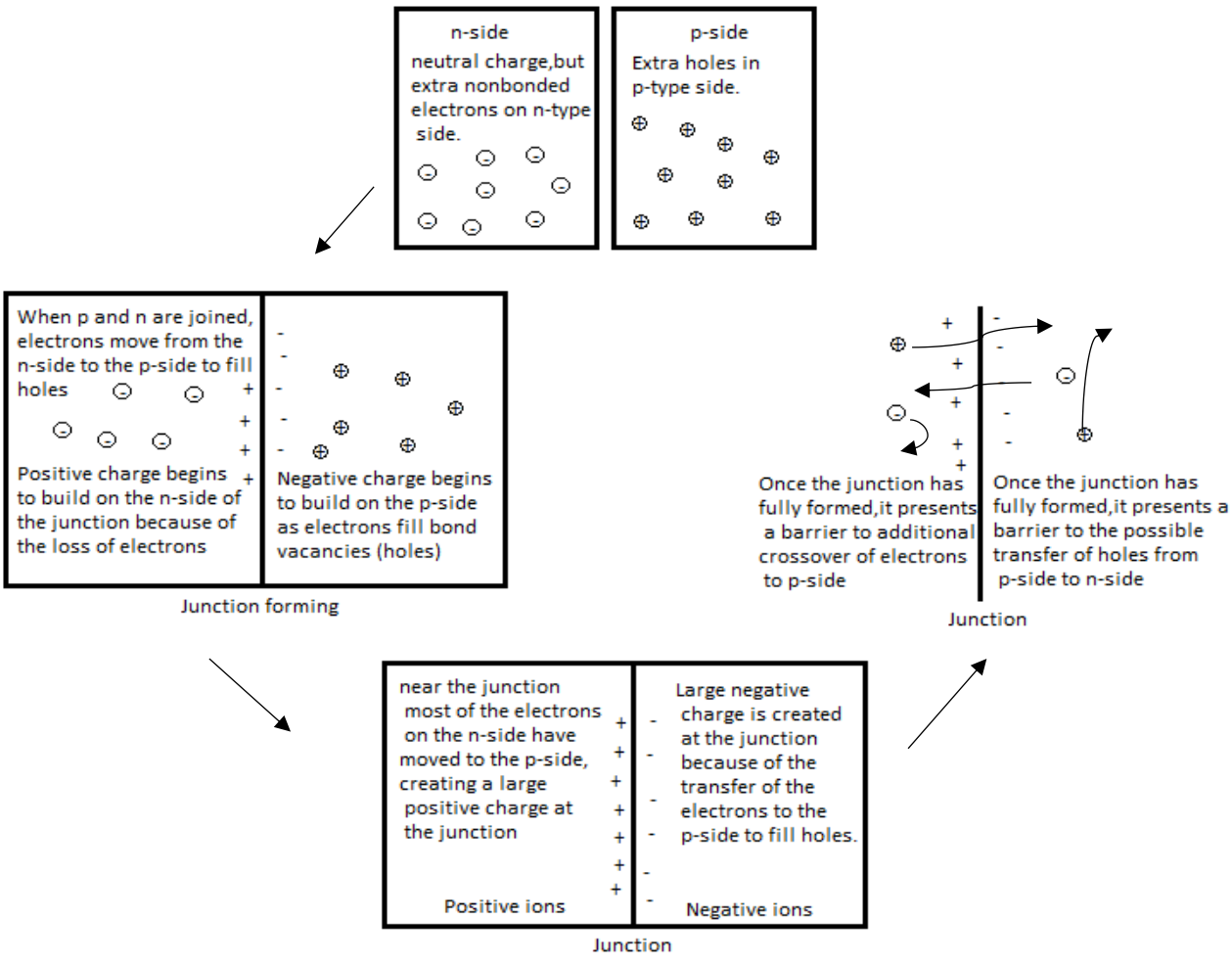

Figure 2.13: This diagram illustrates the formation of the p-n junction.

2.4.5 p-n Junction under equilibrium

The p-n junction represents a system of charged particles which are in diffusive equilibrium such that the electrochemical potential is constant and independent of position. Electrochemical potential is described by the Fermi energy, which is the representation of the average energy of electrons. Under equilibrium conditions the Fermi energy E_F has a constant position in the energy band diagram of the p-n junction. The energy difference between the conduction and valance bands, and the position of the Fermi level does not change in the quasi-neutral regions. Within the depletion region the valence and conduction bands line up between the n-type and p-type material. The curvature of these energy bands indicate the presence of an internal electrical field. The internal electrical field gives rise to a difference in the electrostatic potential between the boundaries and the depletion region [22].

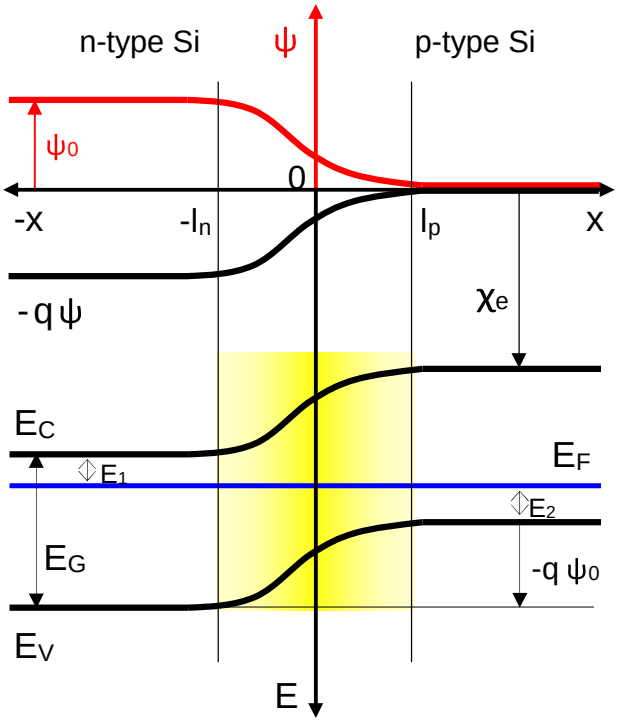

Figure 2.14: Illustration of the energy-band diagram of a single p-n junction. The electrostatic potential profile is also indicated by the red curve [4].

In figure 2.14 the yellow region indicates the depletion region, clearly indicating, that within the depletion region the changes in the carrier concentration are compensated by the changes within the electrostatic potential.

2.4.6 p-n Junction under Illumination

When a p-n junction is illuminated additional electron-hole pairs are generated within the semiconductor material. The concentration of the minority charge carriers (holes for n-type materials and electrons for p-type materials) increase at a large rate. This increase in these concentrations leads to the flow of the minority carriers across the depletion region into the qausi-neutral regions. Holes flow from the n-type into the p-type region and electrons flow from the p-type into the n-type region.

This flow of the photo-generated carriers cause the photo-generated current J_{ph} which adds to the thermal-generation current, J_{gen}. The open-circuit condition is obtained when there is no external contact between the n-type and p-type regions and no net current can flow inside the p-n junction, according to the following equation:.

$$J(V_a) = J_{rec}(V_a) - J_{gen}(V_a) - J_{ph} \qquad 2.42$$

The current resulting from the flux of photo-generated and the thermally-generated carriers has to be balanced by the opposite recombination current, J_{rec} , as indicated by the above formula. The recombination current will increase through lowering of the electrostatic potential barrier across the depletion region. Under non-equilibrium conditions the concentration of holes and electrons are described by the qausi-Fermi energy levels. The electrochemical potential for electrons is higher in the n-type region than that within the p-type region by an amount of qV_{oc}. When the n-type and p-type regions are short-circuited, with the sample under illumination, the photo-generated current flows through the external circuit. Under the short-circuit conditions the electrostatic-potential barrier does not change. However, from the strong variation of the quasi-Fermi levels within the depletion region one can determine that there is current flowing through the semiconductor [22].

When the p-n junction is illuminated and a load is connected between the electrodes only a fraction of the photo-generated current will flow through the external circuit. At the interface between the p-type and n-type regions the electrochemical potential will be lowered by a voltage drop over the load which in turn lowers the electrostatic potential within the depletion region. This results in the increase in the recombination current. The total net current is then given by equation 2.42.

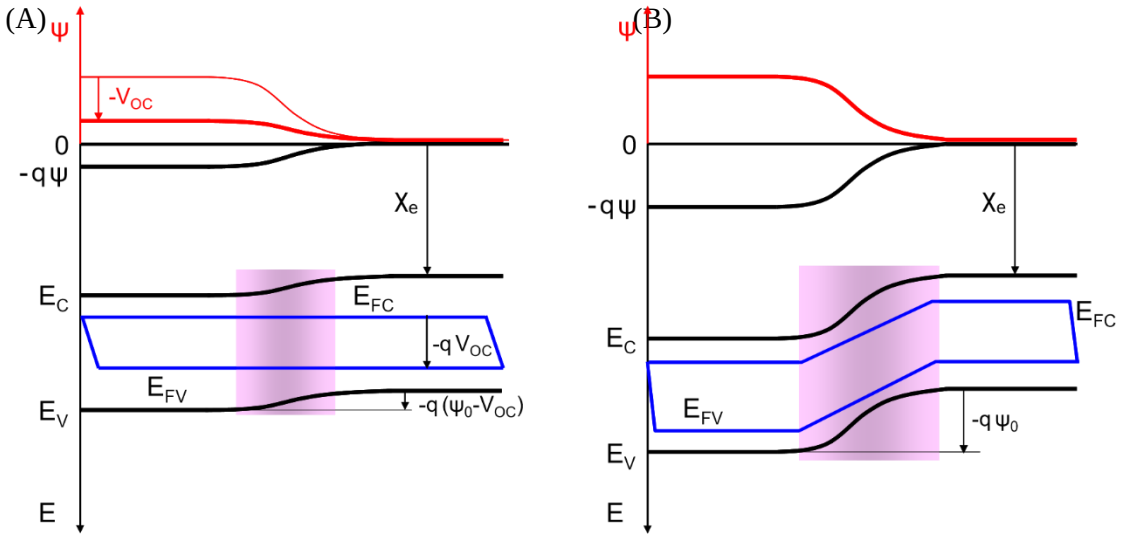

Figure 2.15: Energy band diagram of a p-n junction under illumination for an open-circuit (A) and short-circuit (B) conditions [4].

2.5 GENERATION AND RECOMBINATION

2.5.1 Introduction

Consider a piece of semiconductor material which is in equilibrium. Illuminating the material causes the electrons to be excited from the valence band to the conducting band, resulting in generation of holes in the valance band. The incident light has not disturbed the material from the state of thermal equilibrium, clearly creating a higher concentration of holes in the valance band and a higher concentration of electrons in the conduction band as compared to the equilibrium state. The inequality is then valid,

$$np > n_i^2 \qquad 2.43$$

When incident light is turned off, electrons will recombine with the holes until the equilibrium state is achieved once again. There are different types of recombinations that can take place depending on the material [2]. From the photovoltaic effect it is clear that the rate of recombination strongly determines the performance and efficiency of the photovoltaic cell.

The recombination rate determines the saturation current. Higher recombination rates result in higher saturation current density, which has an effect on the solar cell open circuit voltage (*Voc*) and thus on the energy conversion efficiency.

2.5.2 Generation

The radiative generation of electron-hole pairs occurs when photons are partially absorbed by the semiconductor. If the photon energy is higher than the band gap of the material the bonds holding electrons together can be broken, causing them to be excited to the conduction band, consequently generating a hole in the valance band.

2.5.3 Recombination

When the temperature of the material is above 0 K, it may result in higher vibrational energy, causing the electron bond to be broken. This leads to creation of electron-hole pairs. This situation gives thermal equilibrium thus the following holds,

$$np = n_i^2 \tag{2.44}$$

Illumination of the semiconductor result in the increase of generated electron-hole pairs. Increasing the concentration of electrons and holes increases the recombination rate. When the generation and recombination rates are equal a steady state is achieved, causing band-to-band recombination. This is a radiative process which occurs when the conduction band electron annihilates the valance band hole. The recombination of an electron and a hole causes a photon that carries excess energy to be emitted and energy is released as heat into the lattice.

The Shockley-Read-Hall recombination process occurs when an electron in transition from band gap to band gap acquires a new energy state within the band gap due to the presence of an impurity in the lattice. These impurities are called deep level traps within the semiconductor. These recombination centres generated by the impurities allow trap states or energy states within the forbidden gap. An electron can be trapped at a defect and then recombine with a hole that is attracted by the trapped electron. This process is non-radiative and the excess energy is dissipated as heat within the lattice material. The two types of traps are first the acceptor-type traps that are negative when they contain an electron and neutral when they are empty. The second type of trap are the donor-type traps which are positive when they are empty and neutral when they contain an electron.

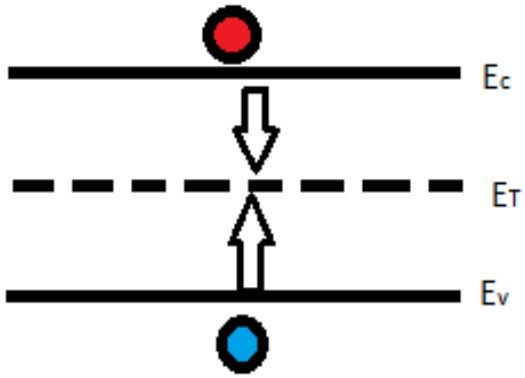

Figure 2.15: Energy band diagram representing the trap level electron-hole recombination process.

In an indirect semiconductor material the Auger recombination process becomes important. The Auger recombination process is a three particle process. In this process the energy and momentum of the recombining electron and hole is conserved by transferring the energy and momentum to another hole or electron. If the third particle involved in this process is an electron then the electron is excited into a higher level in the conduction band. The electron then relaxes again and the energy is transferred vibrational energy of the lattice and dissipated finally as heat. The Auger recombination rate is strongly dependent on the charge carrier densities of the electrons and holes.

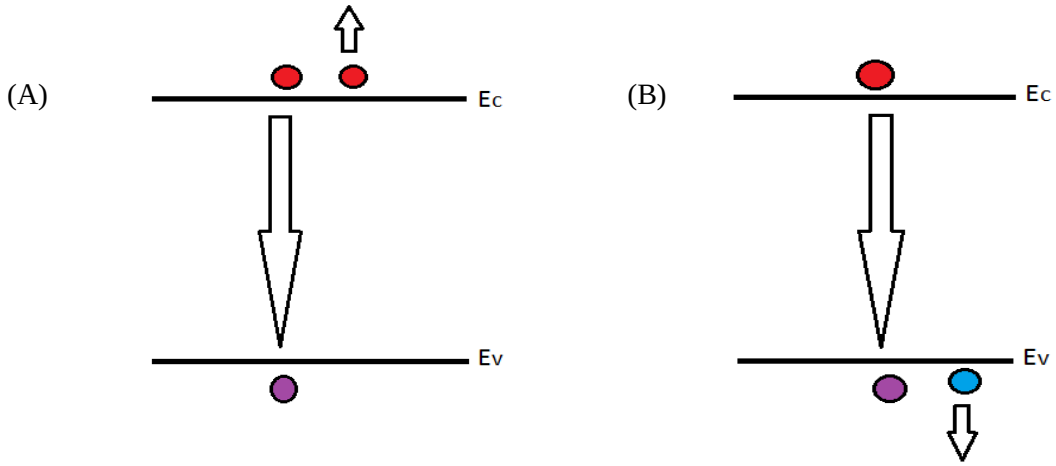

Figure 2.16: Representation of the Auger recombination process with two electrons (red) involved (A), two holes (purple and blue) involved (B).

CHAPTER 3

SOLAR CELLS

3.1 INTRODUCTION

A solar cell is a diode that generates electric current by absorbing solar energy and converting it into electrical energy by a process known as the photovoltaic effect. The operation of the photovoltaic cell requires three basic processes, 1) the absorption of light to generate electron-hole pairs or excitations, 2) the separation of the charge carriers of opposite types, 3) the extraction of those charge carriers to an external circuit resulting in an electrical current being generated. There are varies types of solar cells that have been created and developed in an attempt to obtain higher efficiencies, cheaper cells and wider absorption spectrums. The first practical solar cell was used on the orbiting satellite Vanguard 1 in 1958. The cells were made of single crystal silicon wafers which had an efficiency of 6 % [2].

Solar cells can be classified into the first, second and third generation cells. The first generation cells refer to the wafer-based cells which are mostly made up of crystalline silicon, the predominant photovoltaic technology, that include materials such as poly-silicon and mono-crystalline silicon.

The second generation refers to thin film solar cells. These solar cells are less expensive than the first generation solar cells as they require a decreased amount of material to produce. The cells are a physically thin technology that has been applied to photovoltaic as the name implies. Their efficiency are only slightly less than the other types of cells but require a larger surface area to generate the same power. This second generation, however, are still costly since they require special equipment and energy consuming processes such as vapour deposition for their production. Finally the third generation solar cells include a number of thin-film technologies with most of these solar cells still in the development and research phases. In this third generation cells many new materials have been used such as organic materials, often organometallic compounds as well as inorganic substances. Initially the potential of these cells seemed low as a result of the low efficiency's and the stability of the absorber material being too short for commercial application [15].

There is still, however, great promise for producing low-cost, high efficiency solar cells. The application of solar energy is only constrained by our imagination, a few applications include power plants which in turn can be cost efficient in the long run as well as environment friendly. Another application is the future of transportation such as solar cars. An interesting applications of solar cells is flexible solar cells which can be used on non-rigid surfaces. Transparent solar cells also can be used on windows of building and motor vehicles. Using these transparent solar cells can increases the surface area exposure in urban high population areas without the loss of space [15].

3.2 BASIC CONCEPTS

3.2.1 The photovoltaic effect

When light is incident on the absorber material, the light is absorbed if the photon's energy is larger than the band gap energy. Then electron-hole pairs are formed as these electrons are promoted to the conduction band. In this material the goal is to separate these electrons and holes before they recombine. An important requirement for an efficient cell is that the thickness of the absorber material is not more than the diffusion lengths of the charge carriers. A membrane (semipermeable) that allows electrons to move through and blocks holes is a material which has a large conductivity for electrons and a low conductivity of holes. An example of such a material is an n-type semiconductor material. The opposite is also true, a hole membrane material is a p-type material. An induced electric field helps to separate these electrons and holes and allows them to move to opposite sides in the material and at the n-type membrane the electrons can only flow through and at the hole membrane only holes can flow through. This generates a potential difference and current [3], resulting in an electrical potential. The electrons then flow through an external circuit and subsequently converted to electrical energy. As the electrons re-enter the cell they recombine with holes at the metal-absorber interface. This concept is depicted in figure 3.1 by using a silicon p-n junction solar cell.

The efficiency of electron and hole creation, separation and collection determines the photocurrent. The energy difference between the electrons and holes in the final state before leaving the cell determines the photo-voltage. The product of these two quantities gives the electrical power. The electrical power divided by the solar irradiated power gives the efficiency of converting solar energy into electrical energy in the photovoltaic cell.

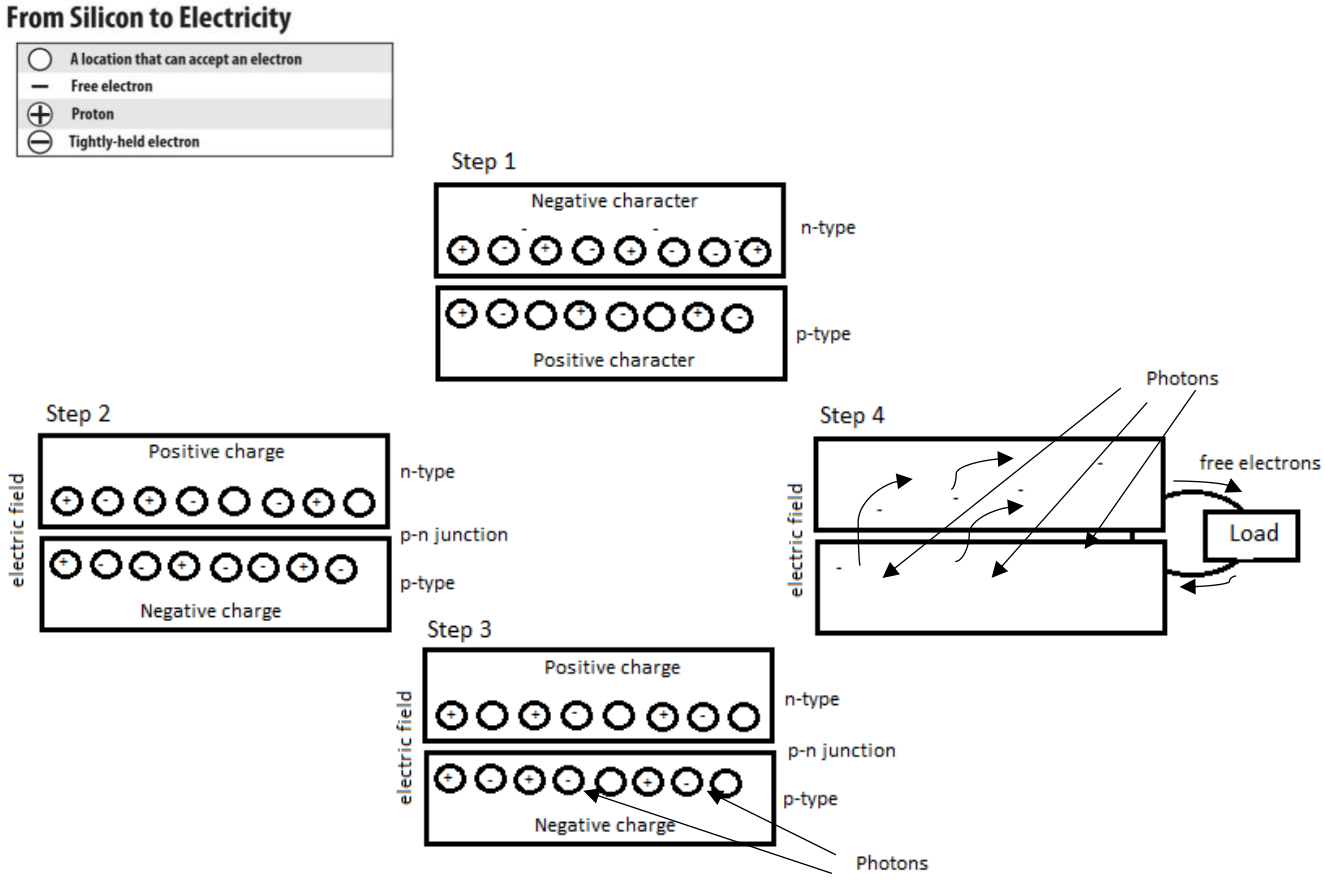

Figure 3.1: Step by step presentation of the photovoltaic effect within a silicon solar cell. **Step1**- Two materials are brought together a p-type and an n-type. **Step 2**-Between these regions a p-n junction is created. **Step 3**-When the material is irradiated with light, photons are incident on the material and are absorbed by the electrons. Electron-hole pairs are formed. **Step 4**- Electrons are promoted to the conduction band. Electrons and holes are collected at opposite ends of the material and then generates a current and voltage which generates electricity. (Adapted from [14])

3.2.2 Type of Solar cells

There are many types of solar cells that are used and developed in today's day and age. The table below represents a few types of solar cells and the average monitored efficiencies of these cells.

Type of Solar cell	Average efficiency (%)
Amorphous Silicon Solar Cell (a-Si)	7
Biohybrid Solar Cell	6.4
Buried Contact Solar Cell	25
Cadmium Telluride Solar Cell (CdTe)	11.1
EFC (Ribbon) Si standard junction	13.4
Organic Polymer	1.7
Copper Indium Gallium Selenide Solar Cells (CI(G)S)	12
Dye-Sensitized Solar Cell (DSSC)	5
Organic Polymer (225)	3.9
Micromorph Cells (Tandem-Cell Using a-Si/µc-Si)	9
Mono-crystalline Solar Cell (Mono-Si)	17.1
Multijunction Solar Cell (MJ)	20-25
Perovskite Solar Cell	20
Photo-electrochemical Cell (PEC)	17
Polymer Solar Cell	10
Polycrystalline Solar Cell (Multi-Si)	14.7
Quantum Dot Solar Cell	7
Thin Film Solar Cell (TFSC)	21
Black Silicon Solar Cell	2.2

Table 3.1: Solar cell type and their average efficiency as tested in Laboratory [23].

3.2.3 Energy source

A solar cell uses energy from the sun to produce electricity. The sun is intensely hot, self-luminous body of gases (mainly hydrogen and helium) at the centre of the solar system and is a medium-size main-sequence star. It is so large that it contributes to 99.68 % of the total mass of the entire solar system [2]. This is the largest natural fusion reactor, where nuclear fusion takes place at the core with temperatures of approximately 15 000 000 K. This is the proton-proton reaction which takes place at the core and one of the product of this reaction is electromagnetic radiation. This electromagnetic waves travel to the surface of the sun called the photosphere and is radiated to the rest of the solar system. The photosphere temperature is approximately 6000 K and it behaves like a blackbody. The total power density of the solar radiation that is incident outside the earth's atmosphere is approximately $1361\,\mathrm{W/m^2}$. The figure below depicts the solar spectrum for the region outside the atmosphere. When the sun is at its zenith the optical air mass (AM) is unity (0), when the distance travelled by the radiation to the surface of the earth is minimal. This spectrum is depicted below as AM 1.5.

The earth's orbit is not circular but slightly elliptical and eccentric, thus the earth-sun distance varies from approximately one astronomical unit ($1.495\text{x}10^{11}$m) to 1.017 astronomical units. The earth is also tilted on its own polar axis at an angle of 23.5 degrees and this results in the seasonal variations. Due to the orbit and angle variation it is clear that the intensity of the sun and angle incident on the earth is not constant.

Another factor that affects the solar radiation that is incident on the surface of the earth is the atmosphere. On a clear day with the sun perfectly overhead, approximately 70 % of the solar radiation through the atmosphere reaches the earth's surface and another 7 % reaches the surface in approximately isotropic manner after scattering from atmospheric particles and molecules. The rest of the radiation is absorbed or scattered back into space. These approximations vary with time and location depending on the water vapor and dust concentrations in the atmosphere. Figure 3.3 depicts the solar radiation on a clear sky day at sea level.

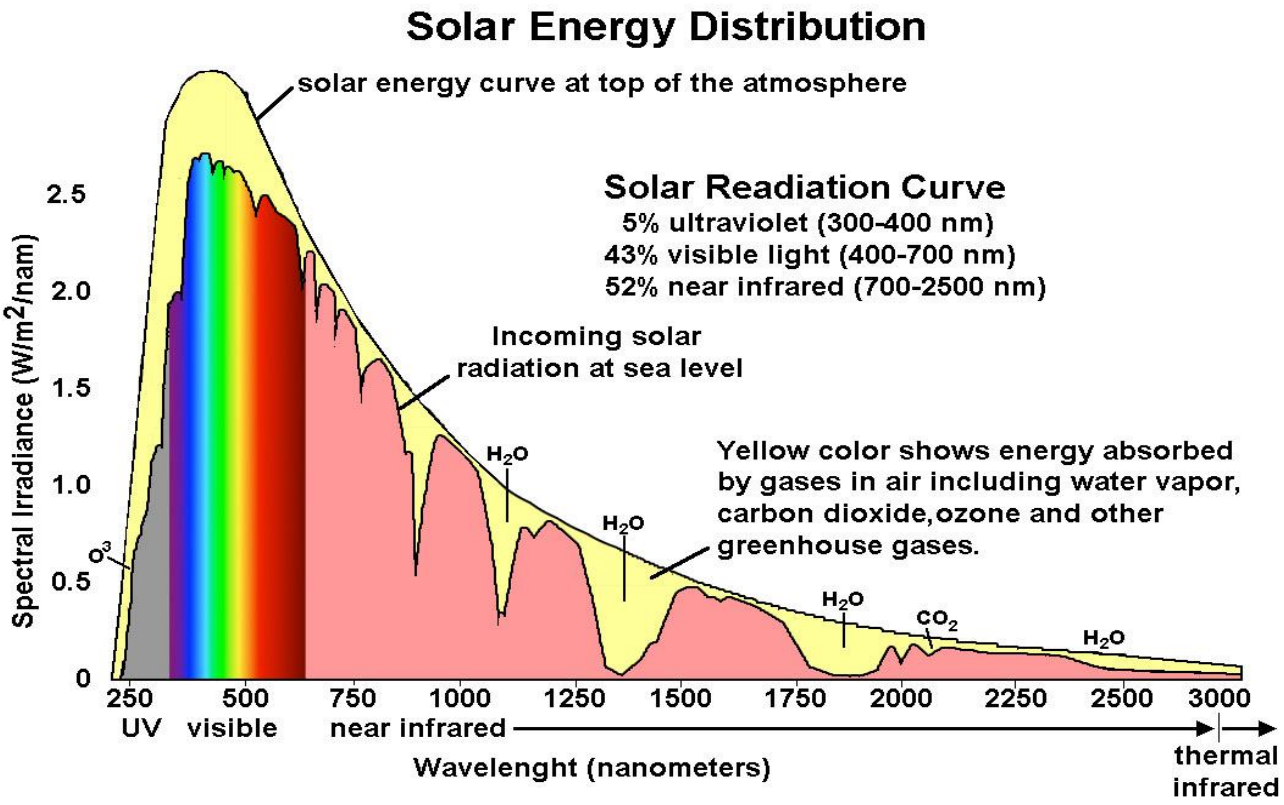

Figure 3.3: Spectral power density of sunlight. The different spectra refer to the black-body radiation at 6000K, the extra-terrestrial AM0 radiation and the AM1.5 radiation [2].

3.2.4 Limitations

There are a number of limitations that restrict the performances of solar cells. For the photon of the incident light wave to be absorbed by the electrons in the semiconductor material the photon must have energy $E > E_g$. Thus all photons with energy lower than the energy gap pass through the material and do not contribute to the conversion of the solar energy to electricity. To overcome this limitation either the material used to fabricate the solar cell should be chosen to reduce the effect of this limitation. Another method of overcoming this limitation is the fabrication of a new type of solar cell - a multifunction solar cell. This type consists of multiple solar cells stacked on top of each other with different absorption spectra resulting in a wide absorption for the entire visible light.

The second limitation to the efficiency of the solar cell is the thermalisation of photon energies exceeding the band gap energy. When the energy of the incident photon is larger than the band gap energy the electron is excited and promoted to the conduction band converting excess energy to heat thus increasing the temperature of the absorber material. This phenomenon can be explained by considering the following example. Consider the illuminated solar cell as a heat engine. The absorber material within the solar cell is the heat reservoir at a temperature T_A and the rest of the cell is a cold reservoir. For simplicity, we assume the temperature of the entire cell as room temperature $T_c = 300\,K$. The incident radiation absorbed by the absorber material is converted to chemical energy and stored in the electron-hole pairs. We also assume that a photon absorbed by the material has an efficiency of 1, thus no energy loss within the process. The efficiency of this thermodynamic heat engine of this solar cell is given by

$$\eta_{TD} = 1 - \frac{T_c}{T_A} \tag{3.1}$$

The process will heat the absorber material while absorbing the solar energy. If we assume that the absorber to be a black body material, all incident radiation will be absorbed and that makes the energy source, the sun, a black body at a temperature of 6000 K. The solar irradiance incident on the solar cell absorber material, where δ_{inc} is the solid angle covered by the incident solar energy is given by the following

$$I_e^S = \sigma T_S^4 \delta_{inc} \tag{3.2}$$

and the emission of the absorber (considered as a black body) is given by

$$E_e^A = \sigma T_A^4 \delta_{emit} \tag{3.3}$$

Using the above equations the efficiency of the absorber is simplified to

$$\eta_A = 1 - \frac{\delta_{emit} T_A^4}{\delta_{inc} T_S^4} \tag{3.4}$$

and for sunlight incident from all possible angles the $\delta_{inc} = 2\pi$ and $\delta_{emit} = 2\pi$ then

$$\eta_A^{\max} = 1 - \frac{T_A^4}{T_S^4} \tag{3.5}$$

is the total efficiency of the solar cell given by

$$\eta_{SC} = (1 - \frac{T_A^4}{T_S^4})(1 - \frac{T_C}{T_A}) \tag{3.6}$$

The ideal solar cell is represented by equation 3.6, indicating that the maximum efficiency cannot exceed 85 %. This is notable limitation to consider when studying photovoltaic technology [21]. There are however more issues related to solar cell limitations and drawbacks that result in the reduction of the efficiency of a solar cell. A complete determination of the efficiency is given below:

$$\eta = \frac{\int_0^{\lambda_g} \frac{hc}{\lambda}\phi_{ph,\lambda}\,d\lambda}{\int_0^{\infty} \frac{hc}{\lambda}\phi_{ph,\lambda}\,d\lambda} \cdot \frac{E_g \int_0^{\lambda_g} \phi_{ph,\lambda}\,d\lambda}{\int_0^{\lambda_g} g\,\frac{hc}{\lambda}\phi_{ph,\lambda}\,d\lambda} .(1 - R^*).IQE_{op}^*\eta_g^*.IQE_{el}^* . \frac{A_f}{A_{out}} . \frac{eV_{oc}}{E_g} .FF \tag{3.7}$$

Each of the eight terms in equation 3.7 are separated by a "." and described as follows:

1) Loss due to non-absorption of long wavelengths.
2) Loss due to thermalisation of the excess energy photons.
3) Loss due to the total reflection of the photon.
4) Loss by incomplete absorption due to the finite thickness.
5) Loss due to recombination of the electron hole pairs.
6) Loss due metal electrode coverage, shading losses.
7) Loss due to voltage factor.
8) Loss due to fill factor.

3.2.5 The advantages and drawbacks of photovoltaic cells

The advantages and drawbacks of photovoltaic cells can be summarized in the following table.

Table 3.2: Summarized pros and cons of photovoltaic cells [4].

Advantages	Drawbacks
No emissions	PV cannot operate without light
Environmentally friendly	Large area required for large application
No noise or moving parts	Initial cost very high
No use of fuels and water	Energy storage devices required
Long lifetime	
PV cells operate even in cloudy weather	
Minimal maintenance required	

3.3 Si/PEDOT:PSS INVERSION LAYER SOLAR CELL

3.3.1 Introduction

Poly (3,4-ethylenedioxythiophene) poly (styrenesulfonate) known as PEDOT:PSS has been shown to be a very cheap and effective metallic top contact for Schottky type hybrid solar cells. This is an organic material and polymer, which acts as a transparent p-type material or hole conductor with a band gap of 1.6 eV and a work function φ_m= 5.0 [31]. The acidic nature of this material is important to the function and performance of the solar cell device since it affects the conductivity of the device. When PEDOT:PSS is deposited onto n-type Si, a p-n junction is formed.

An inversion layer can be formed by using a n-or p-type semiconductor with a high (low for p-type) for n-type work function metal resulting in the formation of a Schottky barrier so high that the minority charge carrier become dominant in a narrow layer at the two materials interface. If we consider Schottky barriers as discussed in section 2.3, the PEDOT:PSS acts as a metallic-like contact due to its high work function. The charge transfer between the two

materials one semiconductor and the other a metal-like form a voltage across the barrier, consisting of a built-in voltage is defined as follows

$$V_{bi} = \varphi_m - E_F \tag{3.8}$$

where φ_m is the work function of the PEDOT:PSS and E_F is the Fermi energy of the n-Si. The Schottky barrier height is defined by the equation

$$\varphi_b = V_{bi} + \left|E_i - E_F\right| \tag{3.9}$$

and the built in voltage exceeds the critical value

$$V_{bi} > \left|E_F - E_i\right| \tag{3.10}$$

where E_i is the intrinsic Fermi level, the majority carriers at the semiconductor surface and of the bulk are of opposite type resulting in the generation of a p-n junction without dopant diffusion. This region is known as the inversion layer.

3.3.2 Inversion layer solar cell structure

The first type of solar cell studied in this project is the n-type Si/PEDOT:PSS inversion layer solar cell which was created by using n-Si and PEDOT:PSS as the p-type contact, figure 3.4 (A).

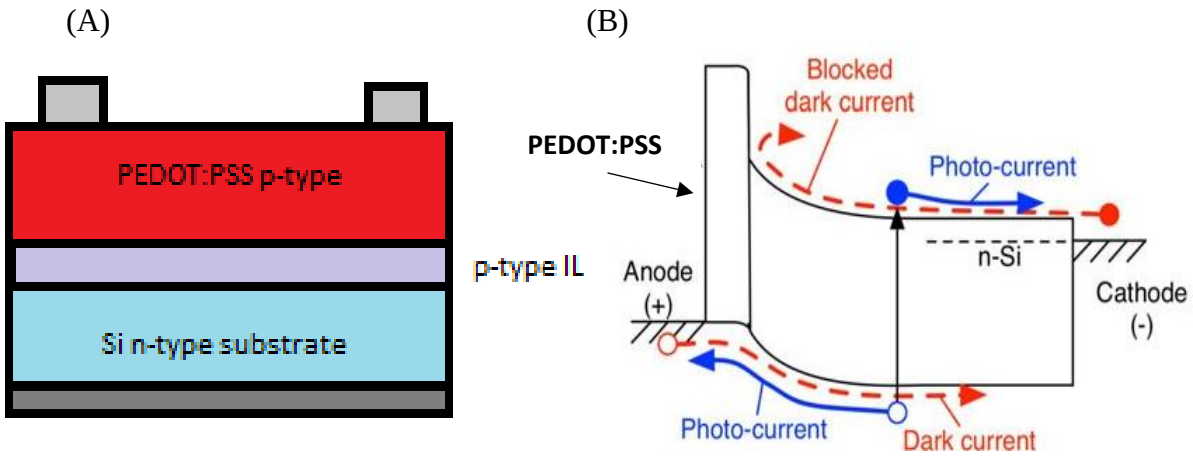

Figure 3.4: The basic presentation of the Si/PEDOT:PSS inversion layer solar cell (A) and band diagram of device under illumination and a forward bias (B) [31].

Figure 3.4 (B) shows the band diagram of the inversion layer solar device. Light enters from the top of the cell and due to the transparency of the PEDOT:PSS layer most of the light is absorbed by the silicon layer. The LUMO (lowest unoccupied molecular orbit) level of the PEDOT:PSS is much higher than the conduction band energy of the n-Si therefore the electrons within n-Si will be blocked from travelling into the PEDOT:PSS. Where the HOMO (highest occupied molecular orbit) level of the PEDOT:PSS and the valance band of the n-Si are nearly aligned and this allows holes within the silicon to travel into the PEDOT unimpeded. The work function of the PEDOT:PSS material is fairly high at approximately 4.9 eV. Due to this high work function a depletion region exists in the n-type silicon at the Si/PEDOT interface. Within this depletion region the separation of the photo-generated carriers in the silicon occurs causing a photocurrent. The negligible hole barrier at the interface allows the collection of holes at the anode and the large barrier at the interface reduces the electron dark current to the anode. This results in a low saturation current and a high open circuit voltage. This is shown in figure 3.4 (B) where the red line shows the electron flow and blue the photocurrent.

3.4 POLYMER SOLAR CELL

3.4.1 Introduction

Polymer solar cells are a type of flexible solar cell which are made by using large polymers molecules. This has the advantage that they can be coated or sprayed on in the production of these cells, thus the production cost is much lower than the standard expensive vacuum deposition as for the silicon first generation solar cells. Another advantage of these cells is that they are created by using polymers with optical tuning capabilities. The resulting solar cells are then lightweight, flexible with the potential to be transparent which can lead to applications in windows, walls and electronics. The two major drawbacks of polymer solar cells are the short lifetime and low efficiency.

Traditional lifetime of silicon solar cells can extend to 25 years were polymer solar cells so far might at best reach a year. The efficiency of polymer solar cells are also lower than traditional cells with average between 3-6 %, however, polymer solar cells that have higher than 10 % efficiency has been reported [16].

Organic polymers such as P3HT:PCBM (poly(3-hexylthiophene) : phenyl-C61-butyric acid methyl ester) blends have wider band gaps than natural semiconductors. Understanding the photo-conversion mechanism in the solar cell is the key to the design and production of more efficient organic solar cells [17].

3.4.2 Photo-conversion mechanism in polymer solar cells

The photo-conversion process can be divided into five main groups. The first is light absorption followed by exciton transport, exciton dissociation, charge transport and finally charge extraction.

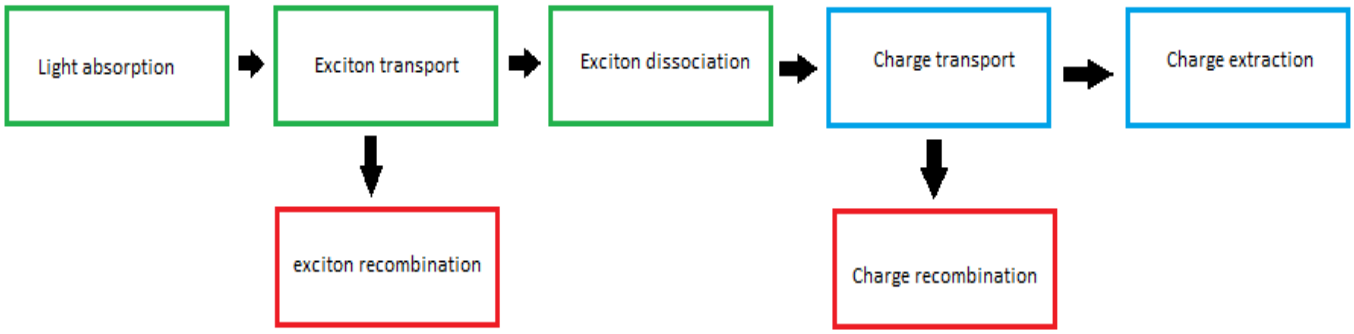

Figure 3.5: Outline of photo-conversion mechanism.

In organic solar cells a few new terms are used. Consider an organic semiconductor material at room temperature. Most of the bonding electrons in this material are in the highest occupied molecular orbital (HOMO) or valance band. The anti-bonding state of the material can be considered as the lowest unoccupied molecular orbital (LUMO) or the conduction band of the material. It is obvious that the difference between the LUMO and HOMO levels is the band gap energy of the material. The vacuum level is defined as the energy of a free stationary electron which is not bound to any of the levels. This is the alignment level of two different materials. The ionisation energy is the energy required to excite an electron from the HOMO or valance band to the vacuum level and the electron affinity is the energy obtained by moving an electron from the just outside the vacuum level to the bottom of the LUMO or conduction band. When a material has a high electron affinity it can easily accept an extra electron in the

LUMO or conduction band and thus acts as an electron acceptor. However a material with a low ionisation potential can release an additional electron and thus acts as an electron donor.

The photoactive layer in an organic photovoltaic cell consists of a conjugated carbon based material, which means that the carbon atoms within the chain have alternating single and double bond and every atom in the chain as a p-orbital available. The conjugated aspect as well as the low dielectric constant of the material gives rise to a different photo-conversion mechanism compared to inorganic photovoltaic cell which uses the photovoltaic effect. The difference occurs in the creation of excitons in the organic solar cells upon light absorption compared to the electron-hole pairs that are directly generated in the traditional inorganic solar cells. The exciton population in the cell is directly related to the amount photons absorbed. Due to the Coulomb attraction and the localised energy nature of the organic semiconductor material the excitons remain bound in the organic electronic material. As expected, photons which have energy higher than that of the band gap energy will result in excitons being created with the same energy and since excited electrons rapidly relax to the LUMO. An exciton is an excited electron-hole pair that are still bound by the Coulomb forces between the electron and hole. This process is very fast and happens in a time scale of a few femtoseconds which is faster than exciton recombination and hopping. Organic semiconductors generally have high absorption coefficients at the peaks of their absorption spectrum, thus by increasing the overlap of the absorption profile can result in the exciton generation being maximised [16]. These excitons can diffuse through the material. The life time of excitons is in the nanosecond scale and thus the diffusion length is only in the order of 10nm.

When the electron donor and electron acceptor materials are brought together an interface can be formed between the two materials. The vacuum level will align for both materials and if the materials can be chosen such that there is a large difference in the materials LUMO and HOMO levels these local electric fields can break the excitons. The electrons can now be injected into the electron acceptor material and the hole will remain in the electron donor material. This process is depicted in figure 3.6.

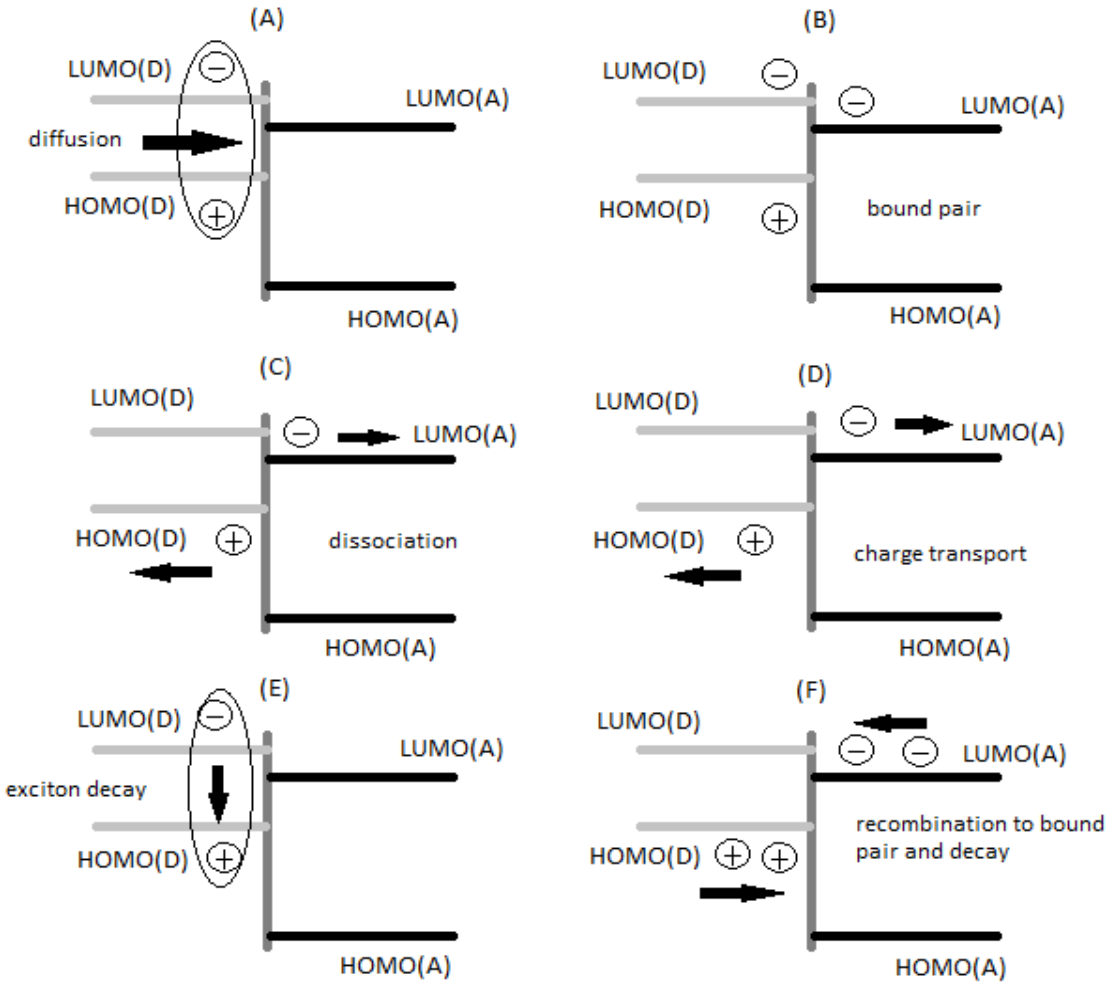

Figure 3.6: Part **(A)** shows the light absorption by the polymer active layer thus resulting in the generation of an exciton. If the exciton reaches the interface, electron transfer to the acceptor material is energetically favoured is shown in part **(B)**. In part **(B)** a Coulombically bound electron-hole pair. The dissociation of the electron-hole pair and the creation of free charge carriers are shown in part **(C)**. The charge carriers now need to be transported to the electrodes in order to be extracted as shown in part **(D)**. Part **(E)** depicts the exciton decay is one possible loss mechanism and other loss mechanism are shown in part **(F)** known as the geminate recombination of the bound electron-hole pair and the bimolecular recombination of the free charge carriers.

Due to the very short diffusion length of these cells, a bulk heterojunction is used whereas the electron acceptor and donor materials are mixed tighter to form a blend thus eliminating the diffusion length restriction of only 10 nm [17,18]. Thus the electrons can travel through the electron acceptor material to the metal back contact and the holes can travel through the electron donor material and be collected at the TCO electrode.

3.4.3 Polymer solar cell structure

In a polymer solar cell, the active layer of the cell is sandwiched between two collecting electrodes. These two layers are the cathode and anode part where the electron and holes are collected after electron-hole pairs are formed. One of these collective layers should be transparent to allow the incident light to travel through to the active layer. Currently ITO is used as the transparent layer. The other collective layer requires the correct work function and in this project aluminium (Al) was used. The active layer consists of an electron acceptor and donor material. The common approach to produce this active layer is to form a heterojunction and thus form a blend of the two materials and transfer the solution to the substrate and then evaporate to form a thin film active layer on the substrate.

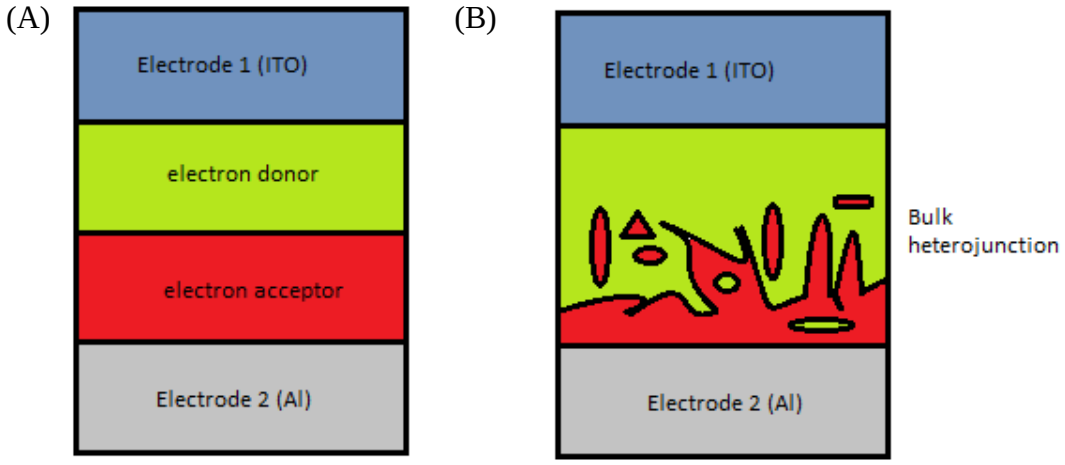

Figure 3.7: The layer structure of an organic solar cell (A) and an organic solar cell with a bulk heterojunction (B).

Once photons are incident on the solar cell surface and reach the active layer an exciton is formed (which is similar to an electron-hole pair). These excitons then diffuse to the boundaries of the donor-acceptor blend where it dissociates into an electron and hole pair. The electron and hole then travel to opposite electrodes (opposite collective layers). In this project, we have used one of most commonly used active layer materials, the donor-acceptor copolymer P3HT:PCBM material for photon-electron conversion. The P3HT:PCBM blend has a wider band gap than natural semiconductor materials like silicon. As the electron and hole pairs are created the holes are usually collected at the TCO electrode. In this study ITO was used and

the electrons are collected at the metal contact. Al was used as the metal contact in this study. For the ZnO nano rods a seed layer was required for the growth of these nano rods.

The structures of the studied organic solar cells is given in figure 3.8.

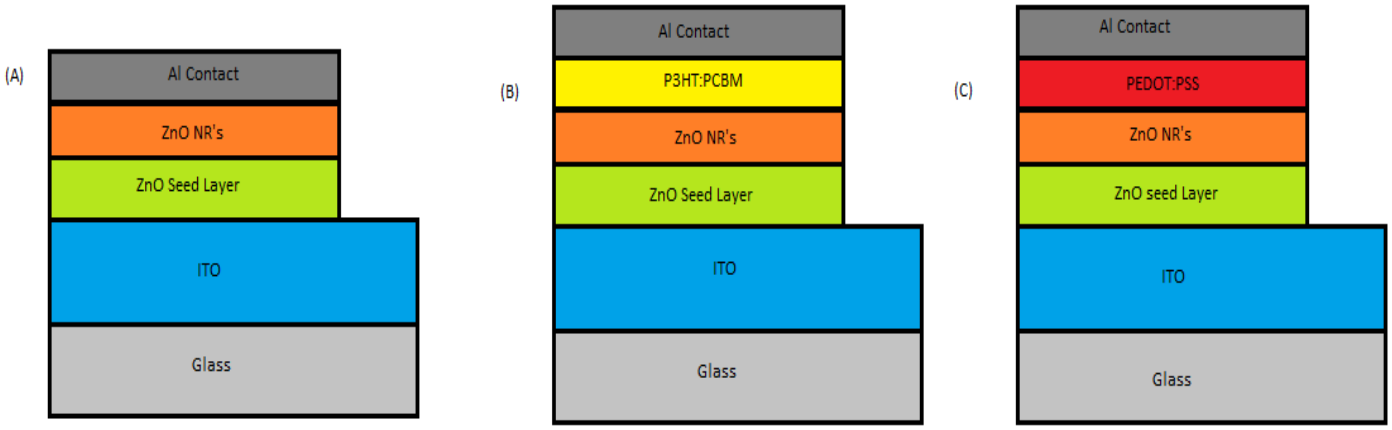

Figure 3.8: Illustration of the structure of an organic solar cell using (A) ZnO Nano rods as a control (B) P3HT:PCBM and (C) PEDOT:PSS.

The results of these polymer solar cells are given in chapter 7.

CHAPTER 4

THE HALL EFFECT

4.1 INTRODUCTION

The Hall Effect was discovered by E.T. Hall in 1879 and is described as one of the richest sources of conduction properties of semiconductor materials [8]. When a conducting material with current passing through is placed in a magnetic field an electric field will be induced. The direction of this electric field is normal to both the magnetic field and current directions. The Hall measurement is important since it gives the resistivity, mobility and the carrier density of the measured semiconductor. The mobility is a measure of the impurity content, quality and homogeneity of epitaxial layer. Resistivity is the proportional relation between the electric field and the current density. In this chapter we will discuss the basic principles and concepts of the Hall Effect.

4.2 THEORY OF HALL EFFECT

4.2.1 Hall Effect derivation

The basic theory of the Hall Effect arises from the basic nature of conduction where current consists of the flow of charged particles (electrons) drifting under the influence of an applied electric field. The velocity at which these carriers will flow is called the drift velocity v and will flow in the direction of the applied electric field (holes) or in the opposite direction of the applied electric field (electrons). The magnitude of the drift velocity of the carriers is proportional to the applied electric field strength E.

The Hall Effect is the production of a transverse potential (voltage charge along the y-direction) and this is due to an applied magnetic field on the material (along the z-direction) with current flowing in the x-direction as shown in figure 4.1. Consider a slice of n-type material where the electrons are the dominant charge carriers. Due to the magnetic field B which is perpendicular to the current flow, the charge carriers will experience a force known as the Lorentz force given by

$$F = e(v \times B) \tag{4.1}$$

where v the drift velocity of the electrons and B is the applied magnetic field [7,19].

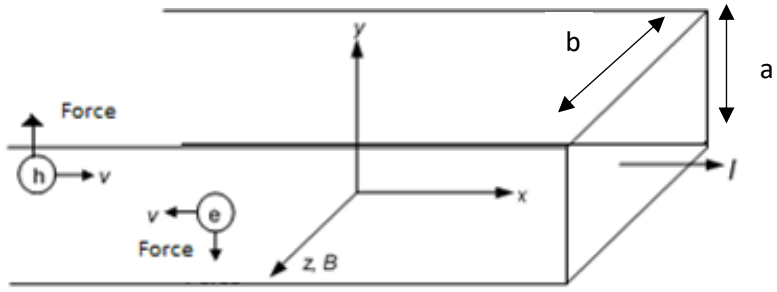

Figure 4.1: The vector diagram that illustrates the Hall Effect [7].

The electrons within the semiconductor will be deflected in the direction perpendicular to the plane of the magnetic field B and drift velocity v. The current within the semiconductor will be contained within the boundaries of the semiconductor solid. This will result in electrons being deflected to one side of the semiconductor by the applied magnetic field. As the electron concentration is increased on one side of the solid, it will produce an electric field along the *y*-direction, E_y and then further repel carriers from that side of the solid. A steady state is eventually established when the effects of this electric field is equal to the magnetic force. Thus equation 4.1 becomes [7]:

$$eE_y = e(v \times B_z) \tag{4.2}$$

where this transverse electric field E_y is proportional to the product of the applied magnetic field B_z and the current density J_x of the solid [9]. The proportionality constant is denoted the Hall coefficient R_H[7].

$$E_y = R_H J_x B_z \tag{4.3}$$

using the relation between the current density and velocity of the electrons in the solid

$$J = nev \tag{4.4}$$

and equation 4.3 we obtain the following [8]:

$$E_y = (\frac{1}{ne}) J_x B_z \quad 4.5$$

thus the Hall coefficient is equal to

$$R_H = -\frac{1}{ne} \quad 4.6$$

where *n* is the carrier concentration of electrons denoted by the negative sign. For holes the hall coefficient is given below, where *p* is the concentration of holes [7].

$$R_H = \frac{1}{pe} \quad 4.7$$

these relations are very useful since the Hall coefficient is related to the carrier concentration. Which is an important parameter in the study of conduction in semiconductors.

4.2.2 Hall coefficient

The Hall coefficient can be expressed with more accurately by using the Hall scattering factor r_H described below for an n-type material [7]:

$$R_H = \frac{r_H}{ne} \quad 4.8$$

the relation between the drift mobility μ and the Hall mobility μ_H can be expressed as the following [9]:

$$\mu_H = r_H \mu \quad 4.9$$

4.2.3 Measurement of the Hall coefficient

According to figure 4.1 the cross-section area of the sample is *a*x*b* with current I_x passing through the sample we define the current density ***J***

$$J = \frac{I_x}{ab} \tag{4.10}$$

a transverse electric field is observed in the *y*-direction E_y due to the magnetic flux density B_z. This transverse potential is known as the Hall voltage and is given by the following [7]:

$$V_H = aE_y \tag{4.11}$$

substituting equation 4.10 and 4.11 into equation 4.3 we can express the Hall coefficient as [7]:

$$R_H = \frac{V_H b}{B_z I_x} \tag{4.12}$$

the Hall voltage measurements gives a value for the Hall coefficient and then using this Hall coefficient we can determine the density of charge carriers and their mobility. Consider a semiconductor where there is no dominant charge carrier in the conduction process. Thus there are hole and electron charge carriers that contribute to the conduction process. This results in mixed conduction and the Hall coefficient is given by [8]:

$$R_H = \frac{(p - nb^2) + (\mu_n B)^2 (p - n)}{e[(p + nb)^2 + (\mu_n B)^2 (p - n)^2]} \tag{4.13}$$

in the low magnetic field limit we get

$$R_H = \frac{(p - nb^2)}{e(p + nb)^2} \tag{4.14}$$

where *b* is the electron to hole ratio. If the electron to hole ration (*b*) is larger than unity then the Hall coefficient reduces to the Hall coefficient of a n-type semiconductor (equation 4.6). If the electron to hole ratio is less than unity then the Hall coefficient reduces to the Hall coefficient of a p-type semiconductor indicated by equation 4.7 [8].

4.2.4 Hall scattering factor

The Hall scattering factor is dependent on the scattering mechanism in the semiconductor material, the band structure of the material, the magnetic field strength *B* and the degeneracy of the carriers [7]. Using the following relation

$$r_H = \frac{R_H(0)}{R_H(\infty)} \tag{4.15}$$

the Hall scattering factor can be determined experimentally. Where $R_H(0)$ the Hall coefficient is in the low magnetic field limit and $R_H(\infty)$ is the Hall coefficient in the high magnetic field limit. As the magnetic field approaches infinity the r_H reaches unity thus it is a fairly good approximation to take the scattering factor as unity at the extreme limit. Equation 4.7 shows that the Hall coefficient is dependent of the Hall scattering factor thus to obtain an accurate Hall coefficient it is necessary to obtain an accurate Hall scattering factor. To do this the electron momentum distribution must be considered. Many of the properties of semiconductor were discussed in chapter 2. Assume that to some degree that there exists a relaxation time τ, then the motion of a charge carrier with charge *q* is given by the following

$$m^* \frac{dv}{dt} = -q(E + v \times B) - m^* \frac{(v - v_{eq})}{\tau} \tag{4.16}$$

where *v* is the velocity, v_{eq} is the equilibrium velocity and m^* the effective mass of the charge carrier. The above equation reduces to Newton's second law which is given by equation 4.2 in the steady state ($^{dv}/_{dt} = 0$) if the velocity is equal to the equilibrium velocity. By solving equation 4.16 the system of coupled differential equations and averaging over the energy distribution of the carriers in a semiconductor material using the Fermi-Dirac function the following current densities are obtained.

$$J_x = \left\langle \frac{\tau}{1+\omega_c^2\tau^2} \right\rangle E_x - \left\langle \frac{\omega_c\tau^2}{1+\omega_c^2\tau^2} \right\rangle E_y \tag{4.17}$$

$$J_y = -\left\langle \frac{\omega_c\tau^2}{1+\omega_c^2} \right\rangle E_x + \left\langle \frac{\tau}{1+\omega_c^2\tau^2} \right\rangle E_y \tag{4.18}$$

the direction of these quantities refer to figure 4.1 and ω is the cyclotronic frequency and is equal to $\omega_c = \frac{eB}{m^*}$ and the brackets denote the averaging over the energy as shown below [19]:

$$\langle F(E) \rangle = \frac{\int_0^\infty F(E) E^{\frac{3}{2}} (\frac{\partial f}{\partial E}) dE}{\int_0^\infty E^{\frac{3}{2}} (\frac{\partial f}{\partial E}) dE} \tag{4.19}$$

the function f denotes the Fermi-Dirac function. If we consider the low magnetic field limit (i.e. $\omega_c \tau \ll 1$) then the expressions of equation 4.17 and 4.18 can be simplified. If we consider figure 4.2 and note that $j_y = 0$ we obtain

$$j_x = \frac{nq^2 \langle \tau \rangle}{m^*} E_x \tag{4.20}$$

if we now simplify equation 4.3. Using equation 4.17, 4.18 and 4.19 we solve for the Hall coefficient as follows[19],[2]:

$$R_H = \frac{1}{q|n|} \frac{\langle \tau^2 \rangle}{\langle \tau \rangle^2} = \frac{r_H}{q|n|} \tag{4.21}$$

and the Hall scattering factor is given by

$$r_H = \frac{\langle \tau^2 \rangle}{\langle \tau \rangle^2} = -3 \frac{m}{m^*} \frac{\int_0^\infty \frac{k^3 \partial f}{d \partial k} [\frac{1}{(S_0 + v_{el})}]^2 dk}{[\int_0^\infty \frac{k^3 \partial f}{d \partial k} [\frac{1}{(S_0 + v_{el})}] dk]^2} \int_0^\infty k^2 f dk \tag{4.22}$$

where the quantity *d* refers the relative mass enhancement in the nonparabolic band and is equal to

$$d = \frac{1}{[1 + \frac{(\frac{m}{m^*} - 1)}{\alpha}]} \tag{4.23}$$

d approaches the value $\frac{m^*}{m}$ if k approaches zero or if the band gap energy (E_g) becomes large. More accurate calculations of the scattering factor are possible but for practical purposes equation 4.22 is sufficiently accurate [19].

4.2.5 Van Der Pauw Measurements

The Van Der Pauw measurements were used to determine the carrier concentration and resistivity of the studied sample. Now that the Hall coefficient is defined by equation 4.12 it is possible to establish parameters of the Hall coefficient such as the Hall coefficient is independent of the length and width of the sample. As long as the sample is flat, homogeneous, connected, isotropic and of uniform thickness then the sample can be of any shape. For the measurements of the carrier concentration and resistivity point-like (small contact area as compared to the rest of the sample) contacts are required. A good strategy is not to let the size of the contact exceed 10 % of the size of the smallest sample dimension [19]. To understand how the Hall coefficient is measured consider the following figure below.

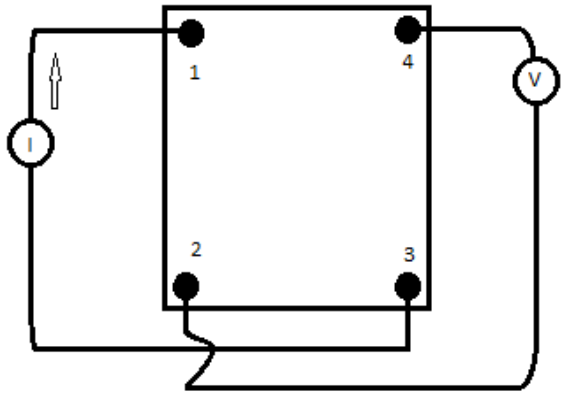

Figure 4.2: Contact configuration for Hall measurements using a square sample.

From equation 4.12 we can observe that the Hall coefficient R_H is proportional to the quantity V_H / I_x were this quantity has dimensions of resistance (Ohm's law). If we define the resistances as follows

$$R_{ij,kl} = \frac{V_{kl}}{I_{ij}} \qquad 4.24$$

where

$$V_{kl} = V_k - V_l \tag{4.25}$$

is the potential between the two contact point's *l* and *k* and I_{ij} is the current flowing between contacts *i* to contact *j*. By averaging over the two configurations of the Hall measurements, errors caused by the misalignment of the contacts are eliminated. The Hall coefficient is thus given by

$$R_H = \frac{d}{B}\left(\frac{R_{31,42} + R_{42,13}}{2}\right) \tag{4.26}$$

there are more thermomagnetic effects that may lead to inaccurate measurements. The thickness of the sample represented by d in equation 4.26. These effects include Righi-Leduc effect, the Nernst Effect and the Ettingshausen effect and are discussed in more detail in section 4.3. Consider $R_{ij,kl}{}^{+}$ as the Hall resistance measured in a magnetic field pointing in the positive z direction (+*z*) and $R_{ij,kl}{}^{-}$ and the Hall resistance measured in the negative z direction (-*z*). All these effects can be eliminated excluding the Ettingshausen effect by averaging over the current and magnetic field directions and thus given us a Hall coefficient as follows

$$R_H = \left(\frac{d}{8B}\right)\left(R^{+}_{31,42} - R^{+}_{13,42} + R^{+}_{42,13} - R^{+}_{24,13} + R^{-}_{13,42} - R^{-}_{31,42} + R^{-}_{24,13} - R^{-}_{42,13}\right) \tag{4.27}$$

using equation 4.8 and the Hall coefficient the carrier concentration can now be calculated, where the Hall scattering factor r_H is usually set to unity. This assumption is true for metals or degenerate semiconductor materials.

The resistivity, ρ of a sample is the proportionality constant between the electric field and the current density of a conducting material and is discussed in section 2.2.5. The reciprocal of the resistivity is the conductivity σ. The resistivity can be given by the following

$$\rho = \frac{\pi d}{\ln(2)}\left(\frac{R_{21,34} + R_{32,41}}{2}\right) f \tag{4.28}$$

where *f* is a correction factor which is dependent on the ratio $Q = \frac{R_{21,34}}{R_{32,41}}$ [19]. The correction factor *f* can be determined by the transcendental equation which is defined by the following

$$\frac{Q-1}{Q+1} = \frac{f}{\ln(2)} \arccos h(\frac{1}{2} e^{(\frac{\ln(2)}{f})}) \qquad 4.29$$

and must be solve numerically. Note that *f* is only a geometric correction factor. The resistivity can also be accurately measured as the Hall coefficient by averaging over all the different contact permutations and current directions [19]. The resistivity is then given by

$$\rho = \frac{\pi d}{\ln(2)} [\frac{(R_{21,34} - R_{12,34} + R_{32,41} - R_{23,41}) f_A}{8} + \frac{(R_{43,12} - R_{34,12} + R_{14,23} - R_{41,23}) f_B}{8}] \qquad 4.30$$

the correction factors f_A and f_B are determined from Q_A and Q_B respectively. These quantities are in turn determined by the following

$$Q_A = \frac{R_{21,34} - R_{12,34}}{R_{32,41} - R_{23,41}} \qquad 4.31$$

$$Q_B = \frac{R_{43,12} - R_{34,12}}{R_{14,23} - R_{41,23}} \qquad 4.32$$

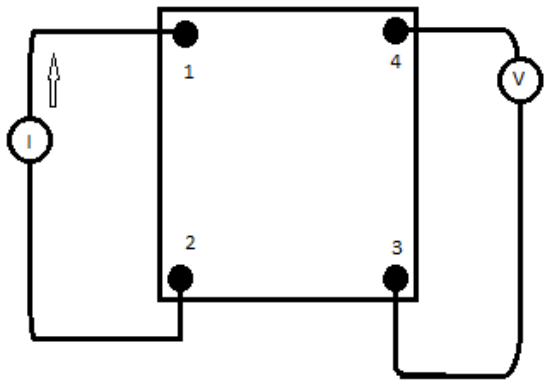

Figure 4.3: Contact configuration for Hall measurements using a square sample.

4.2.6 Mobility

The mobility has been discussed in section 2.2.6. The Hall mobility in terms of the conductivity and Hall coefficient of the sample is given by [19]

$$\mu_H = R_H \sigma \qquad 4.33$$

if the Hall scattering factor is close to unity then the Hall mobility will approximately be equal to the drift mobility.

4.3 FACTORS THAT INFLUENCE MEASUREMENT

When the Hall voltage (V_H) is measured there are associated effects that give rise to potentials that effect the measurements. These associated effects must be accounted for and must be corrected to obtain the correct Hall voltage (V_H). In this section the effects and their corrections will be discussed.

4.3.1 IR Effect

This effect is the potential which arises from the experimental difficulty in aligning the measuring probes on the same equipotential plane [7]. This effect is illustrated in the figure 4.3 where the two probes are not on the same equipotential plane, thus a potential will be measured between them. This potential can be of the same order of magnitude as the Hall voltage.

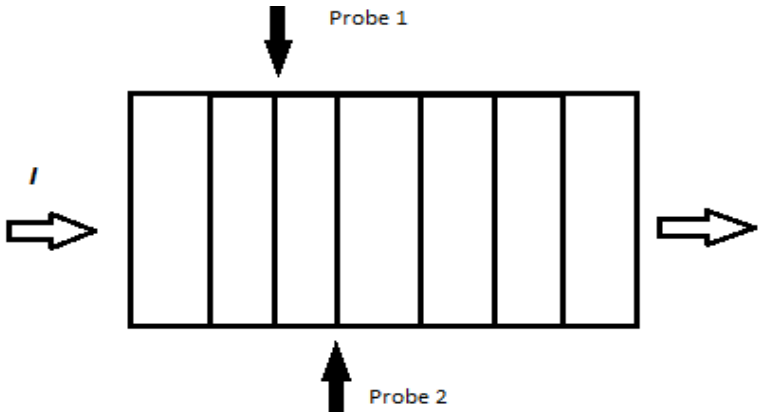

Figure 4.4 The IR drop error, which arises from probe 1 and 2 on the studied sample.

4.3.2 Galvanomagnetic Effects

There are three galvanomagnetic and thermomagnetic effects which can influence the Hall voltage measurements. These effects are called the Righi-Leduceffect, Nernst effect and the Ettingshausen effect [9]. Using the electrons as the dominant charge carriers these effects will

be discussed and illustrated. The red line will indicate how the electrons direction in which they are deflected.

First let's discuss the Righi-Leduc effect. This effect depends on the different velocities of the electrons in the material. When a magnetic field is applied in the *z*-direction and a thermal current flows in the *x*-direction, a transverse temperature gradient is formed in the *y*-direction as depicted in the figure 4.5 below [7].

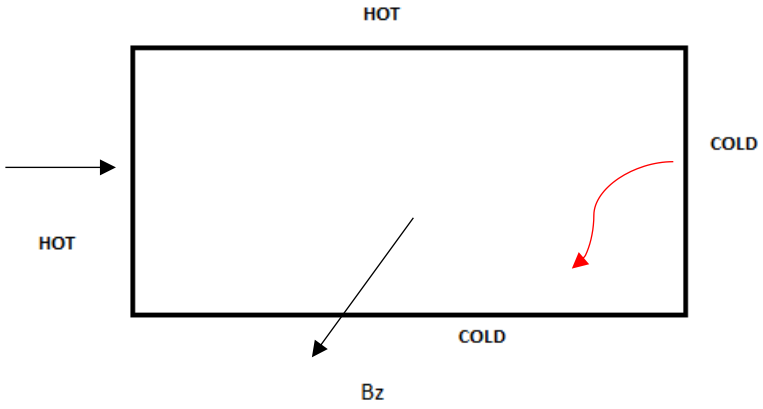

Figure 4.5 Illustration of the Righi-Leduc effect.

Next is the Nernst effect. When there is a current flow in the *x*-direction which arises from a temperature gradient and there is an applied magnetic field in the *z*-direction, a potential gradient appears in the *y*-direction. This potential gradient arises from the electrons trying to diffuse down the temperature gradient and the electrons being deflected by the magnetic field. This is illustrated in the figure 4.6 [7].

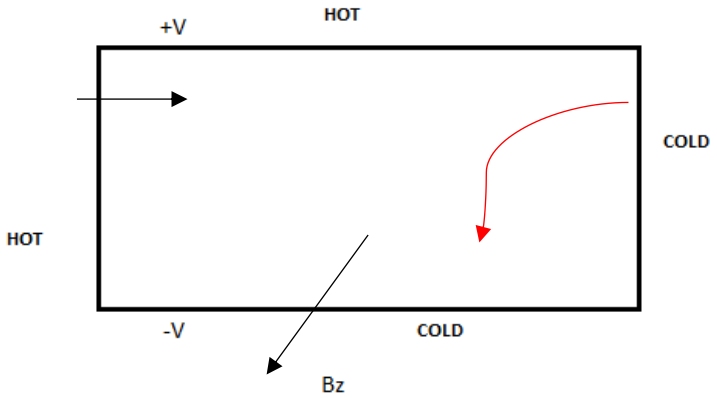

Figure 4.6 Illustration of the Nernst effect.

Finally the Ettingshausen effect. The velocities of the electrons within the material varies. Some electrons have high velocities and others low velocities. When a magnetic field is applied the electrons with higher velocities will follow a different trajectory in the solid compared to the slower electrons. The electrons with lower velocities suffer a greater deflection than the electrons with a higher velocity, thus they have less energy compared the electrons with high velocities [8]. This results in more energy being deflected to the one side of the solid and thus creating a transverse temperature difference. This temperature gradient effects the Hall coefficient, however, this effect is normally less than the experimental error in the Hall coefficient. This is illustrated in figure 4.7 below [7].

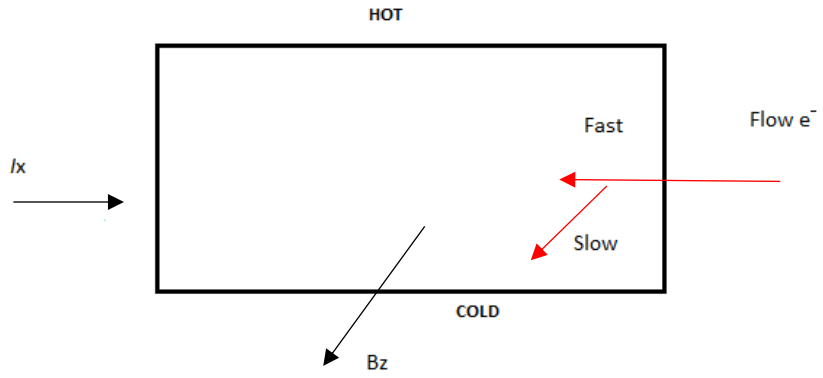

Figure 4.7 Illustration of the Ettingshausen effect.

CHAPTER 5

CURRENT VOLTAGE CHARACTERIZATION IN SOLAR CELLS

The *I-V* measurements (Current-Voltage) is the most important measurement in the characterization of solar cells. From the *I-V* measurements many important properties of the solar cell can be determined such as the efficiency, short circuit current, open circuit voltage and fill factor. These parameters are to classify the quality and performance of solar cells. In this project the *I-V* measurements were done by applying a voltage over the cell and measuring the current over various ranges. The measurements are done under dark and illuminated conditions using a solar simulator. The experimental procedure is discussed in chapter 6 and the results in chapter 7. Within this chapter we will look at the theory of the *I-V* measurements.

5.1 Circuit model of single pn junction Solar Cell

A simple single diode photovoltaic cell can be presented as following circuit shown in figure 5.1 (A). We model photovoltaic cell as a current source in parallel with a diode. When there is no light incident on the cell there is no current (a very small current due to external environment), this results in the cell behaving like a diode. When there is light incident on the cell then current is generated and it flows through the cell. The magnitude of the current is given by equation B. The first term in equation B is the current generated by the solar cell. The second term is the diode current. Where I_0 is the saturation current of the diode. Equation B can be expanded into equation C. Theoretically the effects of the shunt and series resistance effects can be deduced. For a good photovoltaic cell the shunt resistance should be as high as possible and the series resistance should be as low as possible

(A)

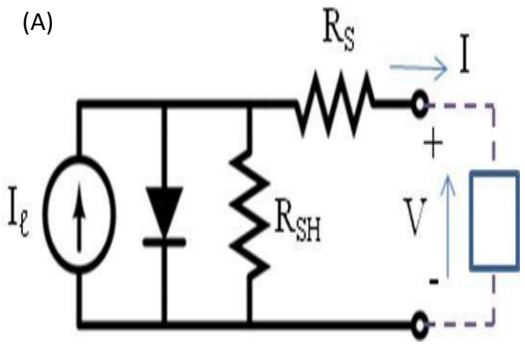

(B) $$I = I_l - I_D = I_l - I_0(e^{\frac{qV}{kT}} - 1)$$

(C) $$I = I_l - I_0(e^{\frac{q(V+IR_S)}{nkT}} - 1) - \frac{V + IR_S}{R_{SH}}$$

Figure 5.1: Circuit model of a single diode solar cell is illustrated by (A). (B) and (C) are the current as a function of voltage and the parameters that effect the net current within a solar cell. These parameters are discussed in this chapter.

5.1.1 Short Circuit Current I_{SC}

The short circuit current corresponds to the short circuit condition when the impedance is low and it is calculated when the voltage is zero. It is the current that flows throughout the external circuit of the solar cell when the electrodes are short circuited. The current is equal to I_{SC} when the voltage is zero. For an ideal PV cell I_{SC} is equal to the total current produced in the PV cell by photon excitation. It is noteworthy that the current moving through the solar cell is dependent on the area of the solar cell. To remove this factor of area the short circuit current density is used, which is denoted J_{SC}. If we were to consider the ideal case the J_{SC} is equal to J_{ph}[4]. If we consider the total current density under illumination of a p-n junction with J_0 as the saturation current density we obtain the following

$$J(V_a) = J_{rec}(V_a) - J_{gen}(V_a) - J_{ph} \quad 5.1$$

$$J(V_a) = J_0[e^{(\frac{eV_a}{kT})} - 1] - J_{ph} \quad 5.2$$

the photo-generated current density value of a simple p-n junction with a uniform generation rate G is given by

$$J_{ph} = eG(L_N + W + L_P) \quad 5.3$$

W represents the width of the depletion region and L_P and L_N is the minority-carrier-diffusion length for the holes and electrons respectively. The above equation means that

only charge carriers generated in the region of the minority-carrier-diffusion lengths of electrons and holes as well as the depletion region contribute to the photo generated current.

5.1.2 Open Circuit Voltage V_{OC}

This voltage occurs when there is no current passing through the external circuit of the solar cell, and is also the maximum potential difference across the cell for a forward-bias sweep within the power quadrant. The open-circuit voltage is dependent on the photo-generated current density and is given by the equation below given that the current in the external circuit is zero

$$V_{OC} = \frac{kT}{e}\ln\left(\frac{J_{ph}}{J_0}+1\right) \tag{5.4}$$

since the saturation current J_0 has a direct relation to the recombination within the solar cell. Thus the open circuit voltage is a measure of the amount of recombination within the solar cell device [4].

5.1.3 Maximum Power P_{MAX}

Using the relation for power $P=IV$ we can solve for P_{MAX}. The power will be zero at an open circuit voltage and short circuit so the maximum power is between these values. Figure 5.2 below gives the relation between the power, current and voltage.

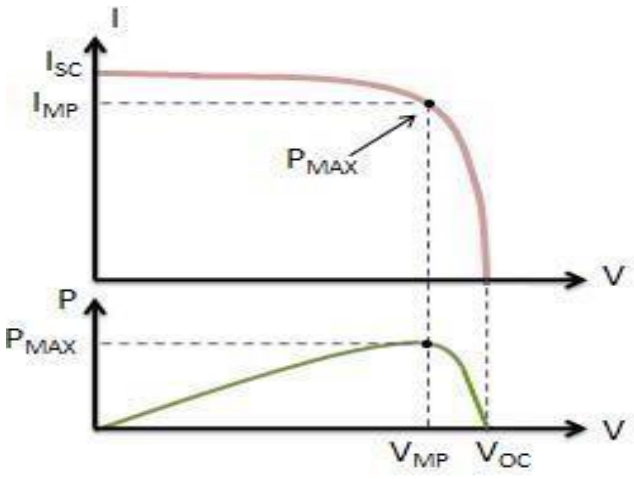

Figure 5.2: I-V sweep for maximum power as illustrated by the green line in the figure. The maximum power is the largest rectangular area within the IV curve.

5.1.4 The Shunt Resistance (R_{SH}) and Series Resistance (R_S)

The efficiency of a solar cell is reduced by the dissipation of power due to internal resistance within the circuit. These resistances can be modelled as R_{SH} and R_S. In the ideal case R_{SH} would be infinitely large as to restrict the current to one path in which to flow, the R_S in this ideal case would be zero resulting in no voltage drop before the load.

The main contributors to the series resistance R_S are the metallic contacts, the contact resistance between the semiconductor and the metallic contact, the carrier transport through the top diffused layer and the bulk resistance of the semiconductor material [2,4,11].

As for the Shunt resistance R_{SH}. This resistance is a result due to the p-n junction and impurities near the junction which cause partial shorting of the junction, usually near the cell boundaries.

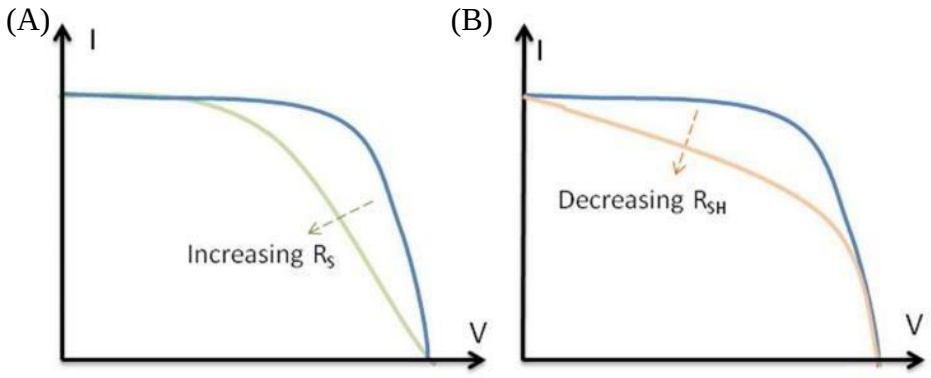

Figure 5.3: Diverging and R_S from ideal case. Effect on fill factor (A) and maximum power (B).

5.1.5 The quality of a photovoltaic cell

There are two more parameters which we can use to evaluate the quality of our photovoltaic cells. The first is the fill factor and the second is the efficiency.

The fill factor: This quantity is calculated by comparing the maximum measured power (P_{max}) with the theoretical power (P_T=$V_{oc}I_{sc}$) that would be output at both the short circuit current and the open circuit voltage together shown in figure 5.4. The average fill factor values range from 50 % to 80 %. We can also graphically interpret the fill factor by the ratio given below:

$$FF = \frac{P_{MAX}}{P_T} = \frac{I_{MP}V_{MP}}{I_{SC}V_{OC}} \qquad 5.5$$

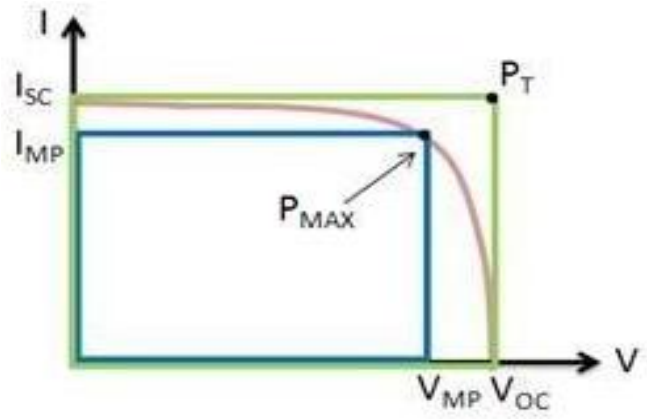

Figure 5.4: Calculating the fill factor from an I-V sweep.

If the solar cell behaves as an ideal diode then the fill factor of the cell can be expressed as a function of the open-circuit voltage V_{oc} and is given by

$$FF = \frac{v_{OC} - \ln(v_{OC} + 0.72)}{v_{OC} + 1} \qquad 5.6$$

where v_{oc} is the normalised voltage given by

$$v_{OC} = V_{OC}\frac{e}{kT} \qquad 5.7$$

the fill factor is practice is lower than predicted values due to the presence of parasitic resistive losses [10].

Efficiency: The ratio between the electrical power output and the solar power input into the photovoltaic cell. We denote it by the symbol η [11].

$$\eta = \frac{P_{out}}{P_{in}} \rightarrow \eta_{\max} = \frac{P_{\max}}{P_{in}} = \frac{J_{SC}V_{OC}FF}{P_{in}} \qquad 5.8$$

for standard measurements the incident power has a value of 1000 W/m^2 which corresponds to the AM 1.5 spectrum as discussed in chapter 3 [4].

5.1.6 Quantum Efficiency

The quantum efficiency (*QE*) is the ratio between the number of carriers collected or absorbed by the solar cell and the number of photons that are incident on the solar cell from the photon source. It may be given as a function of energy or wavelength of the incident light. Photons with energy less than the energy gap are not absorbed and thus the *QE* is zero as shown in the figure 5.5 below. For an ideal solar cell the *QE* is unity as illustrated by the gold line in the figure below. However this is not the case for real solar cells as the *QE* is reduced by recombination effects and reflection. Reflection reduces the *QE* for all wavelengths. Recombination effects can, however, effect certain wavelengths more than others. The blue region or high energy region photons are absorbed close to the surface and thus a higher concentration of front surface recombination occurs. This leads to a lower *QE* in this region. Similarly for the low energy "red" region.

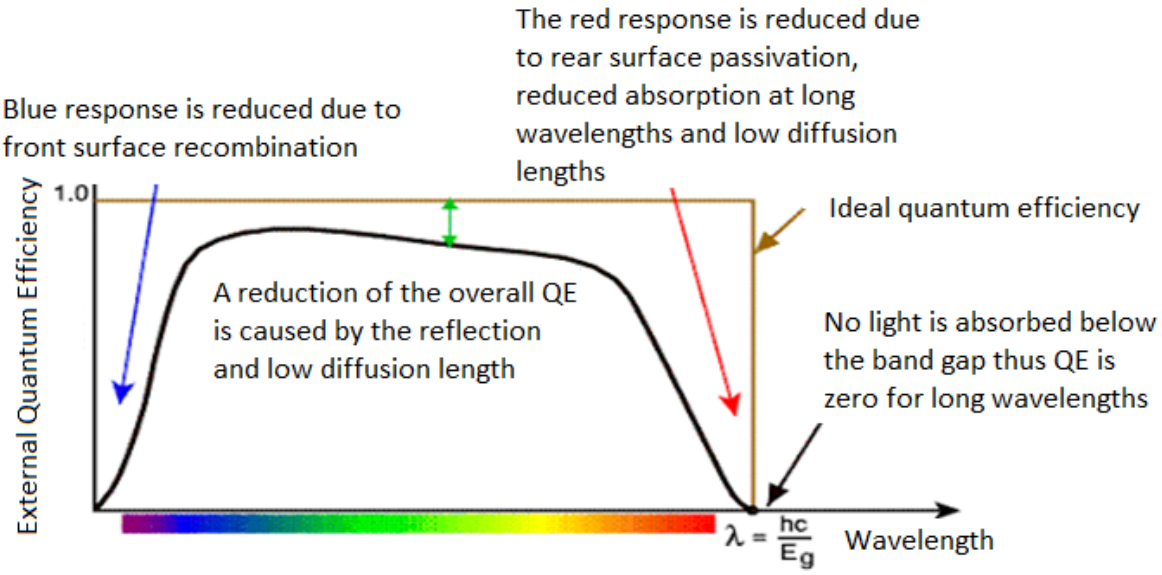

Figure 5.5: QE as a function of wavelength and the parameters that effect it [4].

5.1.7 Temperature effect on *I-V*

The effect of temperature can be seen in two parts. As the temperature increases the short circuit current increases since the electrons have more energy and more phonons have enough energy to create electron-hole pairs. This is, however, a very small effect. The second part is the open circuit voltage. The open circuit voltage decreases as the temperature increases, thus the cells power output decreases. This second effect is much larger than the first effect. Since the second effect is dominant. Thus as the temperature increases the cell output decreases. These effects are illustrated by the figure 5.5 which was obtained from my previous project.

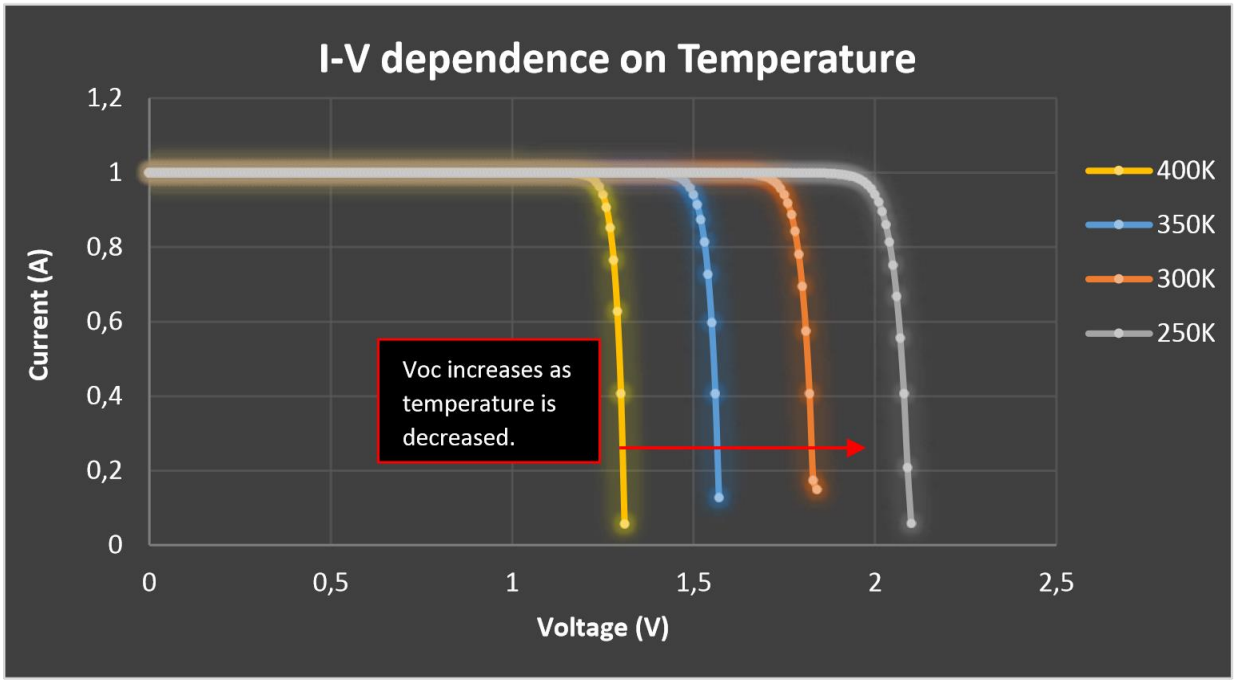

Figure 5.6: Temperature effect on the *I-V* characteristics of a solar cell between 250 K and 400 K.

CHAPTER 6

EXPERIMENTAL

6.1 SAMPLE PREPARATION

The solar cells that were studied in this project range from inorganic simple p-n junction silicon solar cells to organic inversion layer n-Si/PEDOT:PSS solar cell. For simplicity the production and sample preparation of a single solar cell will be discussed in this section as the preparation methods of the other solar cells are mostly similar.

The sample we will consider is the n-type Si/PEDOT:PSS inversion layer solar cell. This solar cell was prepared from the fundamental components. The sample size is approximately 1 cm by 1 cm giving an area close to $1\,cm^2$. In this section the preparation of the silicon organic solar cell will be discussed. The *I-V* experimental setup and the Hall Effect measurement experimental setup will also be discussed in detail in this chapter.

6.1.1 Cleaning

The construction of the silicon solar cell requires that the silicon first be cleaned. Using a Magnetic Stirrer and Hotplate HS31 as the boiling instrument the method used to degrease and clean the silicon sample is described below.

Step 1: Boil the silicon sample in acetone for 5 minutes.

Step 2: Boil the silicon sample in ISO (isopropan-2-ol) for 5 minutes.

Step 3: Boil the silicon sample in methanol for 5 minutes.

Step 4: Boil the silicon sample in deionised water for 5 minutes.

Step 5: Dip the sample in 40 % concertation HF for a duration of 1 second to remove the oxygen from the sample surface then immediately blow dry the sample with nitrogen gas.

6.1.2 Spin coating

The next step in the production of the solar cell is the deposition of the PEDOT:PSS layer on the silicon sample. In this experiment a method known as spin coating was used to produce the PEDOT:PSS thin layer. The mixture of the PEDOT:PSS used in this experiment was diluted with water in the following ration 3:1 with 3 parts PEDOT:PSS to 1 part distilled water. The silicon sample was place on the sample holder and then a vacuum was applied thus the sample was in place. Two drops of the PEDOT:PSS solution was applied to the sample. The spin-coater was closed and then the process was activated the static spin coating had 3 stages. The first was the increasing of the RPM the second was the spinning of the sample at 3000 RPM for 1 minute and the last stage was the reducing speed stage until the sample stopped spinning. The solution in stage two spread evenly over the sample and a uniform layer was achieved. The sample was then removed and placed in an oven at a temperature of 373 K for 1 minute. If an additional layer was required then the procedure was repeated until the desired thickness was achieved. In this experiment three layers of PEDOT:PSS were applied to the silicon sample.

6.1.3 Deposition of metallic front contact

The deposition of the metal contact was done using an Edwards AUTO 306 resistive vacuum deposition machine. The contact was made using aluminium (Al) at a density of 2.7 gcm^{-3} and an acoustic impedance of $8.17 \times 10^5\ gcm^{-2}s^{-1}$. The deposition rate was kept at a constant of 1 Angstrom per second for even distribution over the sample. The contact was deposited as a grid on the sample and the thickness deposited on the sample was 50 nm with a vacuum of approximately 5×10^{-6} mbar.

6.1.4 Deposition of back contact

For the back contact of some of the solar cells such as the n-Si/PEDOT:PSS solar cell, Indium-Gallium as used by scratching the silicon using a scalpel and applying the alloy onto the back of the silicon. Then in the *I-V* characterization experiment the solar cell was placed on a high electrical conduction foil and a copper sheet to allow the contact probes the be connected to the back contact so that measurements could be done.

6.2 *I-V* CHARACTERIZATION

The *I-V* measurements are the main part of the experiment for the characterization of solar cells since the *I-V* graphs are used to deduce and calculate very important characteristics of solar cells such as the fill factor and efficiency. The importance of these parameters were discussed in chapter 5. This section will focus on the experimental setup and execution of the current-voltage measurements of each studied cells. The entire experiment was automated using a LabVIEW program and a $Oriel^{®}LCS - 100^{TM}$ Small Area Sol1A solar simulator.

6.2.1 Setup

The *I-V* measurements were done in the electronic lab. The sample was kept in a faraday cage and isolated from the environment to prevent any factors such as light, air and dust. Using two probes that are in contact with the sample and connected to the oscilloscope. (Agilent B2912A Precision/Measure Unit 10fA, 2 channel). The experiment is set up to measure the current (*I*) and voltage (*V*) characteristics of the studied solar cells using a National Instruments LabVIEW program and a solar simulator (model: $Oriel^{®}\ LCS - 100^{TM}$ Small Area Sol1A). The dark measurements were calculated beforehand within a dark room and was isolated from any light radiating sources.

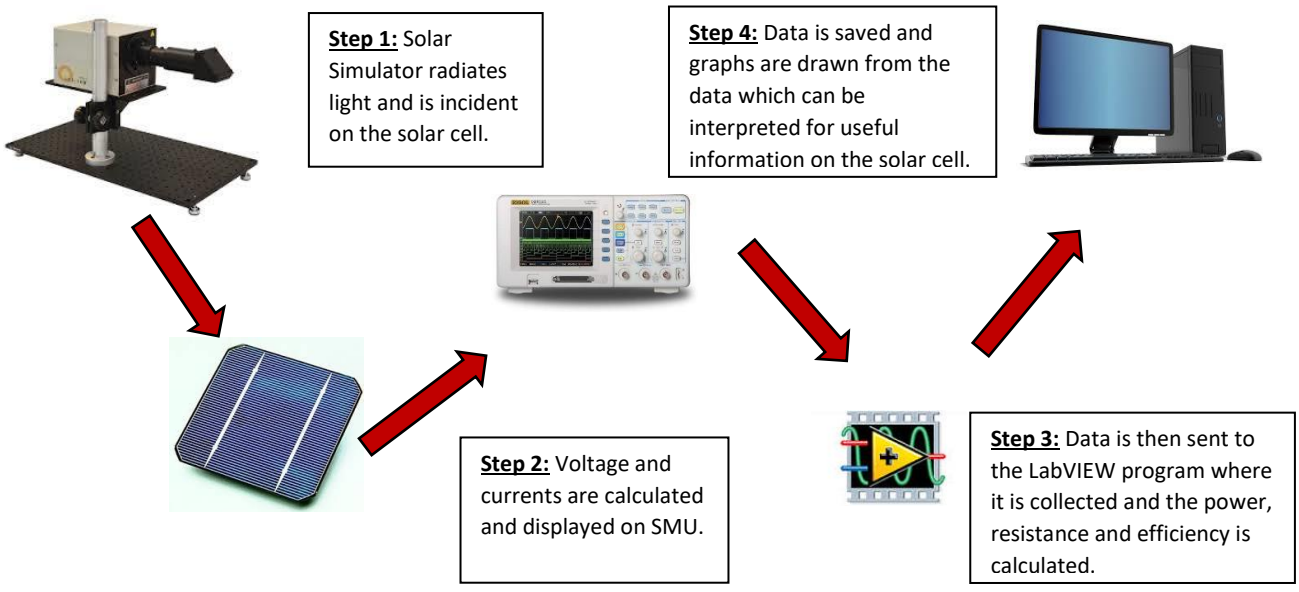

Figure 6.1: Basic diagram of *I-V* experiment outline

In our system setup the shutter of the solar simulator was controlled by a switchbox thus allowing control of the radiation intensity in suns by increasing or decreasing the size of the shutter. We can also set the solar simulator to 1 sun intensity at AM 1.5 which is approximately 1000 W/m^2. The solar simulator radiates light which travels within the tubes and is incident on the studied cell.

Using probes and placing the cell on a good conducting material, in this case a thin sheet of copper we could measure the current and voltage using cables and an SMU (Source, Measure Unit). The SMU then measured and collected the *I-V* data in voltage steps of 0.01 V from 0 to 1.4 V and calculated the shunt and series resistance. This data was sent via a connection wire to the LabVIEW program. The data was collected into an array within the program which then interpreted the measured data into graphs and calculations were made such as power, fill factor, shunt resistance, series resistance and efficiency. The program also allowed us to protect our equipment by allowing an automatic shut down if some parameters pass over the save range like the current, temperature or voltage. Also each experiment was done twice and the average was be taken of the results to reduce errors.

Using a solar simulator we calculated the effect of various parameters on the *I-V* curves such as the series, shunt resistance and temperature. These results are depicted below in the results section.

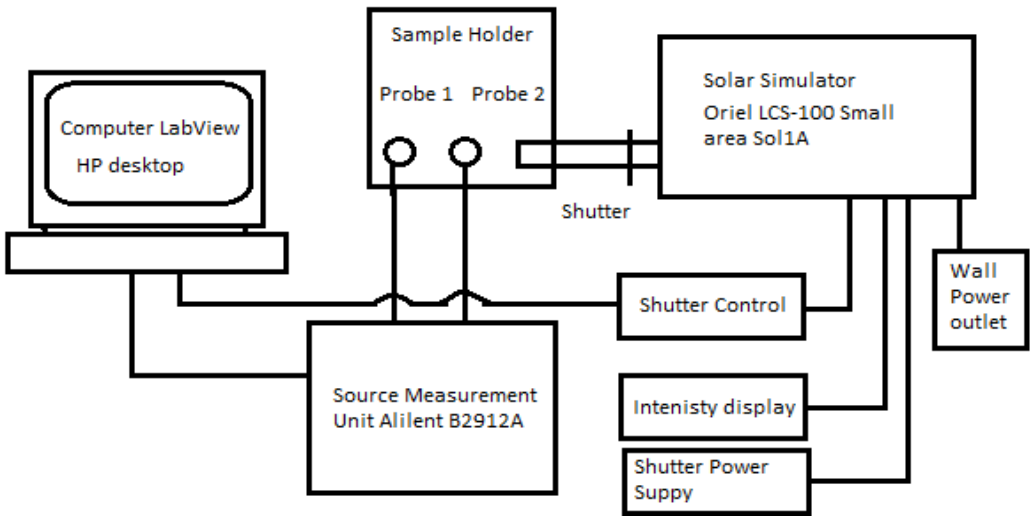

Figure 6.2: Schematic representation of the Current-Voltage characterization setup.

6.2.2 Equipment

$Oriel^{®}LCS-100^{TM}$ Small Area Sol1A:

This solar simulator has a beam size of size 38 mm x 38 mm with a working distance of range from 20 cm ± 5 cm. This device replicates sunlight for our evaluation of our solar cell.

Agilent B2912A:

This will be our SMU which has two channels with a minimum resolution of 0.01 pA and 0.1 µV. The maximum current is for a direct current (DC) ± 3.03 A and for an alternating current (AC) is ± 10.5 A pulse; with a maximum voltage ± 210 V [8].

Figure 6.3: Agilent B2912A Precision Source/Measure Unit 10 fA, 2ch and cables.

KEITHLEY 239 Programmable voltage source:

In this experiment this unit was used to apply the 5 V required by the $Oriel^{®}LCS-100^{TM}$ Small Area Sol1A for the shutter control. This allowed us to write a routine within the LabVIEW program which could open and close the shutter to form dark and illuminated conditions. The shutter control in this setup was set to the remote setting thus allowing the shutter to be controlled by the LabVIEW program.

Newport:

This device was used for one simple purpose. Since this experiment was an independent temperature experiment this unit was used to display the temperature within the sample chamber. This unit was also used to display the solar intensity of the light incident on the studied sample and this intensity was set at 1000 W/m^2 which approximately simulates the sun intensity on the surface of the earth.

Sample Holder:

A small Faraday cage was built to isolate the sample from light, dust and electric interference from any other equipment in close proximity to the sample. The cage was big enough to hold the studied sample and the 2 probes. The probes are then in contact with the front and back contact of the sample and are connected to the SMU Agilent B2912A unit. The two wires from the oscilloscope are connected to the cage via input slots and then the corresponding output terminals are connected to the probes.

6.2.3 Experiment procedure

The computer program was designed using National Instrument LabVIEW 2011 to control and execute our experiment. The sequence of the LabVIEW program is shown below.

1) Data file save location is selected by the user.
2) Parameters such as current and voltage limits, voltage increments, intensity and wait between measurements are selected.
3) Program detects if shutter is on or off and also determines if the measurements are done only for dark or illuminated or both conditions.
4) Voltage difference via oscilloscope is set over sample and current is measured and saved in an array. This is done from the start voltage in increment steps to the final voltage if none of the limits are reached.
5) If limits are reached then measurements are stopped and procedure continuous from step 6.
6) All current and voltage measurements are used and the *I-V* graph is plotted.
7) Parameters such as the shunt, series resistance, open circuit voltage, short circuit current, fill factor and efficiency are calculated and displayed.
8) Data is then saved in the data file selected in step 1 for further study.

The data in step 4 is continually updated and displayed on the second graph and can be observed throughout the measurement process.

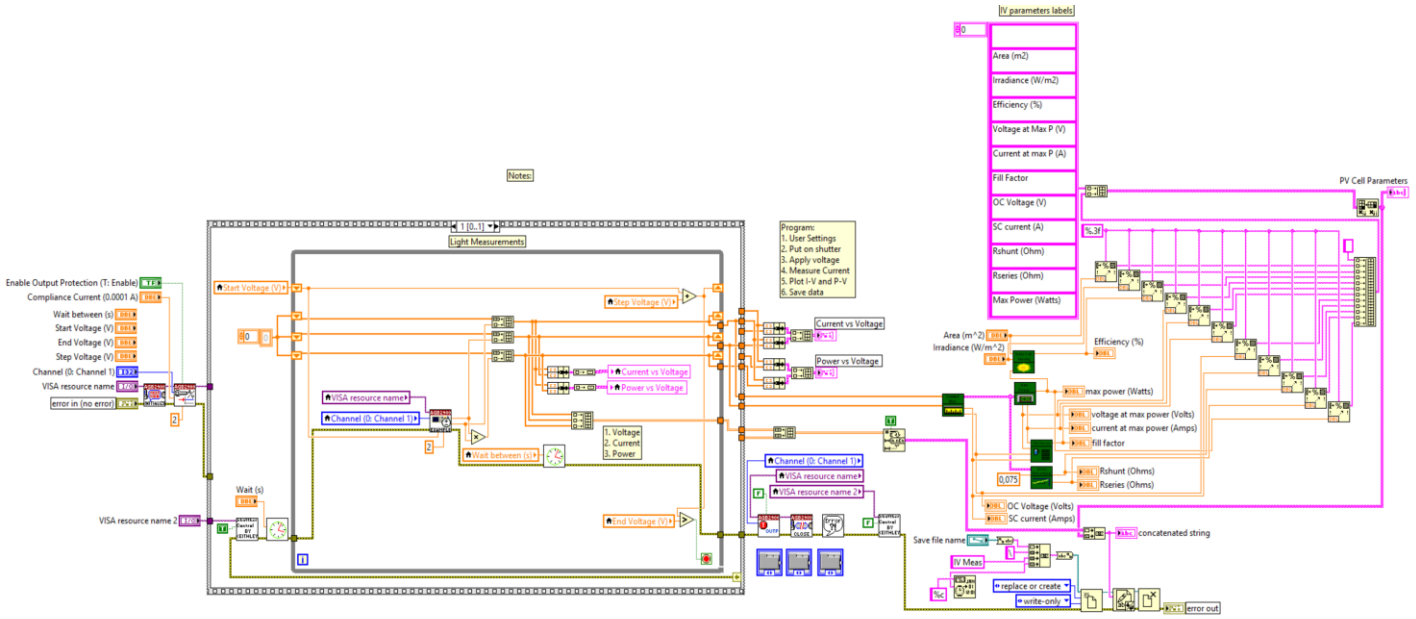

Figure 6.4: Block Diagram of the I-V measurement LabVIEW program using the $Oriel^{®}LCS-100^{TM}$ Small Area Sol1A.

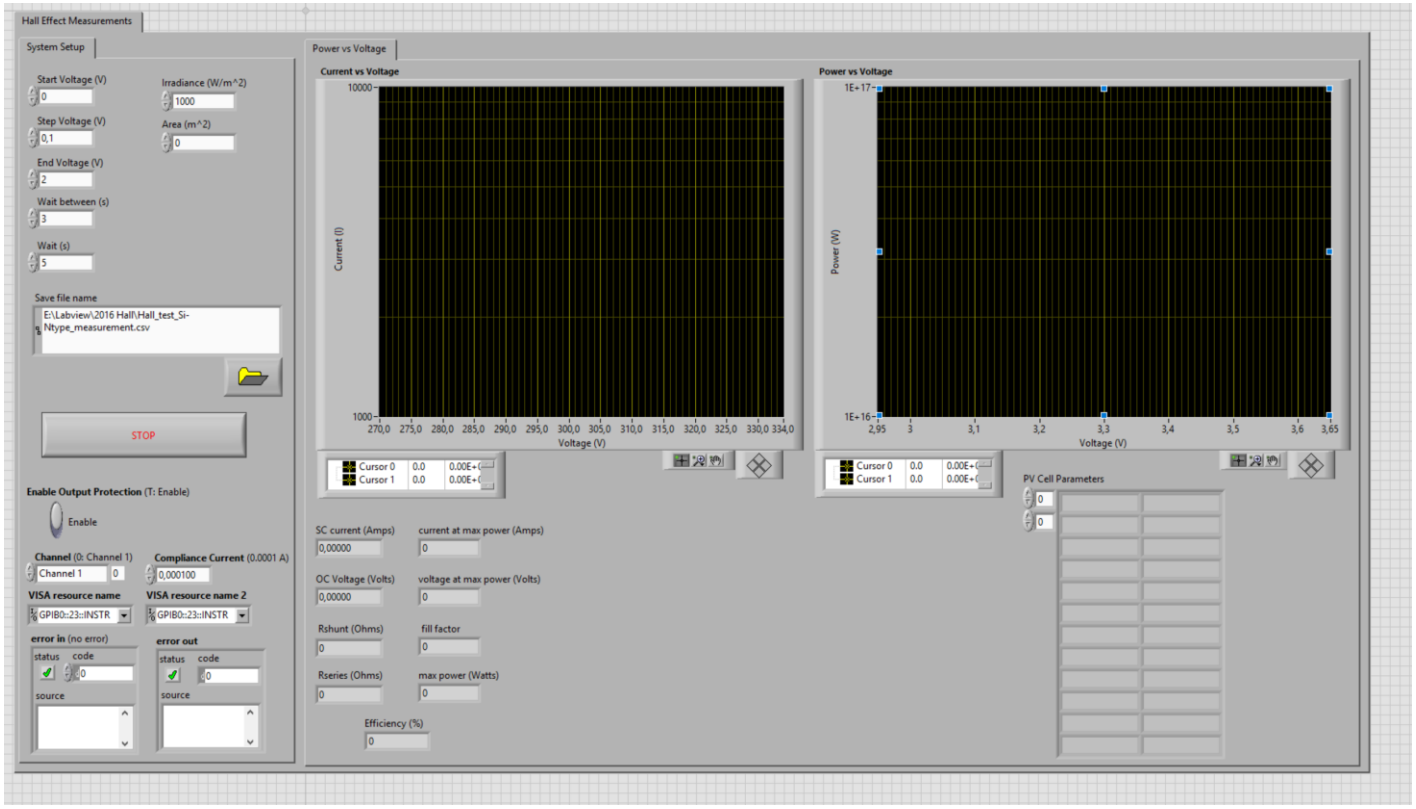

Figure 6.5: User interface of the I-V measurement LabVIEW program using the $Oriel^{®}LCS-100^{TM}$ Small Area Sol1A.

6.3 HALL EFFECT EXPERIMENT

As described in chapter 2 and 4 the resistivity, carrier concentration and the mobility are some of the most important properties of semiconductor material. These quantities are of great importance for device application. By using the *TDH* measurements these quantities can be calculated and determined. In chapter 4 it was shown that the Hall measurements can separate conductivity into carrier mobility and carrier density. These measured quantities, however, are not the true values of the carrier density and drift mobility but differ by the quantity known as the Hall scattering factor as discussed in chapter 4. The Hall measurements setup and execution is discussed in this chapter as well as the equipment used for this experiment.

6.3.1 Setup

For safety reasons and accurate measurements the entire experiment must be automated. A key component of this Hall Effect experiment is a suitable magnet. Our lab had a magnet which was made by Oxford Instruments Ltd. An HP 6030A System power supply unit was used as the current source power supply for this magnet. The HP 6030A power supply unit can only supply a voltage in one direction however by using an inverting switch unit the direction could be inverted also allowing us to invert the polarity of the magnetic field. Since the Hall measurements are temperature sensitive a cryostat with Air Products powered by a He cycle compressor was used.

For the electrical measurements two instruments were used. The first was a HP 3245A universal current source which supplied the current necessary for the Hall measurements. The second instrument was an Agilent 34970A data acquisition unit, this unit was responsible for both creating the various contact configurations and the measurements of the voltage of these configurations.

By using a software program developed in LabVIEW all the instruments except for the magnet switch unit are controlled via a GPIB interface. The magnet switch is controlled via a digital output from the data acquisition unit. The schematic representation of the Hall Effect measurements is shown in the figure 6.6.

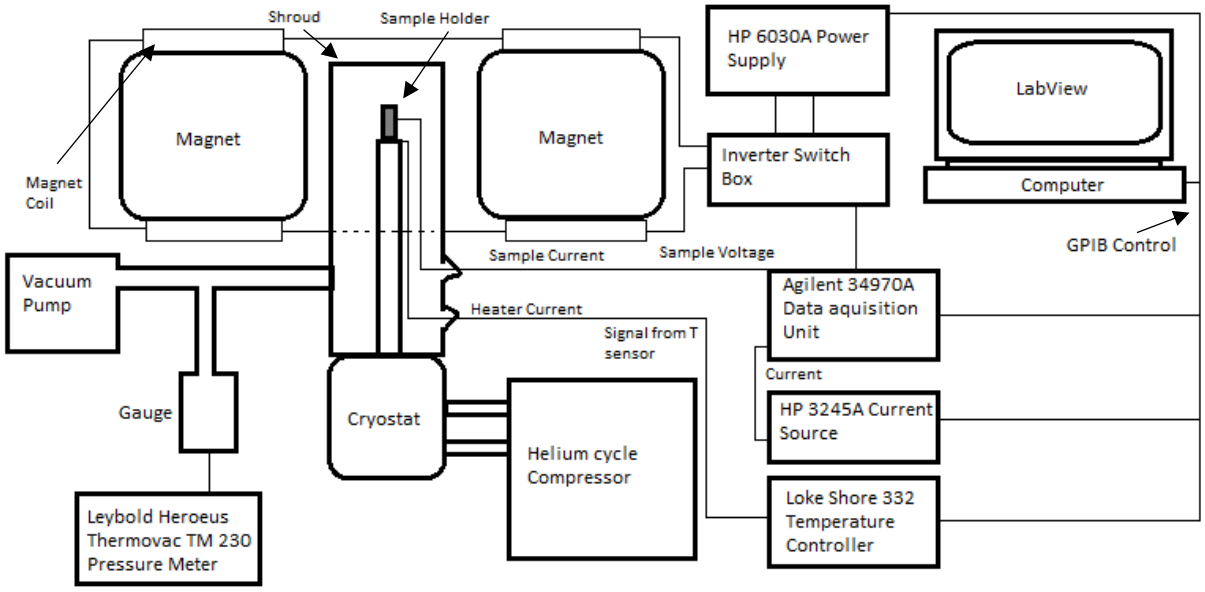

Figure 6.6: Schematic representation of the temperature dependent Hall Effect measurement setup.

The Agilent 34970A switch matrix used in this experiment setup is shown in figure 6.7. This picture is a simple illustration of how the different configurations are chosen for each Hall measurement.

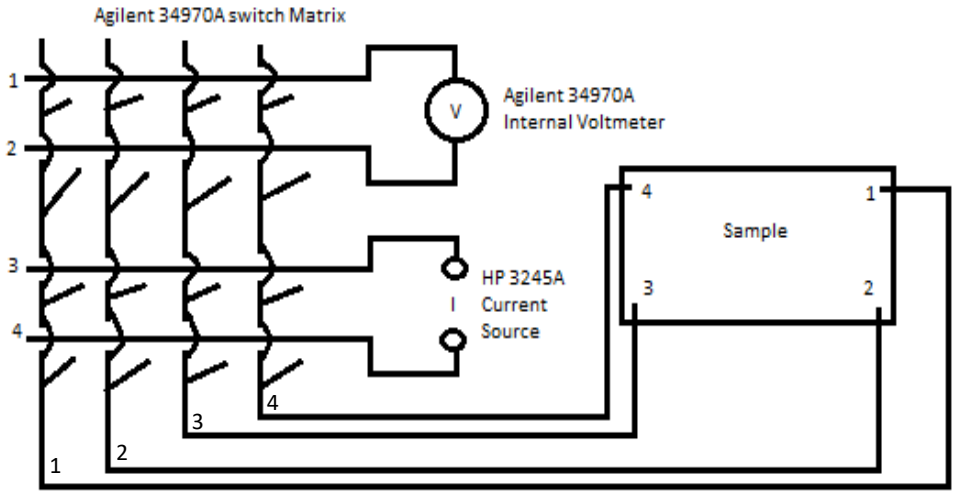

Figure 6.7: Schematic representation of the measuring component of the temperature dependent Hall Effect measurement setup.

6.3.2 Components

Current Source:

The HP 3245A Universal Source was used in this experiment as a precision DC current source. There are a few limitations that need to be taken into consideration when this unit is used. The maximum voltage output of this unit when applying a specific current is 15 V and if an attempt to apply a current that requires a voltage higher than 15 V the unit will fail to supply the current without notifying the user. For this reason it is important to check the applied voltage when this unit is used and to ensure that the voltage output of the current being supplied by this unit is within the limit of 15 V. The table below gives the error in the applied current for ranges in high-resolution mode according to the specifications of the HP 3245A unit.

Range (A)	± Error
0.00000	3.3 nA
0.00005	5.9 nA
0.0005	46 nA
0.01	0.96 µA
0.1	23.5 µA

Table: 6.1 The error in the current output of the HP 3245A.

The excitation current applied to the sample should be small enough to stay within the desired voltage range. The current should also be sufficiently small due to sample heating. However the applied current should also be large enough to produce a measurable Hall voltage. Depending on the samples resistance used in the experiment the currents in the range of $10^{-8}\ to\ 10^{-1}$ A of the current source was used in this experiment. It is worth noting that the resistance of the sample changes with temperature thus the applied current must be adjusted as the temperature changes to remain in the desired voltage range.

Voltmeter and Data acquisition unit:

A HP34970A Agilent voltmeter was used in this experiment. The internal voltmeter output voltage values averages over an integer number of power line cycles (PLC's). This reduces the noise which originates from the 50 Hz mains power cycle.

Integration Time	Resolution (V/Range)
1 PLC (0.02 seconds)	0.000003
2 PLC (0.04 seconds)	0.0000022
10 PLC (0.2 seconds)	0.000001
20 PLC (0.4 seconds)	0.0000008
100 PLC (2 seconds)	0.0000003
200 PLC (4 seconds)	0.00000022

Table: 6.2 Maximum voltage resolution as a function of integration time.

The range and resolution for the Agilent 34970A can be selected in the computer program before measurements are executed. By preselecting the voltage range more reliable results could be obtained than allowing the voltmeter to auto-select the range.

In this experiment the Agilent voltmeter/ switch unit was set in monitor mode rather than scan mode. Monitor mode enables more precise control over the time intervals between the matrix switching and the voltage measurements which allows sufficient time for each configuration to be selected and the current to stabilize and accurate voltage measurements to be obtained. The 1 V and 10 V ranges were used in this experiment. When choosing a voltage resolution two factors must be considered. A high resolution is required, however, a high resolution requires a longer integration time as seen in table 6.2 but a longer integration is not desirable since it can result in increased thermomagnetic errors. In this experiment an integration of 100 PLC was used.

A delay time between applying the current to the sample and measuring the voltage could be selected by the user in the computer program. Another factor to consider is the electrical power applied to the sample which is the product between the applied current and voltage. Again to high voltage results in sample heating but a high enough voltage is required for good measurability.

Magnets and Magnetic Power Supply:

In this Hall Effect measurement setup a HP 6030A power supply was used to supply the magnets with the desired current. This power supply is rated at 1000 Watts with a maximum current and voltage at 17 A and 200 VDC respectively. However this power supply can only supply current in one direction so a switch box was used to invert the polarity of the magnetic field. A table was created with the magnetic field strength and the corresponding current required to obtain this magnetic field strength. To ensure the protection of the instruments used in this setup a magnetic field strength of 0.5 T was used. To obtain this magnetic field strength a current and voltage of 7.29 A and 70 V respectively was used. These values are well below the limits of each instrument.

The magnets used in this experiment was manufactured by Oxford Instruments Ltd., the trolley mounted magnet features water-cooled magnet coils and retractable magnet poles to adjust the distance between the two magnetic poles. The continuous current limit of the magnet without water-cooling is 7 A and with water-cooling is 12.5 A. A continuous magnetic field strength of 2.6 T can be achieved depending on the pole separation and types of poles used. In this experiment setup, 10cm diameter plane tip poles were used at a separation of 4.5 cm to allow the cryostat to easily fit between the poles while keeping a distance to allow for a uniform magnetic field within the sample.

The magnet used in this setup has a large inductive reactance, due to this it is not wise for the HP 6030A to supply the desired current instantly since it applies undue strain on the device. To prevent this a routine was programmed to ramp up the current in increments of 0.1 A until the desired current is reached. This routine takes approximately 10 seconds to complete. As the magnetic field is ramped up or down an electric field is induced which in turn destabilizes the thermocouple for a short amount of time. To prevent an inaccurate temperature measurement

a delay was set within the program to allow the magnetic field to stabilize before the measurements are done. The delay used in this experiment ranged from one to two minutes.

Lake Shore 332 Temperature controller:

The Lake Shore 332 temperature controller was used in this experiment setup. The temperature unit has three power settings: Low (0.5 Watts), medium (5 Watts) and high (50 Watts). In the study the high setting was used for temperatures above 40 K. This temperature unit has two temperature sensor inputs, one for a diode sensor and another for a thermocouple. Both of these sensors were used in this experiment. A standard Chromel versus AuFe thermocouple with 0.07 % Fe was used for the temperature control unit. The thermocouple was embedded in indium metal at the tip of the cryostat shaft where the sample holder attachment point is also found. Fast and stable temperature control is achieved. The Lake Shore 332 temperature control employs a standard PID (Proportional-Integral-Derivative) control algorithm. In this experiment setup the PID was set at the following values the P and I values were 300 and 200 respectively due to the fast feedback and the D was set to zero. Since the thermocouple and sample are not at exactly the same position and that thermocouples are intrinsically quite inaccurate, a dual sensor approach was adopted. A LakeShore DT-470-SD-13 silicon diode sensor was also included in the setup. The sensor was mounted on the rear side of the sample holder below the position of the studied sample which therefore gave much more accurate temperature readings. The sensor is useful in the temperature range of 1.4 K to 500 K and an accuracy of 1 K is specified.

There is one issue to consider within the temperature part of this setup and that is the time required for the systems temperature to stabilize. The sample is not so tightly coupled to the system as the temperature sensor. To ensure that this issue does not affect the accuracy of the measurements a large delay time was employed between the temperature set point and the measurement procedure. A delay of about 10 to 15 minutes was sufficient enough to obtain accurate measurements. If the temperature measured is in an error of 0.05 K of the desired temperature for one minute then the measuring procedure is executed.

Sample Holder:

A new sample holder was made to simplify the insert and removal of the samples. The temperature sensor was placed next to the sample to accurately measure the temperature. The sample holder has a restriction on the sample size which has a maximum area of 1 cm by 1 cm.

Helium compressor and cryostat:

A closed helium cycle compressor by APD Cryogenics, model HC-2, was used in this setup to power an Air Products displacer-type cryostat. Since this equipment was already in the lab it was not necessary to modify this part of the experimental setup. The oils of both the vacuum pump and compressor were checked and renewed when required.

Vacuum system:

The vacuum system in the setup consists of a Varian SD-90 piston pump connected to the cryostat. The shroud encloses the vacuum chamber and the vacuum monitoring system which comprises of a Leybold Heraeus (LH) pressure sensor which is connected to a LH Thermovac 230 pressure meter. The shroud fits on the cryostat via a double O-ring seal. When the cryostat is active a vacuum of 10^{-3} mbar was achieved at temperatures below 50 K due to gas freeze-out. When the cryostat is not active a vacuum of 10^{-2} mbar is achieved.

6.3.3 Experiment procedure

The computer program was designed using National Instrument LabVIEW 2011 to control and execute our experiment. The sequence of the LabVIEW program is shown below.

1) Experiment conditions are manually selected by user, these conditions include the temperature range, current, average measurements, time delay and sample thickness.
2) The 4 probe contact test is done to ensure that there is electrical contact with the sample for each probe. If proper contact is not achieved the user is notified and can correct the contact error.
3) The temperature unit Lake Shore 332 is configured and desired temperature is set.
4) Volt meter and switch matrix, the HP34970A unit is configured, which allows the different configurations to be selected and desired voltage measurements to be done.
5) The HP3245A current source is activated and desired current is calculated and adjusted to protect the equipment and then the current is applied to sample.
6) The 8 resistance measurements are done with a 5 second delay between each measurements and an average of 3 for each configuration is done.
7) The magnetic field is generated by activating the HP6030A magnet current source and the magnetic field is ramped up.
8) The 4 Hall measurements are done for a positive magnetic field direction.
9) The magnetic field is ramped down until there is no current flowing through the magnet.
10) The polarity of the magnetic field is changed and the magnetic field is ramped up.
11) The 4 Hall measurements are done for a negative magnetic field direction.
12) The temperature is measured at the second sensor.
13) The data is stored in an array and the mobility, carrier density and resistivity is calculated, data is plotted and the data is saved in selected file and location.
14) Return to step 3 for next temperature, if temperature is equal to final temperature the program is stopped and data is saved.

The entire program is automated and the data and the graphs are continually updated and can be viewed throughout the measurement process.

The figure 6.8 and 6.9 below represent the front panel and the block diagram for the Temperature dependent Hall measurement program which was programmed using LabVIEW 2011. SubVI programs were also written and used within the main program such as the contact test and Cal n, u, p which are the programs to test if there is a good contact before measurements proceed and calculate the mobility, resistivity and carrier density respectively. Other SubVI programs such as the temperature control and magnetic switch were adapted from previous systems and modified for this program.

The equipment used in this experiment have their own limitation and these limitations were discussed earlier in this chapter 6. Table 6.3 are the limitations observed during and after measurements were done.

Limitation	Comments
305 K Limit	The lake shore 332 was used as the temperature control. A 305 K limit was observed due to the cryostat pump and compressor. The sensor A placed within the cryostat measured an increase in temperature above 305 K. Where the temperature sensor B which was at the sample measured a limit of 305 K.
25 K Limit	The cryostat and compressor used within this system has a lower limit of 25 K.
Resistance Limit	Sample contact resistance should not be above 1.5 K ohm. Since ohmic contacts are required for accurate *THD* measurements.
1 Tesla Limit	The power supply used to power the magnetics only allowed for magnetic fields lower than 1 Tesla.
Sample size Limit	Due to the very limited sample within the sample holder, the samples could not be larger than 1cm x 1cm.

Table 6.3: Additional restrictions of the *TDH* measurement system.

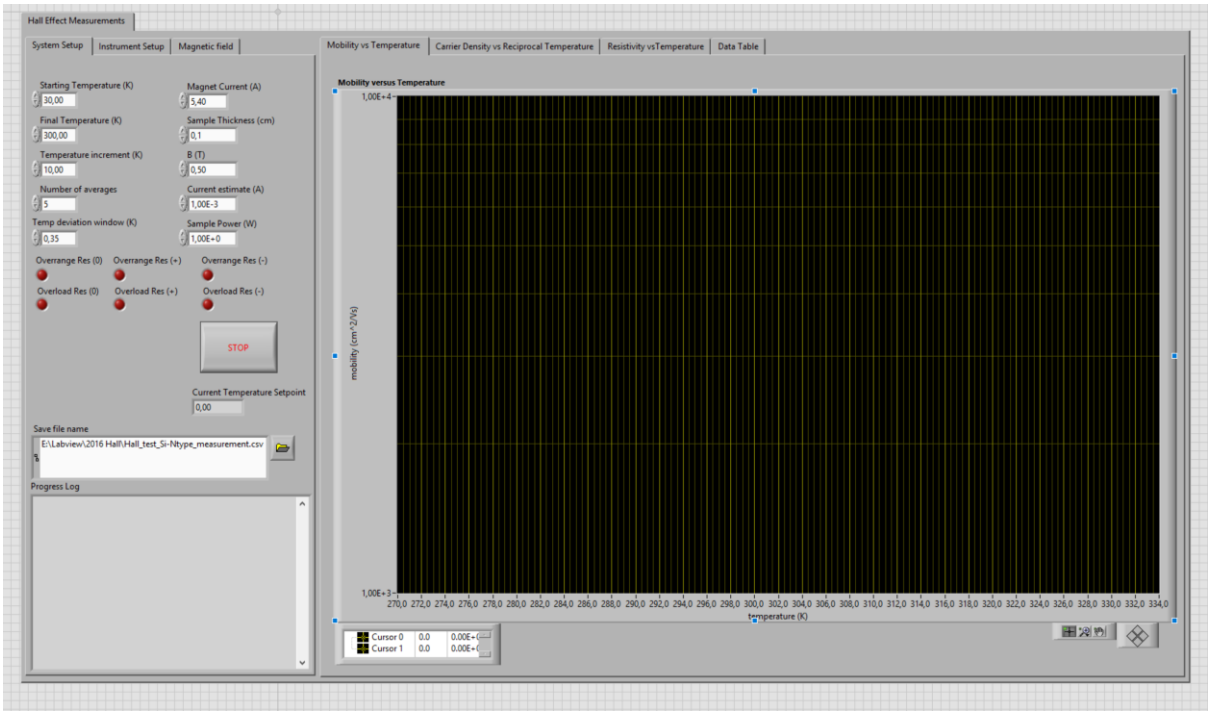

Figure 6.8: The front panel of the *TDH* measurement program in LabVIEW 2011.

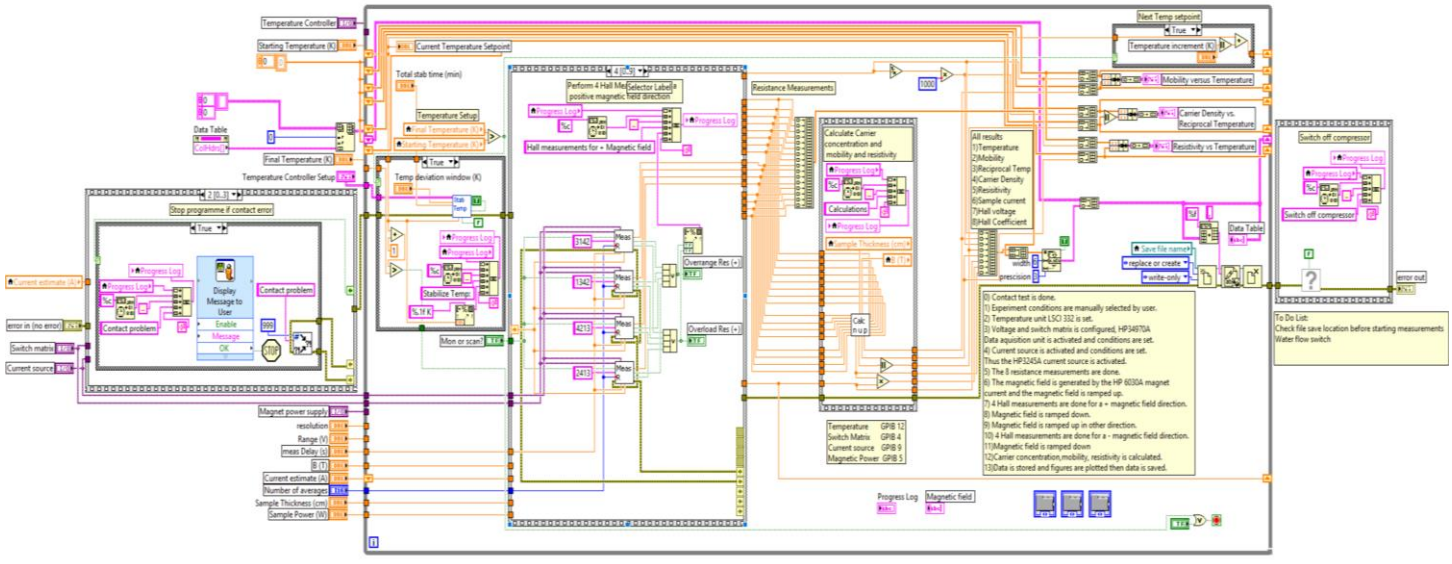

Figure 6.9: The block diagram of the *TDH* measurement program in LabVIEW 2011.

CHAPTER 7

RESULTS

7.1 HALL MEASUREMENTS

In this section the Temperature dependent Hall measurements are shown and discussed. The experiment was executed by the *TDH* measurement experiment as discussed in the previous chapter. The temperature range used in this experiment was 30 K to 300 K with increments of either 5 K or 10 K as soon as the temperature reached the desired set point the sample chamber was allowed to stabilize for 5 min before measurements were taken. The thickness of the n-Si, n-Si with Al_2O_3 and n-Si/PEDOT:PSS samples were taken to be $1\,\mu m$ where the Al_2O_3 and PEDOT:PSS layer thickness was taken to be 100nm. GaAs samples were also measured one being a p-type and the other an n-type. The perovskite solar cell thickness was 4 mm. The magnetic field applied to do the Hall measurements was kept constant at a value of 0.5 T. It was also noted that if the applied current is to large when measurements are done on a sample with more than one layer such as the n-Si with Al_2O_3 that the current will not only flow through the studied later but the n-Si as well. Thus for accurate measurements and characterization various currents from 1 to 100 micro-Ampere were applied to samples with more than one later layer.

7.1.1 Studied Sample

In this project various samples were studied and measured. The first is n-type silicon. The silicon is doped with phosphorus, the second is the same n-type silicon with a layer of aluminium-oxide (Al_2O_3).The next sample is complete solar cell, a n-type Si/PEDOT:PSS inversion layer solar cell which was made by myself in the lab. This cell was made on the same n-type silicon as sample one and the PEDOT:PSS was mixed with a 2:1 concentration. The PEDOT:PSS material has an energy gap of 1.6 eV [3]. Further details of this solar cell was discussed in chapter 3. The next sample was PEDOT:PSS on glass. Gallium Arsenide (GaAs) was also measured in the *TDH* experiment. There were two GaAs samples. One was a p-type GaAs and the other was an n-type. The thickness of these GaAs samples were 0.3 mm. GaAs

has a band gap energy of 1.424 eV. The first material used to construct the n-Si/PEDOT:PSS inversion layer solar cell studied in this project is the n-type silicon (Si) with an energy gap of 1.12 eV. The Hall measurements of this material is discussed in this section. The n-type Si with Al_2O_3 was also investigated to establish how the additional layer of Al_2O_3 on the n-type silicon changes the electrical properties of the material and if this layer could potentially improve the performance of solar cells. Now that we have investigated the n-type silicon that was used to make the solar cell, the PEDOT:PSS was applied to the silicon and thus the solar cell is created.

7.1.2 Hall Measurement

In this section the Hall measurements are done to calculate the mobility, carrier concertation and resistivity of these materials and the solar cell. Each parameter will be discussed respectively for all measured samples. A smoothing algorithm was used on the obtained mobility and carrier concertation measurements to average out any single "inaccurate" measurements which may have occurred due to weak contacts during the measuring procedure. These inaccurate measurements were results due to the vibration of the cryostat and the thermal expansion of the probes and sample holder.

Before the measurements were done on the discussed samples, measurements at different magnetic fields and currents were done to illustrate the effect of these to parameters on the measurements. These effects are shown in figure 7.1. It can be seen that the magnetic field or current applied does not affect the resistivity and in turn the hall mobility and carrier concentration. The only parameter that effects these quantities is the temperature of the sample as desired. The sample used to measure these effects was a n-Si substrate with PEDOT:PSS spin coated on the n-Si. Three layers was spin coated for an approximate thickness of 100 nm.

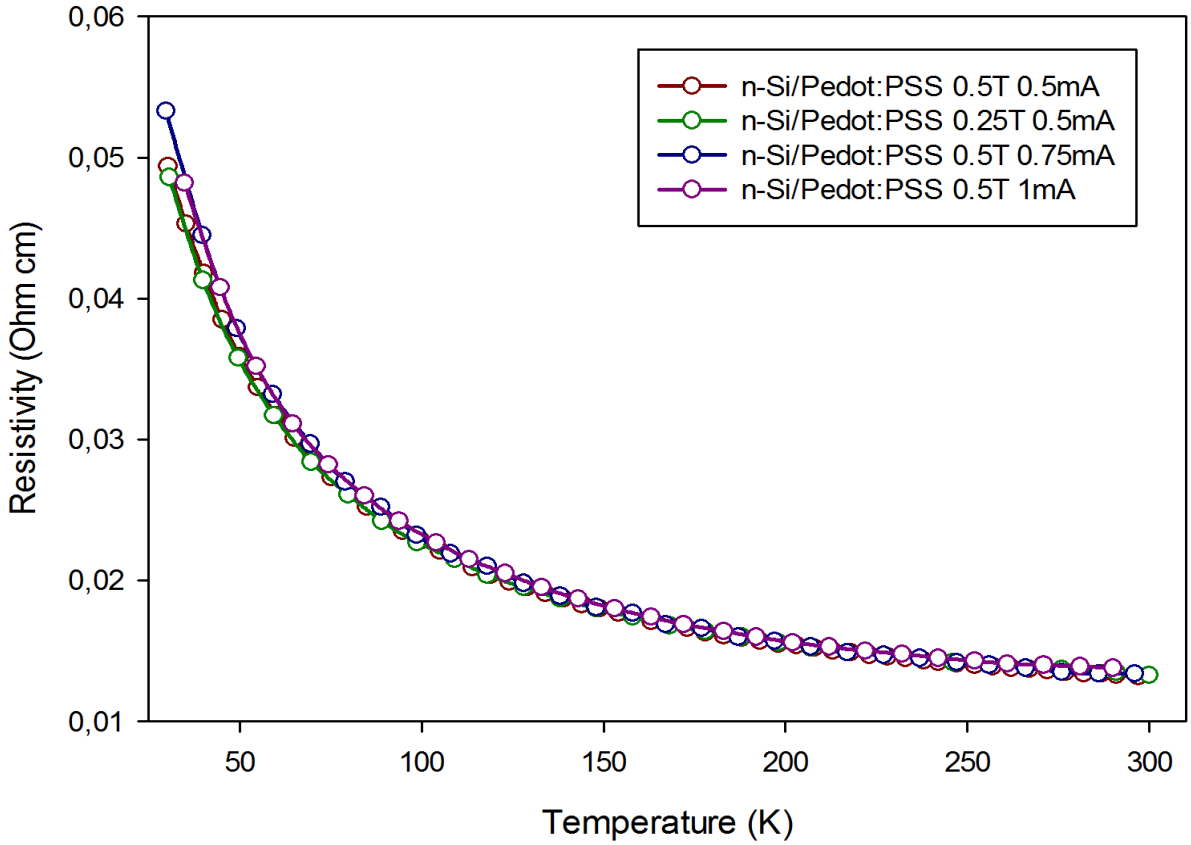

Figure 7.1: The resistivity vs temperature for studied n-Si/PEDOT:PSS with a thickness of 100 nm sample from 30 K to 300 K. The measurement was done at 0.25 T and 0.5 T with a current of 0.5 mA and again at 0.5 T with currents of 0.5 mA, 0.75 mA and 1 mA. Resistivity value at 300 K is 0.014 Ohm.cm.

Hall Mobility:

There are two basic scattering mechanisms that influence the mobility of these charge carriers namely acoustic scattering and impurity scattering. There are in some cases other sources of scattering which might be important. For non-polar semiconductor materials such as Ge and Si acoustic phonon scattering is dominant. For polar materials like GaAs optical-phonon scattering is significant [2].

As the temperature increases we observe from the measurements of n-Si as indicated by figure 7.2, that the mobility decreases. This is a result from acoustic phonons and ionized impurities within the material which result in carrier scattering [9]. From the literature the mobility due to acoustic phonons, μ_l, and ionized impurities, μ_i, are given by the equations below.

$$\mu_l \sim (m^*)^{-\frac{5}{2}} T^{-\frac{3}{2}} \qquad 7.1$$

and

$$\mu_i \sim (m^*)^{\frac{-1}{2}} N_l^{-1} T^{\frac{3}{2}} \qquad 7.2$$

and then a combined mobility of

$$\mu \sim \left(\frac{1}{\mu_l} + \frac{1}{\mu_i}\right)^{-1} \qquad 7.3$$

thus the mobility decreases with temperature and effective mass for acoustic phonon scattering and for ionized impurity density the mobility decreases with an increase in impurity density and effective mass. These relations are deduced from equation 7.1 and 7.2.

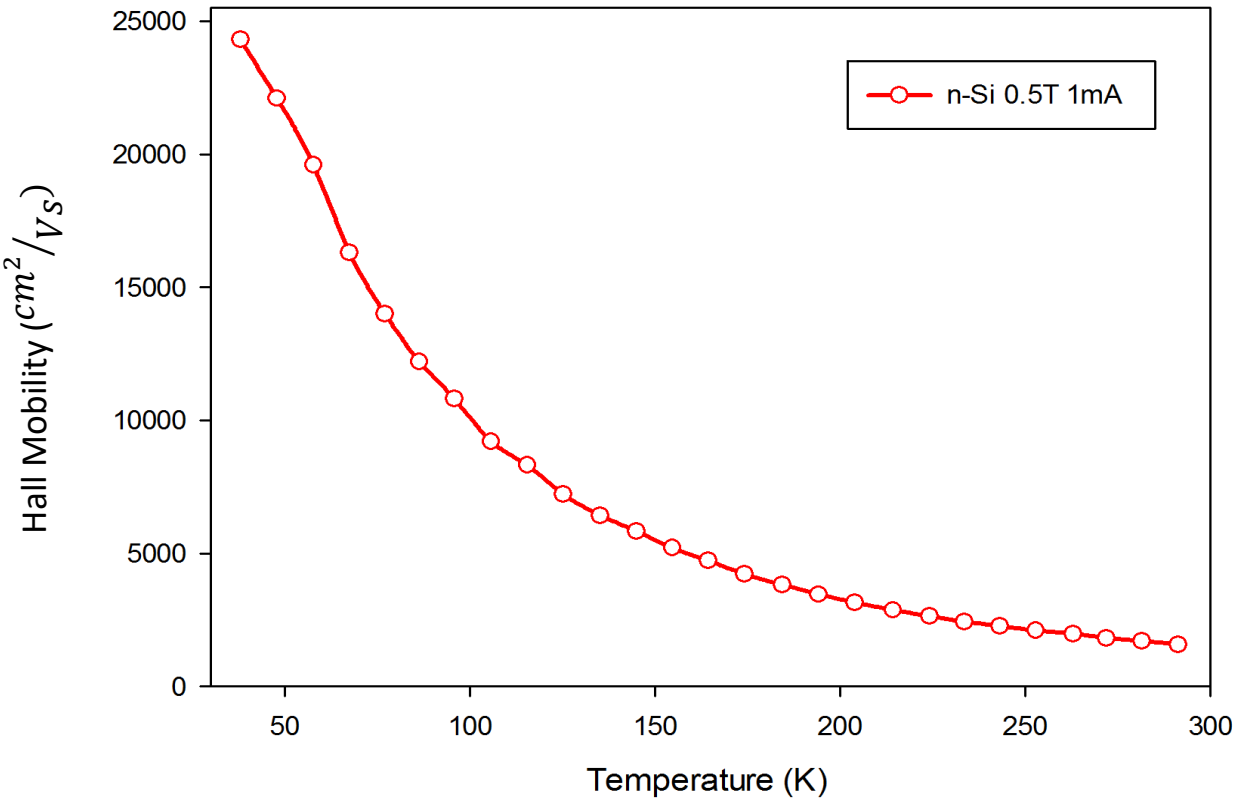

Figure 7.2: The hall mobility vs Temperature for studied n-Si sample from 30 K to 300 K. With a hall mobility of approximately 1400 $cm^2(Vs)^{-1}$ at 300 K.

To explain acoustic scattering effect in a simple way is to understand that like electrons, phonons can be considered as particles. Thus a phonon can interact (collide) with electrons and holes and scatter it. As the temperature increases the phonon concentration increases resulting in more scattering and a decrease in the mobility. This is known as lattice (phonon) scattering.

Impurity scattering also effects the mobility. Doped semiconductor materials with acceptors or donors which are ionized and therefore charged. The Coulombic force will deflect electrons or holes which approach an impurity. Thus as the temperature decreases, the impurity scattering increases and this results in a decrease in the mobility. This is observed in figure 7.3. The mobility is proportional to $T^{-3/2}$ [2].

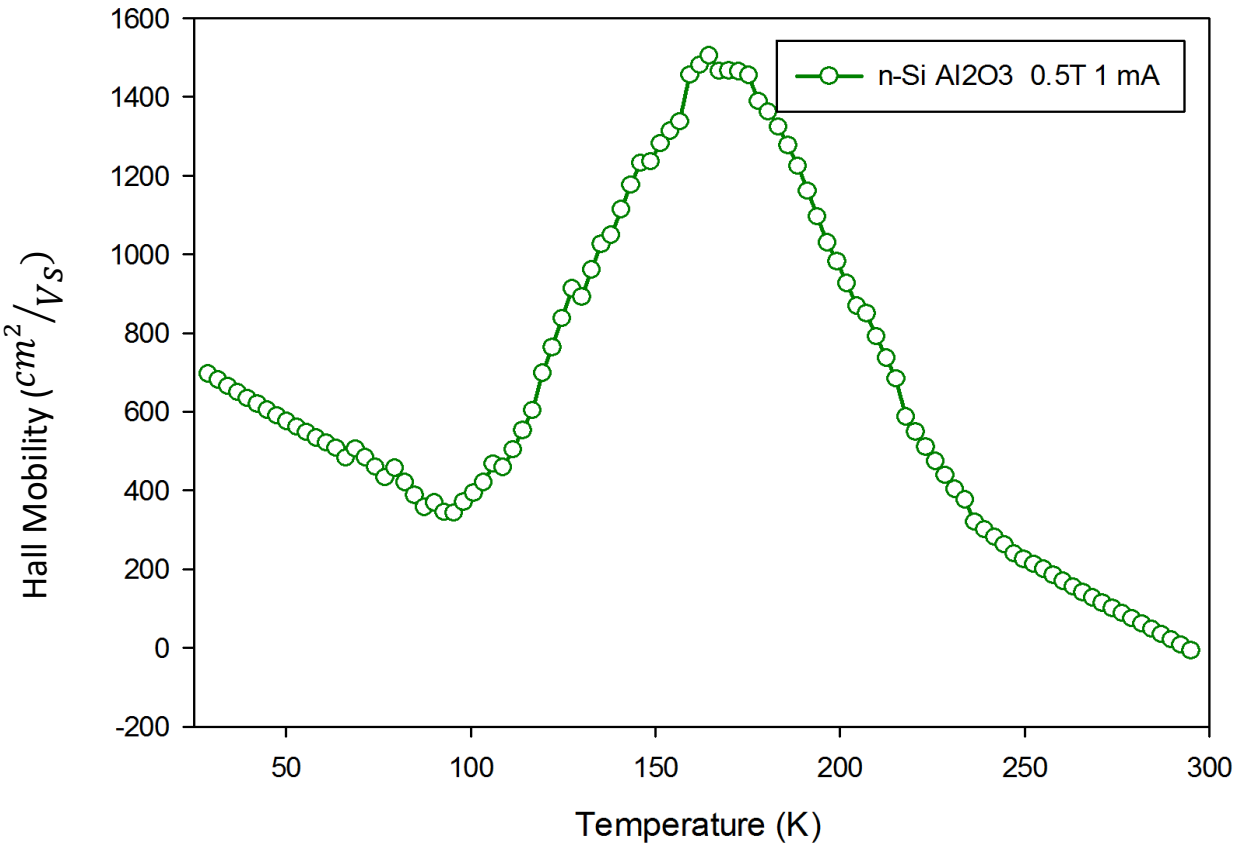

Figure 7.3: The hall mobility vs Temperature for studied n-Si with Al_2O_3 sample from 30 K to 300 K.

The next sample measured was PEDOT:PSS on glass to allow higher currents through the sample. Hall mobility measurements in the 10^{-1} $cm^2(Vs)^{-1}$ range were measured for temperatures above 100 K. The Hall mobility as a function of temperature is shown in figure 7.4 below.

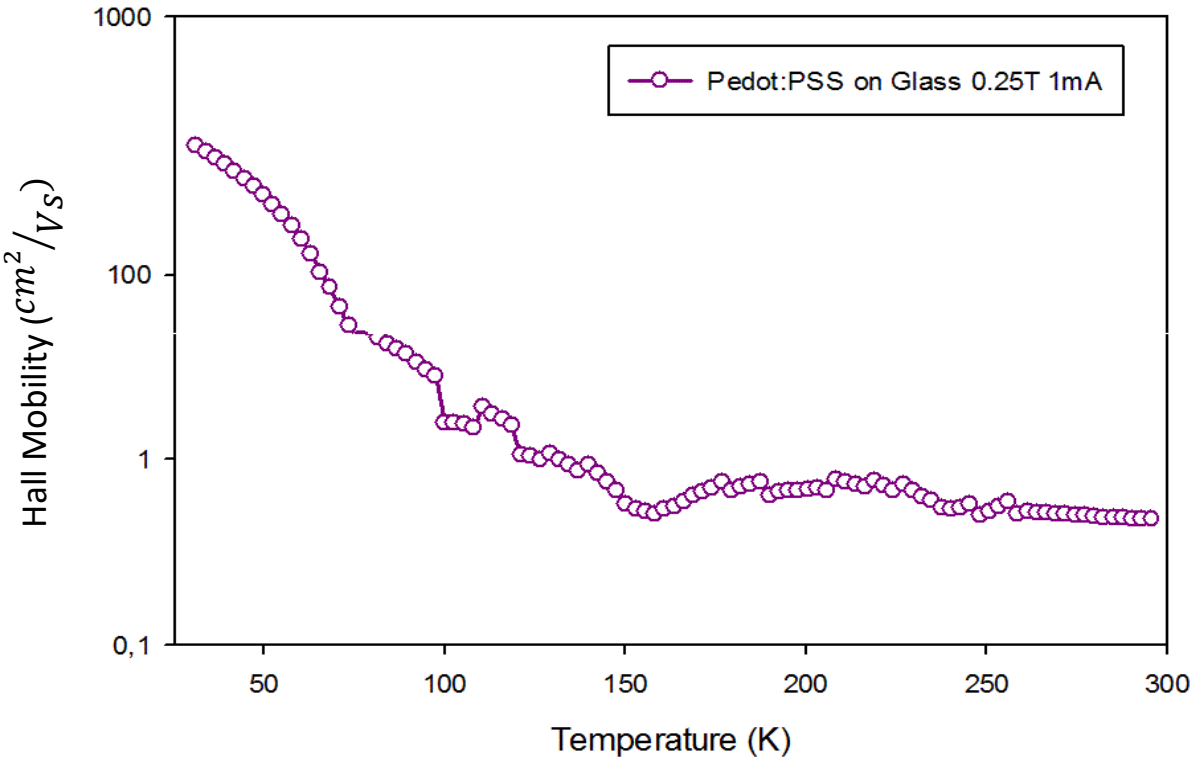

Figure 7.4: The hall mobility vs Temperature for studied n-Si with PEDOT:PSS 100 nm layer sample from 30 K to 300 K. PEDOT:PSS has a mobility of 0.7 $cm^2(Vs)^{-1}$ at 300 K.

The next samples are GaAs p-type and n-type. Due to the dependence of the effective mass of the mobility. The electron mobility is greater than the hole mobility for a given impurity concertation. This is shown in figure 7.5 and 7.6. GaAs is a polar semiconductor material and thus optical-phonon scattering is significant. Impurity scattering is typically only seen at lower temperatures [27]. The mobility of p-type GaAs at 300 K is approximately 1.2×10^2 $cm^2(Vs)^{-1}$ and the mobility of the n-type GaAs at 300 K is 2.7×10^4 $cm^2(Vs)^{-1}$. At 300 K it can be seen that the p-type and n-type hall mobility differs with a factor of approximately 100.

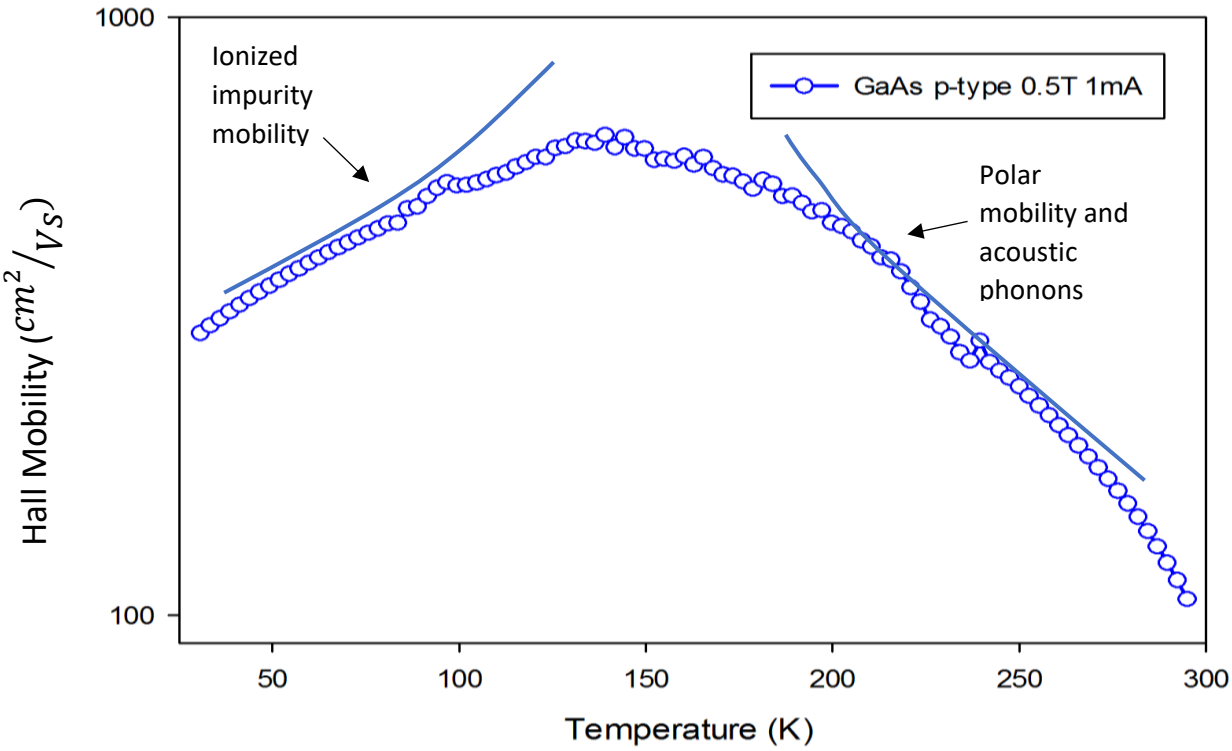

Figure 7.5: The hall mobility vs Temperature for studied p-type GaAs sample from 30 K to 300 K. With a Hall mobility of 1.2×10^2 $cm^2(Vs)^{-1}$ at 300 K.

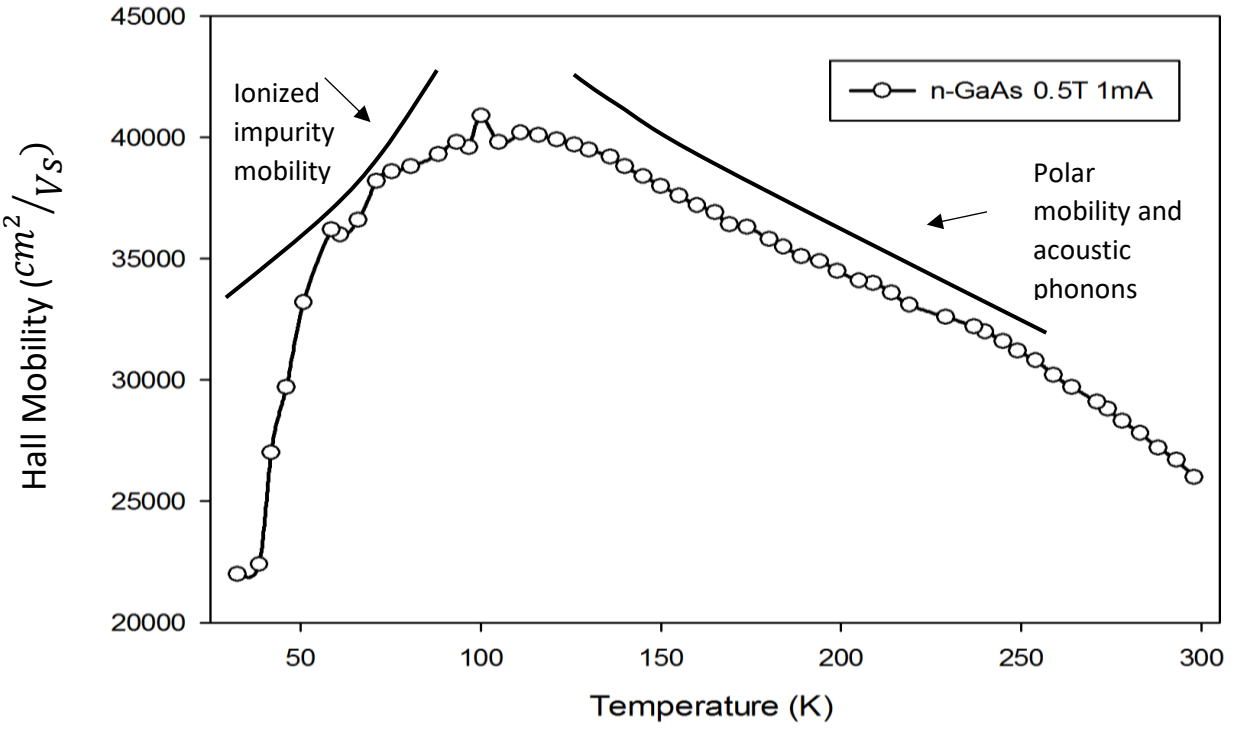

Figure 7.6: The hall mobility vs Temperature for studied n-type GaAs sample from 30 K to 300 K. With a Hall mobility of 2.7×10^4 $cm^2(Vs)^{-1}$ at 300 K.

Carrier Concentration:

The carrier concentration in a semiconductor is temperature dependent. The intrinsic carrier concertation is given by equation 2.12 and can be expanded by the following formula

$$n_i = 2[\frac{2\pi kT}{h^2}]^{\frac{3}{2}}(m_n m_p)^{\frac{3}{4}} e^{(\frac{-E_g}{2kT})} \quad 7.4$$

where the exponential temperature dependence is the dominant. At very low temperatures, very low concertation of intrinsic electron-hole pairs exist and donor electrons are bound to the donor atoms. This region is known as the freeze-out or ionization region. Within a doped material, as the temperature is raised, increasing ionization occurs, and at approximately 100 K all the donor atoms are ionized [27]. At this point the carrier concertation is determined by doping. The extrinsic region also known as the saturation region, is the region where every available dopant has been ionized. Within this region as the temperature increases the carrier concertation does not change. At high temperatures the intrinsic carriers thermally generated are dominant and outnumber the dopants. Within the intrinsic region the carrier concertation increases as the temperature increases.

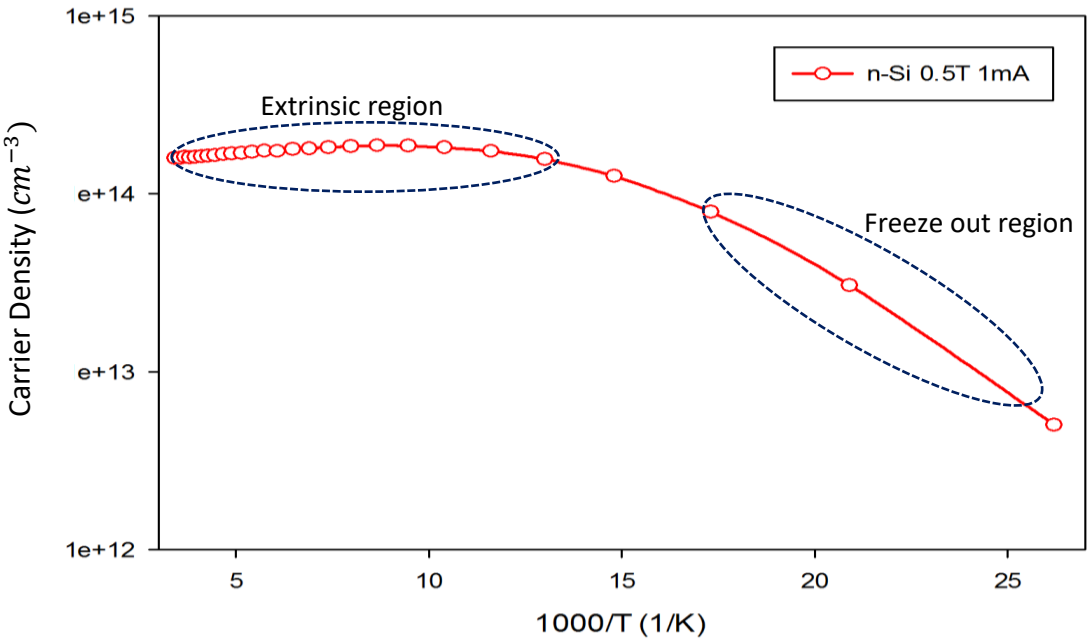

Figure 7.7: The carrier density vs reciprocal of the temperature for studied n-Si sample from 30 K to 300 K. With freeze out region below 100 K and a saturation region from 100 K to 300 K with a carrier density of $n \sim 10^{14}$ cm^{-3}.

The next sample which is the same n-Si as previous with a Al_2O_3 layer shows a freeze out region from 35 K and a saturation carrier density of $n \sim 10^{17}$ cm^{-3}. As the sample reaches temperatures above 200 K the sample is in the intrinsic region. In this region the carrier density increases as the temperature increases. For Al_2O_3 from 200 K to 300 K the carrier density increases by a factor of 10 from $n \sim 10^{17}$ to $n \sim 10^{18}$ cm^{-3}. This is shown in figure 7.8.

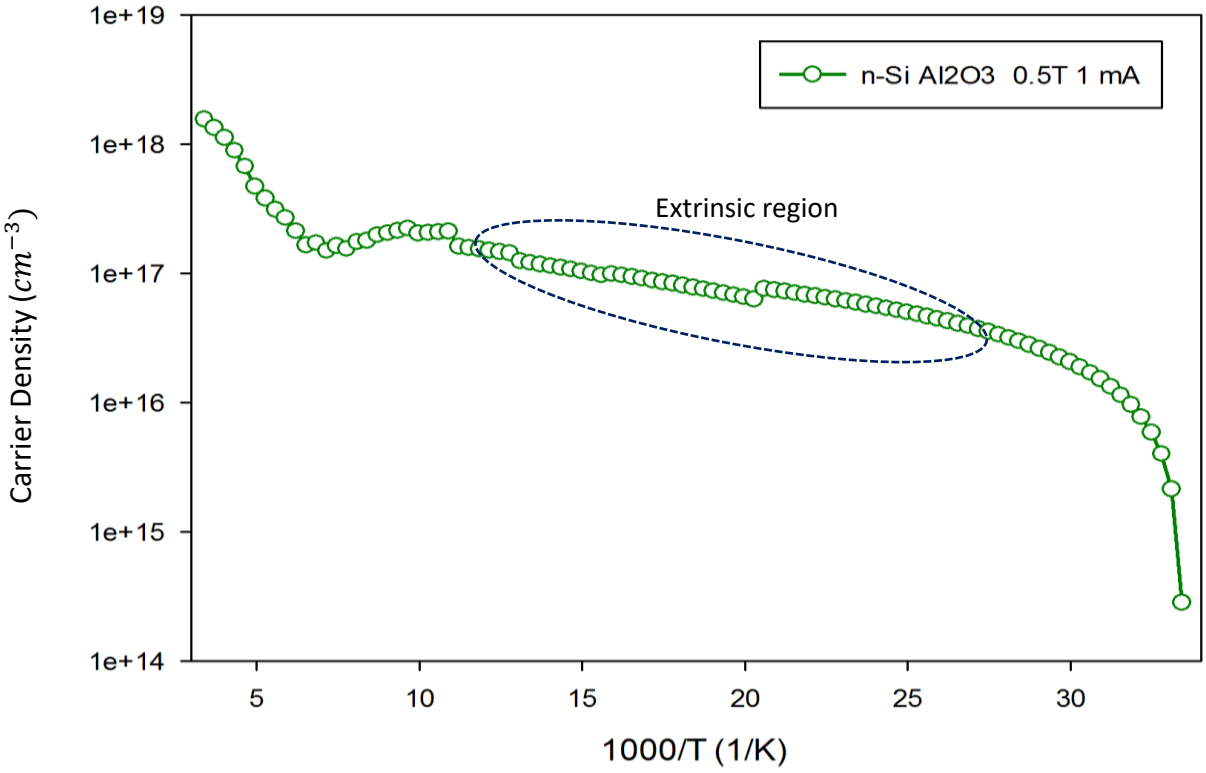

Figure 7.8: The carrier density vs reciprocal of the temperature for studied sample n-Si with Al_2O_3 from 30 K to 300 K. A carrier density of 10^{18} cm^{-3} was measured at 300 K.

The PEDOT:PSS sample shown in the figure 7.9 has a carrier density at 300 K of approximately 9.7×10^{21} cm^{-3}. This value corresponds to recent studies done on the properties of PEDOT:PSS. This high carrier concentration at room temperature is another reason PEDOT:PSS is such a popular p-type conducting polymer material used for electronic applications such as photovoltaic cells. This high concertation may also be the reason for the low mobility seen in figure 7.4 due to impurity scattering.

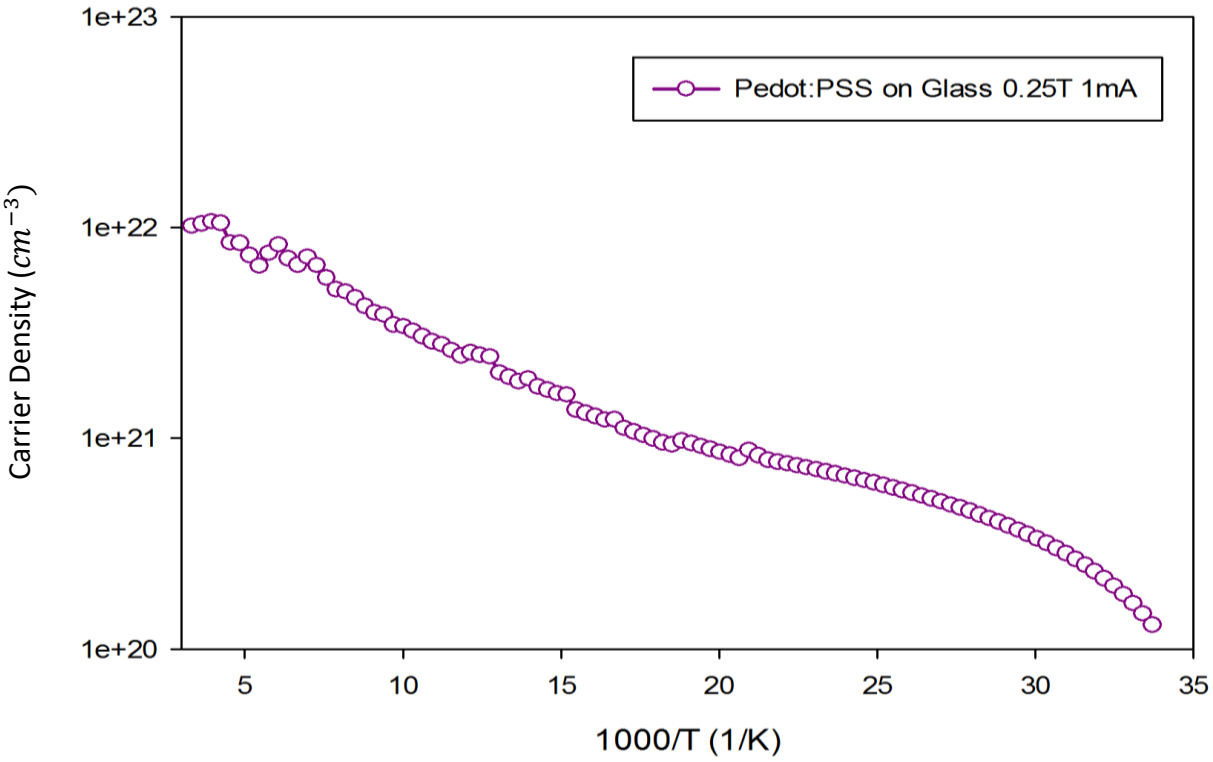

Figure 7.9: The carrier density vs reciprocal of the temperature for studied sample PEDOT:PSS layer of 100 nm from 30 K to 300 K. A carrier density of 10^{21} cm^{-3} was measured at 300 K.

The final two samples are the n-and p-type GaAs samples. The carrier density of the p-type GaAs at room temperature is approximately $p \sim 10^{16}$ cm^{-3} and the carrier density for the n-type is $n \sim 10^{15}$ cm^{-3}. From figures 7.10 and 7.11 the ionization region for p-type and n-type GaAs respectively are 30 K and below 30 K. The ionization region for the n-type GaAs was not observed since the temperature to reach this region is below 25 K, thus outside the capabilities of the equipment used in this experiment. The carrier density at the extrinsic region for the p and n-type were $p \sim 10^{15}\ cm^{-3}$ and $n \sim 10^{14}\ cm^{-3}$ respectively. The intrinsic region was reached for the n-type GaAs at 220 K. For temperatures from 220 K and higher the carrier density greatly increased as illustrated in figure 7.11.

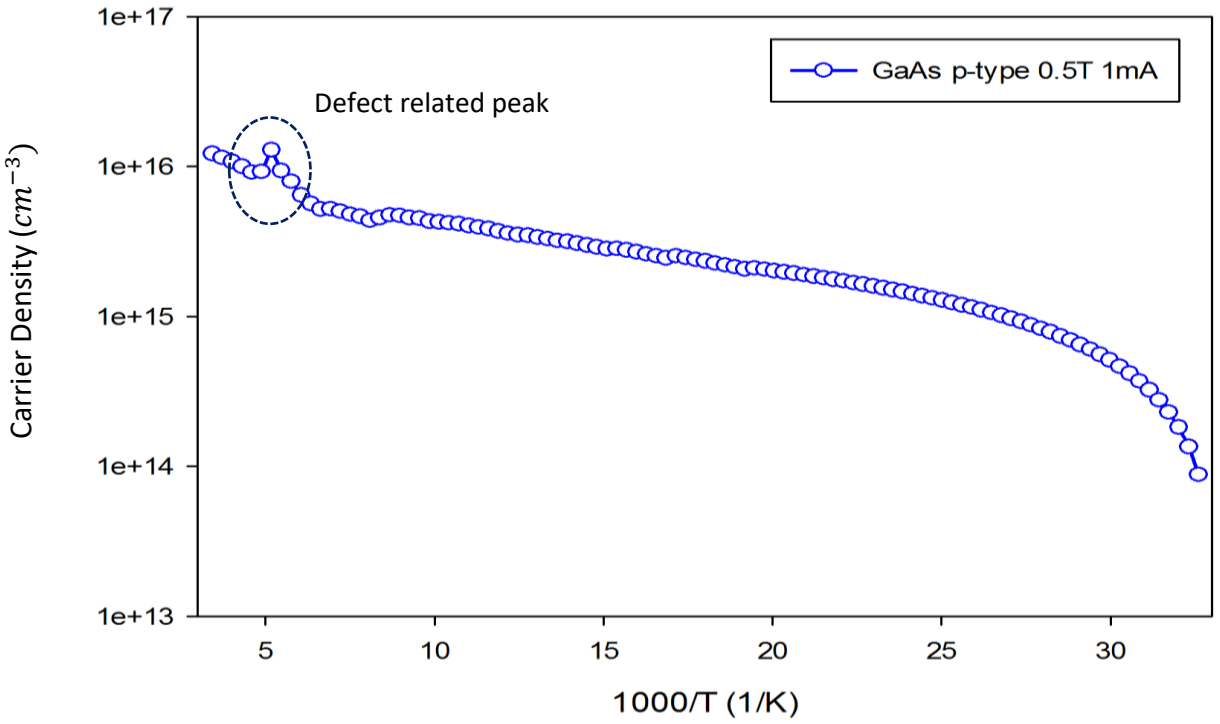

Figure 7.10: The carrier density vs reciprocal of the temperature for studied sample p-type GaAs from 30 K to 300 K. The carrier density at 300 K is measured at $p \sim 10^{16}\ cm^{-3}$.

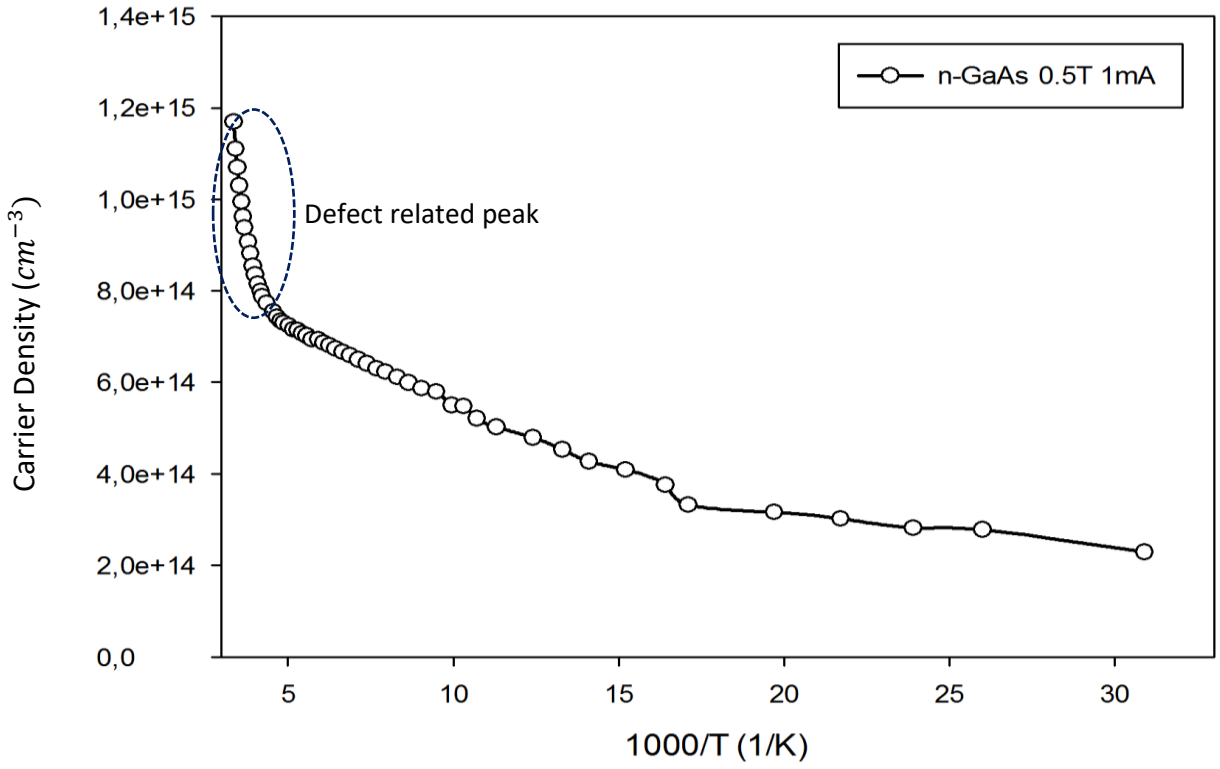

Figure 7.11: The carrier density vs reciprocal of the temperature for studied sample n-type GaAs from 30 K to 300 K. The carrier density at 300 K is measured at $n \sim 10^{15}\ cm^{-3}$.

Resistivity:

The resistivity which is the inverse of the conductivity is dependent on two factors as indicated by equation 7.5. First is the concentration of free carriers which are available to conduct current through the material and second their mobility which represents their freedom to move. The resistivity is given by:

$$\rho = \frac{1}{q[\mu_n(T)n(T) + \mu_p(T)\,p(T)]} \tag{7.5}$$

for an n-type material we can simplify the resistivity formula to

$$\rho = \frac{1}{q[\mu_n(T)n(T)]} \tag{7.6}$$

From what we know about conducting materials like metals is that their electrons are in the conduction band and are able to move freely within the lattice. This “sea” of electrons is what makes conduction possible. The opposite is true for insulator materials. In these materials the electrons are in the valance band and bound to the atom. Semiconductor materials behave like non-metals or insulator materials at low temperatures. The electrons are trapped in the valance band. However as the temperature increases the electrons gain sufficient energy to jump to the conduction band and move freely and behaves like a metal or conducting material. As the conduction increases due to temperature increase of the semiconductor materials, we know that the resistivity decreases. At high temperatures the semiconductor material behaves like a metal and at these high temperatures the resistivity increases with temperatures due to scattering, which is discussed in the mobility and carrier concertation sections.

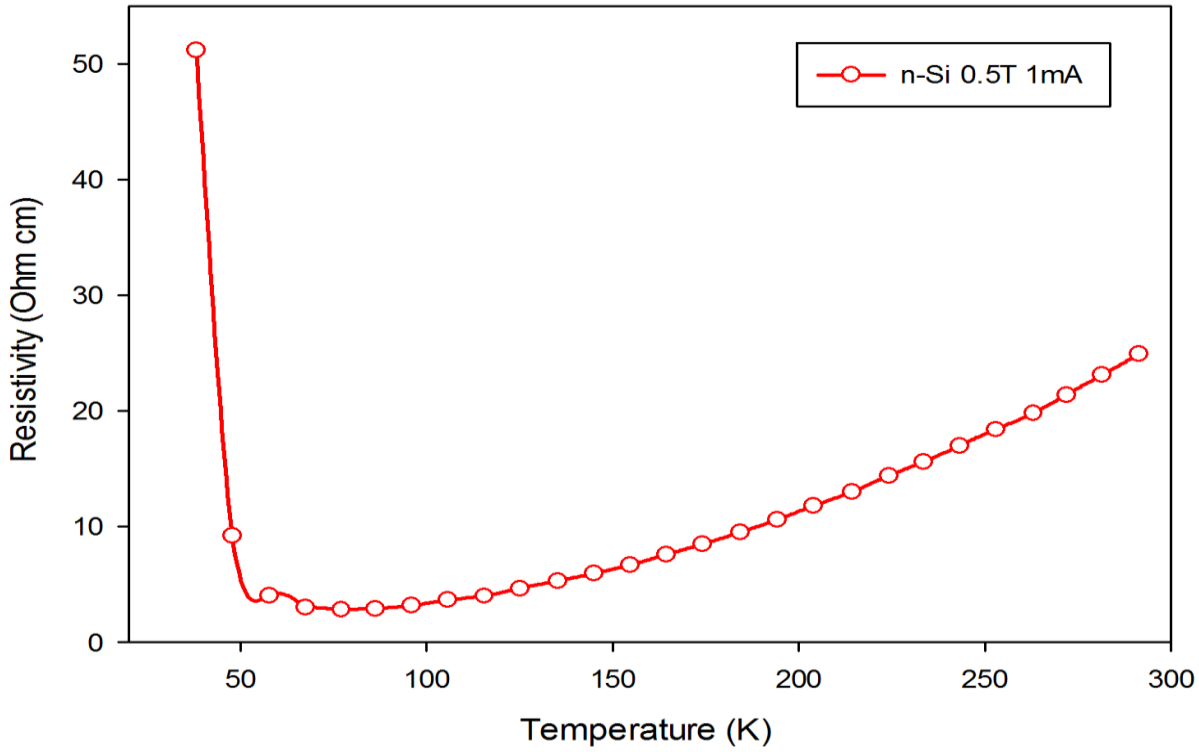

Figure 7.12: The Resistivity vs Temperature for studied n-Si sample from 30 K to 300 K. The behaviour of silicon in this temperature range perfectly illustrated the behaviour of a semiconductor. At very low temperatures the semiconductor acts as an insulator (30 K to 80 K). As the temperature increases the semiconductor act as a metal illustration conducting properties (80 K to 300 K). This is a result of the scattering mechanisms discussed earlier.

The resistivity as seen in figure 7.12 should be high at lower temperature below 50 K for Si. This is due to the fact that the carrier concentration is at a minimum in the freeze-out region. Even though the mobility is high the carrier concentration factor is dominant. From the measurements it is seen that the resistivity greatly decreases to a minimum just above 50 K at a value of approximately 2.5 Ohm.cm.

As the temperature is increased the resistivity also increases as seen in figure 7.12. Within the saturation region the carrier concentration does not change, however, as the temperature increases within this region the mobility decreases due to lattice and impurity scattering, this results in an increase in the resistivity.

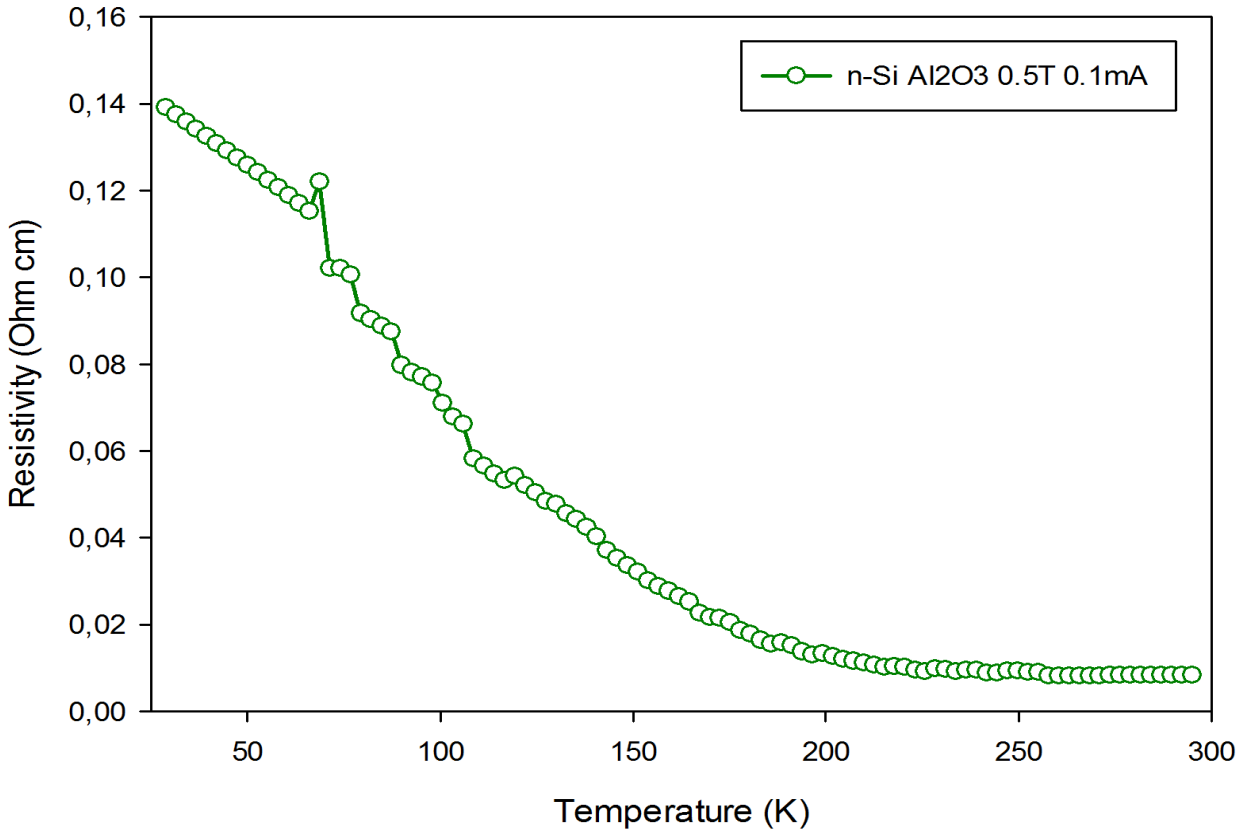

Figure 7.13: The Resistivity vs Temperature for studied n-Si with Al_2O_3 sample from 30 K to 300 K.

As seen from figure 7.14 the resistivity for PEDOT:PSS is low. If we compare this to the n-Si it has a much lower resistivity at room temperature. The resistivity is low approximately 10^{-3} Ohm.cm. At temperatures from 220 K and higher the resistivity is fairly constant. Due to the very low resistivity of this material at room temperature, is one more reason that makes this PEDOT:PSS a very promising material for organic solar cells.

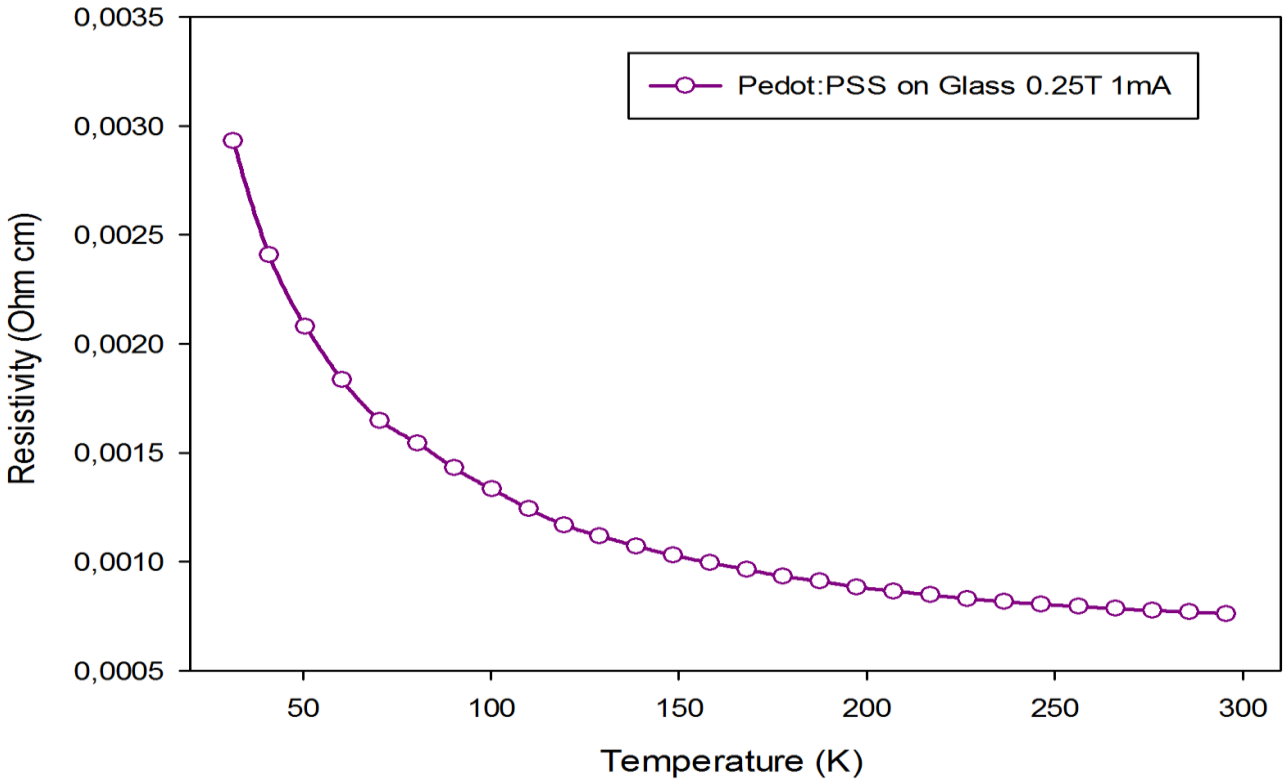

Figure 7.14: The Resistivity vs Temperature for studied n-Si with PEDOT:PSS layer spin coated on the sample from 30 K to 300 K.

Figures 7.15 and 7.16 represents the resistivity as a function of temperature for the p and n-type GaAs respectively. Both materials have the same resistive behaviour as a function of time. The p-type and n-type GaAs resistivities differ with a factor of approximately 10.

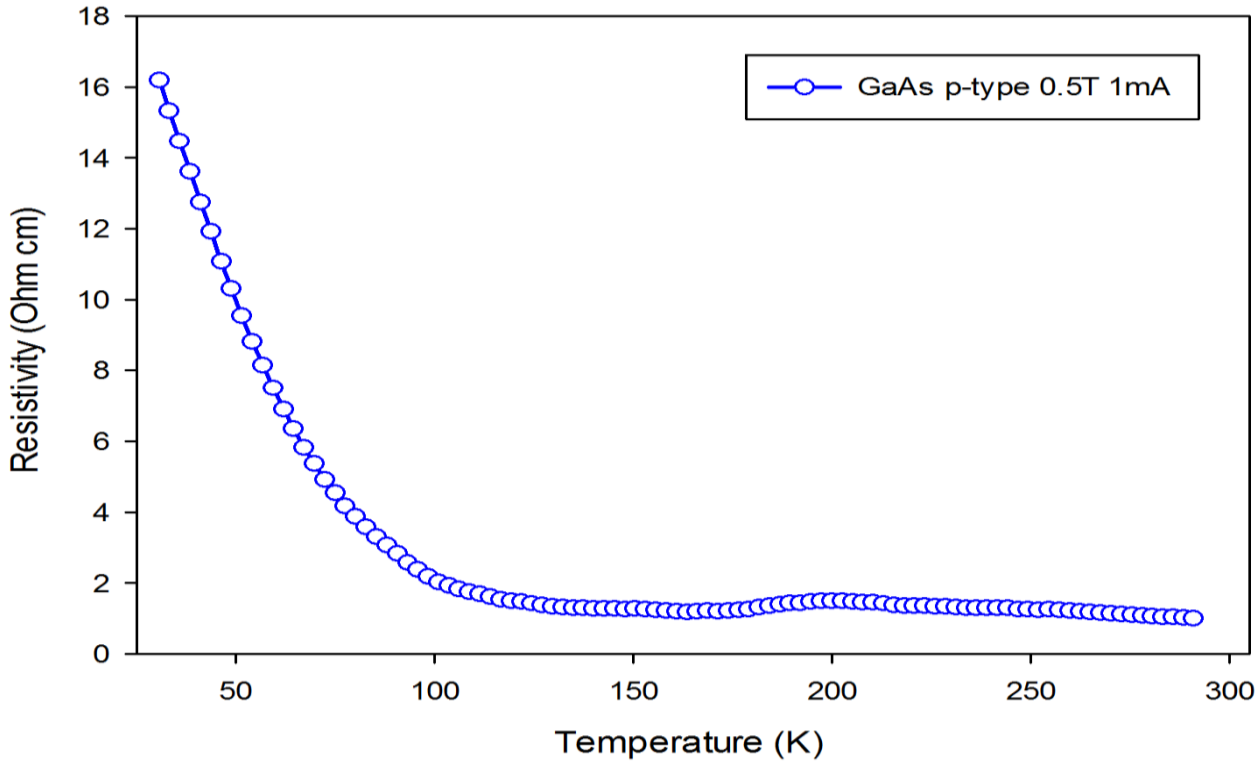

Figure 7.15: The Resistivity vs Temperature for studied p-type GaAs sample from 30 K to 300 K. A resistivity of order 10^0 Ohm.cm at 300 K.

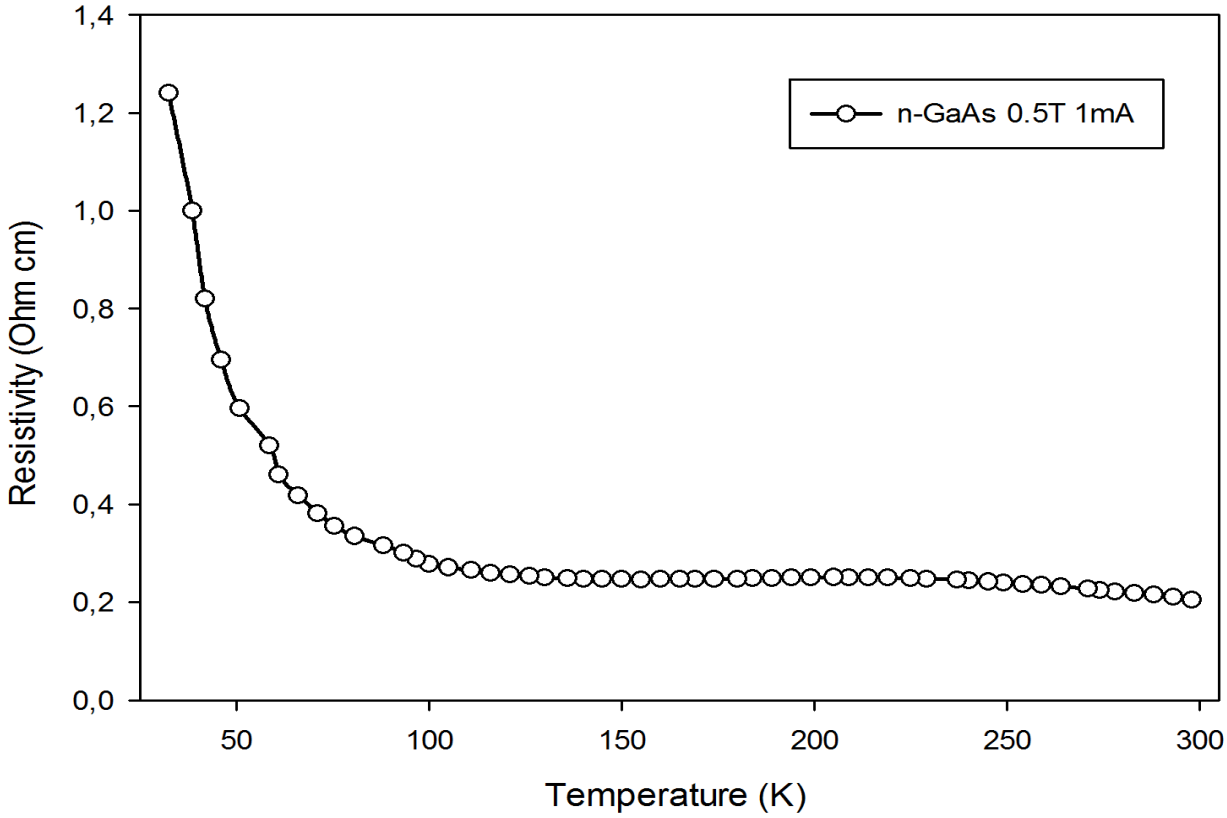

Figure 7.16: The Resistivity vs Temperature for studied n-type GaAs sample from 30 K to 300 K. The resistivity at 300 K is approximately $2x10^{-1}$ Ohm.cm.

7.2 *I-V* AND *C-V* MEASUREMENTS

The *I-V* and *C-V* measurements were done in a Faraday cage so as to isolate the samples from environmental factors such as noise and heat. The studied samples were the n-Si used to fabricate the solar cells and the perovskite solar cell sample. Measurement interval ranged from -2 V to 2 V at room temperature which was approximately 300 K.

7.2.1 *I-V* and *C-V* Measurements of n-Si

In this section n-Si was radiated for 0, 30 and 60 minute time intervals with alpha particles in the radiation lab. This was done to investigate the effect of this radiation on the electrical properties of the n-Si semiconductor material.

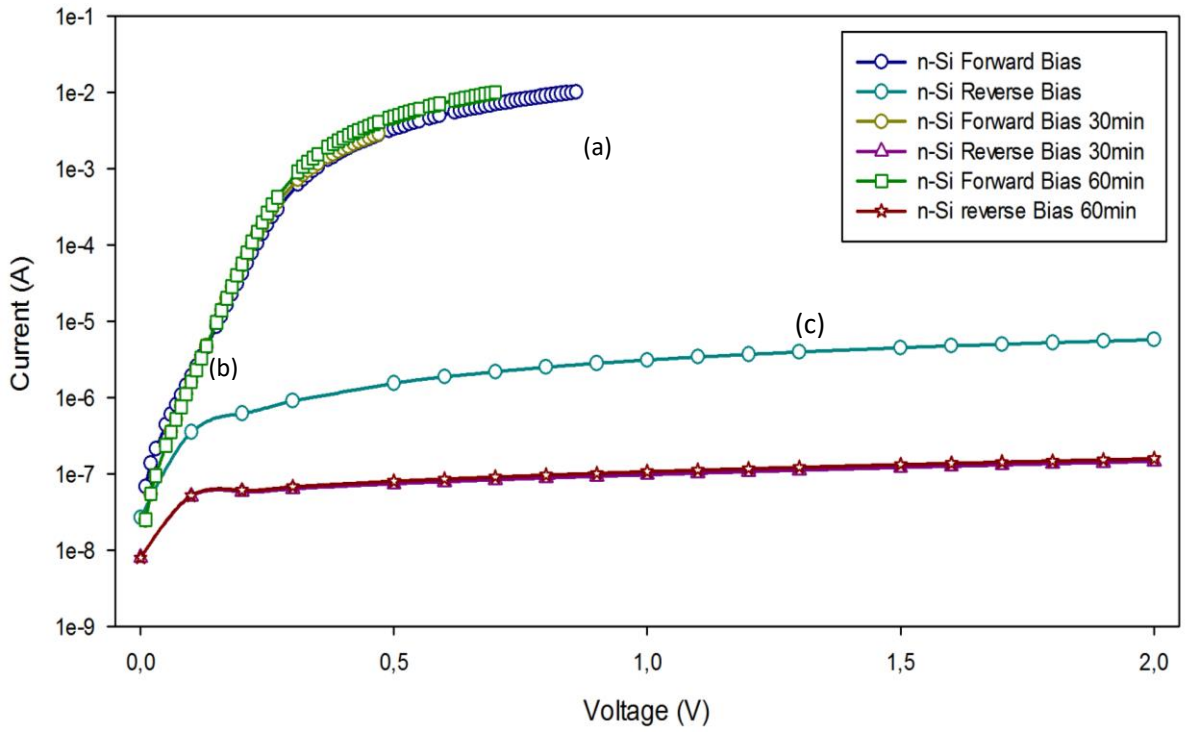

Figure 7.17: Current-Voltage characteristics of Si n-type Pd Schottky diode. Region a) Series resistance effect b) Diffusion current and c) is the reverse leakage current.

Table 7.1: Data obtained from LabVIEW program.

Sample Description	No Radiation	30 min Radiation (Alpha)	60 min Radiation (Alpha)
n	1,252	1,094	1,085
Is (A)	$82{,}66 \times 10^{-9}$	$47{,}42 \times 10^{-9}$	$44{,}37 \times 10^{-9}$
SBH (eV)	0,655	0,669	0,670
Series Resistance (Ohm)	58,101	57,418	34,516

In figure 1 and table 1 we can see that as the sample was radiated that the characteristics of the Schottky diode improved. As radiation duration increases for 0 to 60 min the series resistance decreases, and the ideality factor (n) approaches unity (n=1 is the ideal diode case). However after 60 minutes of radiation at the next interval (120 minutes) the sample was damaged and measurements were not possible. The capacitance per unit area is given by

$$C = \frac{dQ_c}{dV} = \frac{\varepsilon_S}{\sqrt{2}L_D}(\beta V_{bi} \mp \beta V - 2)^{-\frac{1}{2}} \tag{7.7}$$

where V_{bi} is the built in potential and the plus-minus sign is determined by the forward-reverse bias conditions. Using this equation we can obtain the impurity concentration of the substrate by plotting

$$\frac{1}{C^2} = \frac{2L_D^2}{\varepsilon_S^2}(\beta V_{bi} \mp \beta V - 2) \tag{7.8}$$

as a function of the voltage (V) the gradient is related to the impurity concentration (N_B)

$$\frac{d(\frac{1}{C^2})}{dV} = \frac{2}{q\varepsilon_S N_B} \tag{7.9}$$

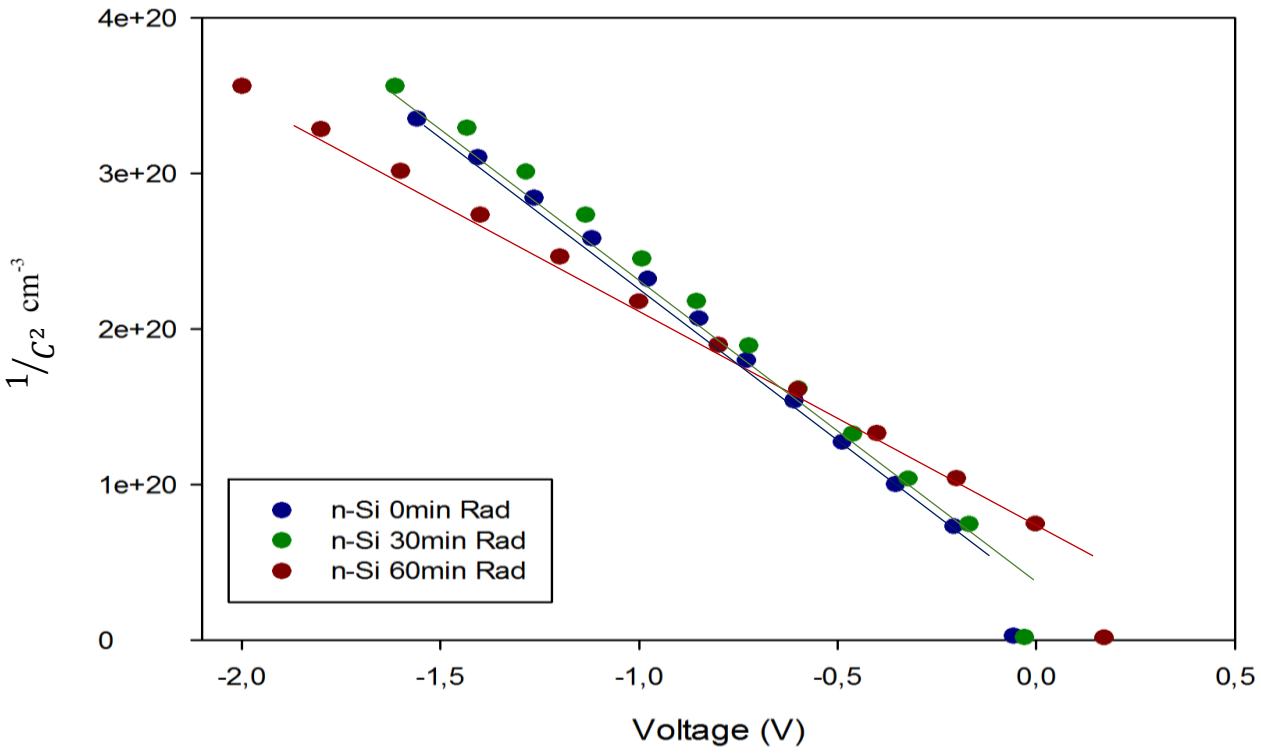

Figure 7.18: The capacitance-voltage relation for n-Si and the effect of radiation exposure for 0, 30 and 60 minutes.

From the relation between the gradient of the figure above and the impurity concentration it can be concluded that as the radiation duration increased from 0 to 30 min that the carrier concentration did not change and for the radiation from 30 min to 60 min that the impurity concentration increased.

7.2.2 I-V and C-V Measurement for Perovskite solar cell

We were not able to measure the capacitance-voltage measurements for the perovskite sample as the capacitance for forward and reverse bias were both 1 pF. This also indicates that DLTS is impossible. The *I-V* measurements we done for dark and illuminated conditions.

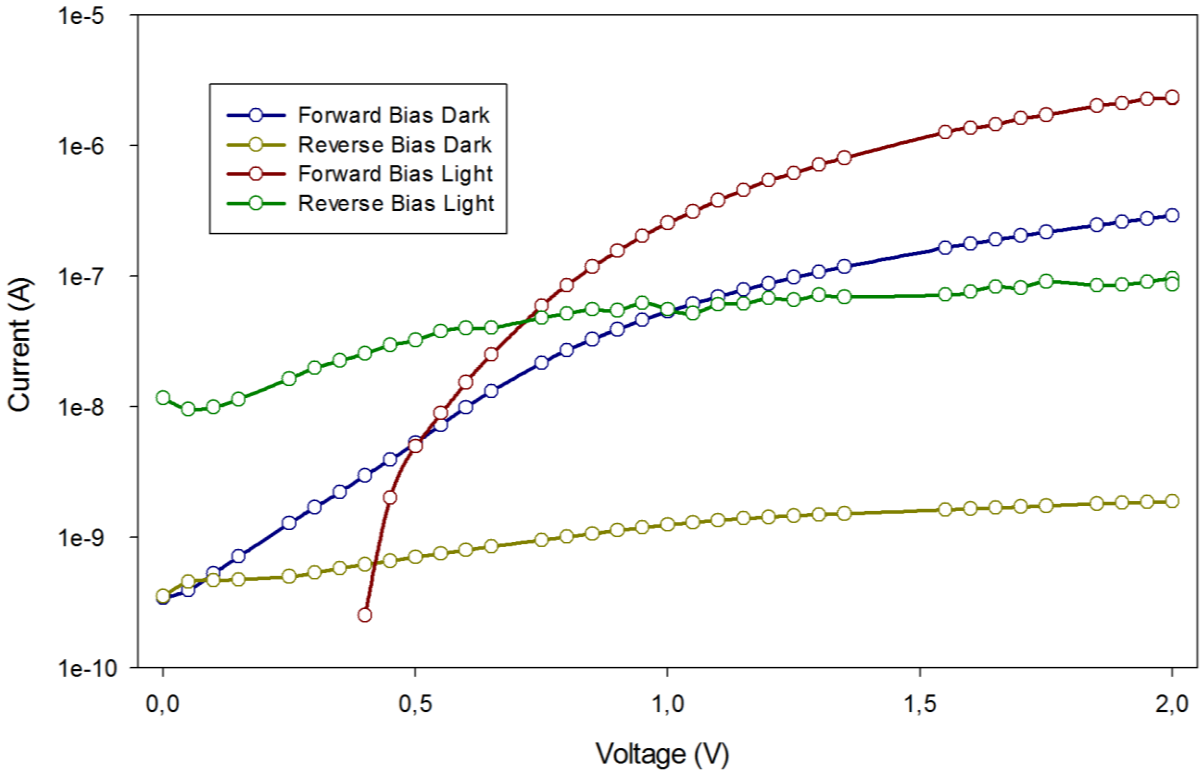

Figure 7.19: Current-Voltage characteristics of Perovskite MAPbBr3 p-type solar cell for light and dark conditions

The sample is a perovskite solar cell. This perovskite sample was the $MAPbBr_3$ with a band gap of 2.3 eV. Due to the high series resistance of the perovskite sample DLTS is impossible. A capacitance of 1 pF was measured in the *I-V* and *C-V* measurements.

7.2.3 *I-V* and *P-V* Measurements for n-Si/Pedot:PSS solar cell

The n-Si/PEDOT:PSS inversion layer solar cell was fabricated as discussed in chapter 3. The *I-V* and *P-V* measurements are shown below. The intensity was 1 sun and measurements were done from -0.5 V to 1 V in increments of 0.01 V with an average 3 measurements per increment. The green line represents the *I-V* curve and the red line represents the *P-V* curve.

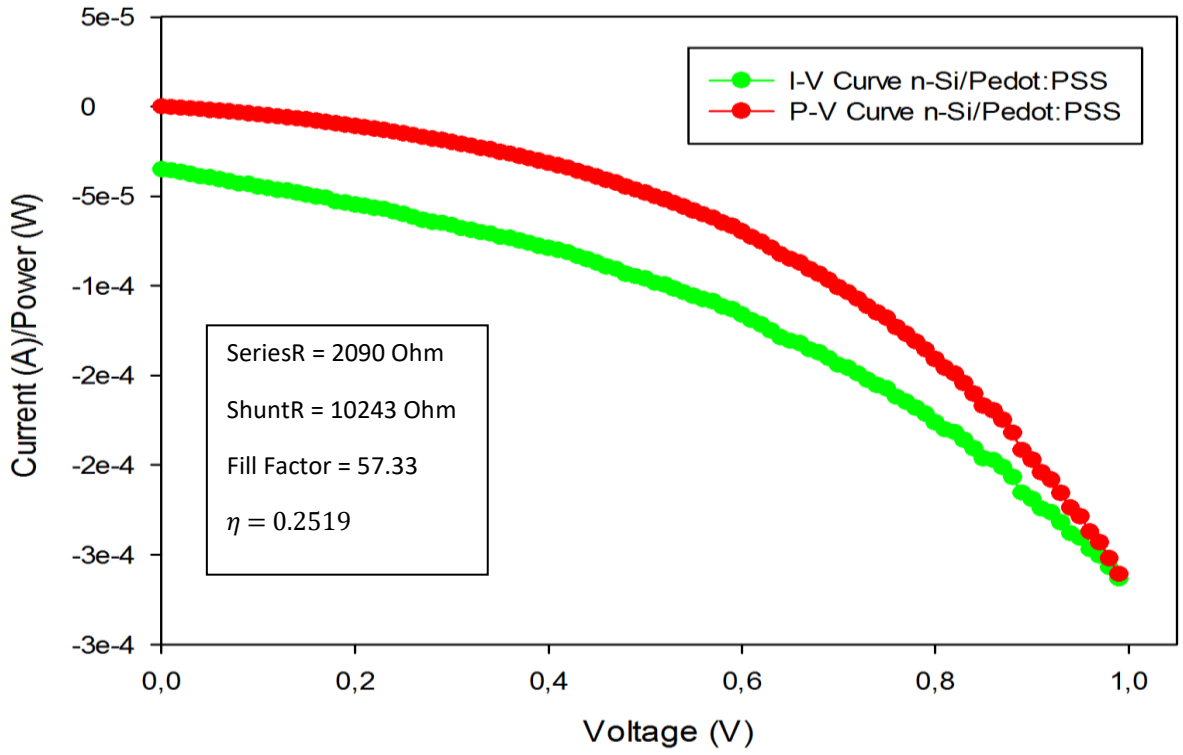

Figure 7.20: Current-Voltage and Power-Voltage characteristics of n-Si/PEDOT:PSS inversion layer solar cell.

7.3 P3HT:PCBM and PEDOT:PSS

The goal of this experiment is to compare the organic solar cells ZnO NRs P3HT:PCBM, ZnO NRs PEDOT:PSS and ZnO NRs control sample in terms of *I-V* characterization. This result will point us in the direction for further investigation.

7.3.1 Studied Sample

The cell structure of these sample are given in the figure below.

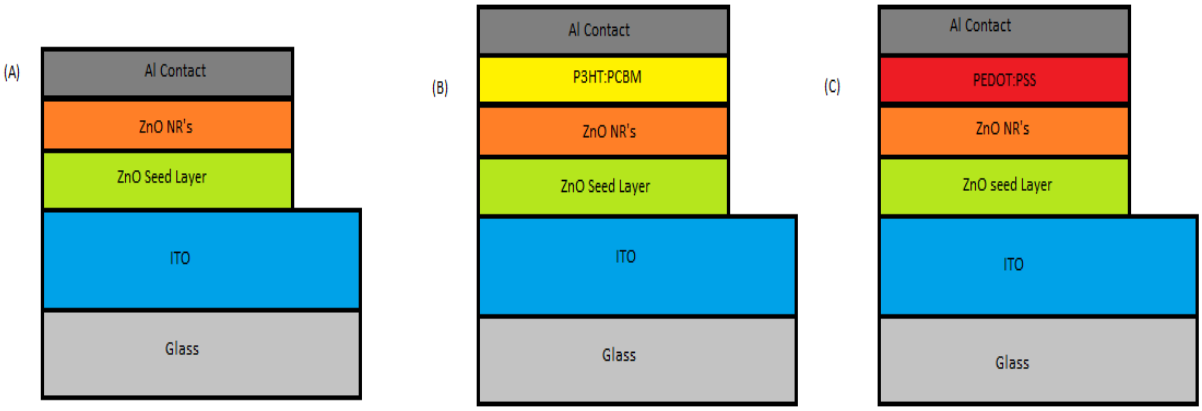

Figure 7.21: Schematic representation of solar cell structures.

7.3.2 *I-V* Measurements

The *I-V* characterization of a solar cell is one of the most important characterizations of the cell. A photovoltaic cell absorbs solar energy and generates electrical energy through a process called the photovoltaic effect. In this experiment the samples were illuminated under a concentration of 1 sun at AM1.5 (approximately 1000 W/m^2) by using a solar simulator (model: $Oriel^{®}\ LCS-100^{TM}$ Small Area Sol1A). An oscilloscope was also used and a potential difference was applied to each sample ranging from 0 V to 1 V in increments of 0.02 V and the current was measured. The execution of this experiment was automated and done by a LabVIEW program to reduce errors and obtain accurate measurements. Various parameters can be determined from these *I-V* curves such as the maximum power output, fill factor and efficiency of the cell. The *I-V* curves of the studied samples are given in table 7.2 and figure 7.22.

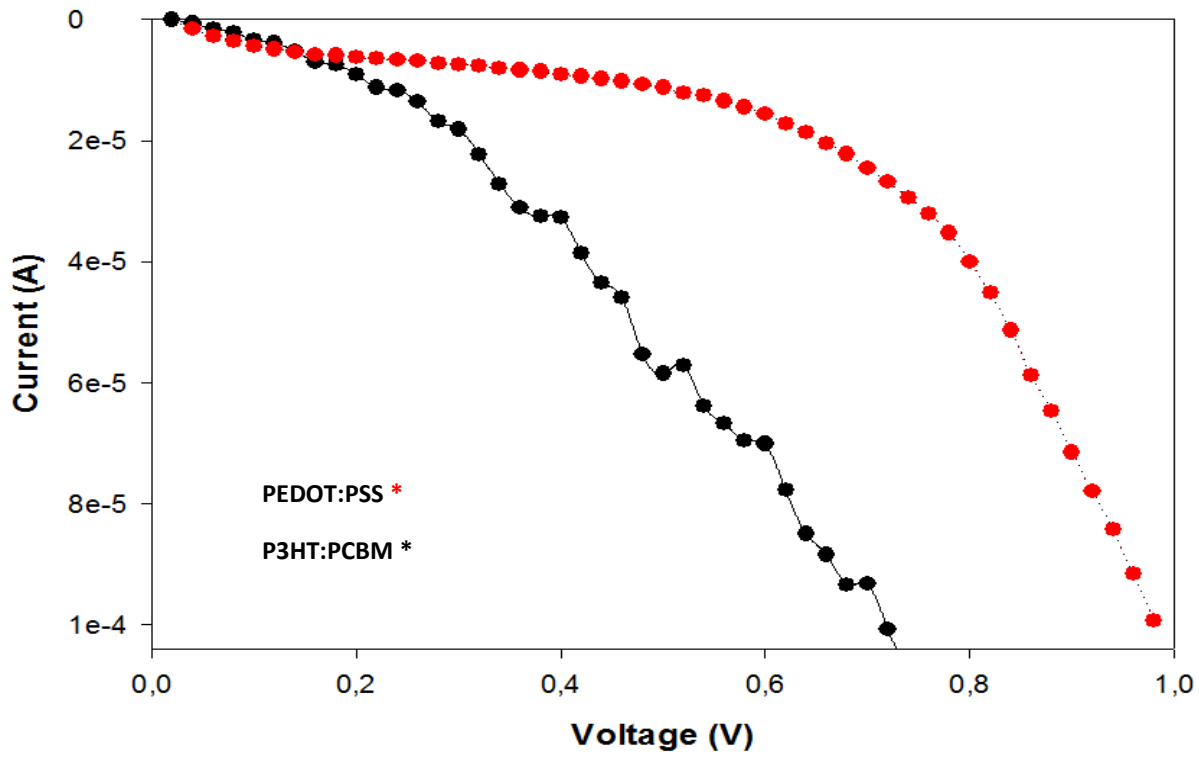

Figure 7.22: *I-V* curve of studies sample from a voltage of 0 to 1 V in increments of 0.02 V.

Table 7.2: *I-V* measurement results for studied samples.

Sample Description	Voc(V)	Fill Factor	Shunt resistance(Ω)	Series resistance(Ω)	Power(W)	Efficiency(%)
ZnO NRs Control	0.96	59.87	21275.101	2994.292	8.3E-5	0.0439
ZnO NRs P3HT PCBM	0.96	52.17	263947.31	30579.27	7.6E-6	0.003833
ZnO NRs PEDOT:PSS	0.96	57.37	50098.37	4074.23	1.95E-4	0.0975413

The current-voltage relation in the photovoltaic effect is given by the following equation:

$$I = I_l - I_0(e^{\frac{q(V+IR_S)}{nkT}} - 1) - \frac{V + IR_S}{R_{SH}} \qquad 7.10$$

for an ideal solar cell the shunt resistance should be as large as possible to restrict the current to a single flow path, and the series resistance should be as low as possible resulting in no voltage drop before the load. The main contributing factor to the series resistance are the metallic contacts, the contact between the material and the metallic contact. The main contributing factor to the shunt resistance is the impurities within the cell. By comparing the P3HT:PCBM sample to the control sample it is clear that the series resistance is extremely high and this is not favourable to the cells performance. Whereas the shunt resistance of the P3HT:PCBM is higher than each of the studied samples (control and PEDOT:PSS) and this is favourable to the cells performance.

The short circuit current corresponds to the short circuit condition when the impedance is low and it is calculated when the voltage is zero. Thus *I* (current) is equal to I_{SC} when the voltage is zero. For an ideal *PV* cell I_{SC} is equal to the total current produced in the *PV* cell by photon excitation. The open circuit voltage is the voltage than occurs when there is no current passing through the cell, and is also the maximum potential difference across the cell for a forward-bias sweep within the power quadrant.

Another important factor is the fill factor which is the quantity is obtained by comparing the maximum measured power with the theoretical power.

$$FF = \frac{I_{MP}V_{MP}}{I_{SC}V_{OC}} \qquad 7.11$$

the average fill factor ranges from 50 % to 80 %. As we can see from the data the ZnO NRs control has the highest fill factor at 59.87 and is thus the most favourable in terms of this ratio between the maximum power output measured and the theoretical maximum power. The ZnO NRs P3BHT PCBM sample is not far behind with a fill factor of 57.17.

CHAPTER 8

CONCLUSION

TDH measurements n-type Si, n-Si with Al_2O_3, Pedot:PSS and GaAs

If we consider these materials for the manufacture of solar cells there are three main factors to consider. Efficiency, Cost and longevity (Sustainability). n-Si is a strong durable materials with high efficiency but solar cell fabrication cost is also high. GaAs materials are more efficient than Si, however, the cost of GaAs, if compared to Si, is approximately 1000 % more expensive which destroys the chance for commercial solar power usage. PEDOT:PSS is cheap, efficient but longevity at this point is very low. The following table sums of the *TDH* measurements of these materials at 300 K. The temperature dependence of these parameters can be seen in chapter 7.

Table 8.1: Summary of TDH measurements done in this study at 300 K.

Material	Hall Mobility ($cm^2(Vs)^{-1}$)	Carrier Density (cm^{-3})	Resistivity (Ohm.cm)	Pros	Cons
n-Si	10^3	10^{15}	10^1	Efficiency Longevity	Cost
Pedot:PSS	10^{-1}	10^{21}	10^{-3}	Cost	Longevity
Al_2O_3	10^1	10^{18}	10^{-2}	Longevity	Cost
p-GaAs	10^2	10^{16}	10^0	Efficiency Longevity	Cost
n-GaAs	10^4	10^{15}	10^{-1}	Efficiency Longevity	Cost

The *TDH* measurement is a very effective technique to measure important properties of semiconductor materials and the dependence of temperature of these properties.

n-Si *I-V* and *C-V* measurements

Electrical characterization was also performed on an n-Si sample. These measurements include an *I-V* measurement and a *C-V* measurement. The sample was measured at 0, 30 and 60 minutes under the influence of alpha radiation to measure the effect of alpha radiation on the materials characteristics. Figure 7.17 and figure 7.18 illustrates the *I-V* and *C-V* graph respectively under the influence of radiation. Under the influence of alpha radiation the *I-V* indicates that the n-Si improves. Under no radiation the ideality factor is 1.252 and after 30 minutes irradiation with alpha-particles, the ideality factor is 1.094. Long exposure to radiation however resulted in the destruction of the semiconductor material.

n-Si/PEDOT:PSS solar cell *I-V*

A n-Si/PEDOT:PSS inversion solar cell was manufactured by spin coating and a resistive deposition techniques. More details are discussed in chapter 3 and 6. The *I-V* and *P-V* measurements of this solar cell is illustrated by figure 7.20. The efficiency of this solar cell was calculated at 0.2519 % and a fill factor of 57,33. The n-Si/PEDOT:PSS solar cell is a inorganic-organic solar cell. By using Si the highly efficient benefits of Si is still obtained and the manufacturing techniques such as spin coating to apply the PEDOT:PSS layer reduces the cost of fabrication. This results in a moderately high efficient low cost solar cell. Record high efficiency of 12 % Si/PEDOT:PSS solar cells have been produced [31].

PH3T:PCBM and PEDOT:PSS

PH3T:PCBM and PEDOT:PSS are conducting polymers. In recent years new cheaper methods to fabricate solar cells have been under great study. With ZnO nano rods the organic solar cells were fabricated and *I-V* measurements were done. The results are illustrated in figure 7.22. PEDOT:PSS solar cell measured a efficiency of 0.097 and P3HT:PCBM measured an efficiency of 0.003. Organic solar cells as compared to other solar cell in types today's age have lower efficiencies however the cost to fabricate are very low making them a promising branch of solar cells.

REFERENCES

[1] UDT Sensors, Silicon Photodiodes-Physics and Technology, April 1982.

[2] M. Zeman, Introduction to Photovoltaic solar energy, Delft University of Technology

[3] A. Abudulimu, Measuring the efficiency and charge carrier mobility of organic solar cells, Umea university, Sweden, 2012

[4] O. Isabella, A.H.M Smets, M. Zeman, Solar Energy-Fundamentals, Technology and Systems, Delft University of Technology, 2014

[5] M. Johnsson, P. Lemmens, Crystallography and Chemistry of Perovskites, Phys. For Condensed Matter, Braunschweig, Germany, 1998

[6] A.D. Lozano-Gorrin, Structural Characterization of New Perovskites, Universidad de La Laguna, Spain, 2003

[7] S.A. Goodman, The characterization of GaAs and AlGaAs by the Hall effect, MSc dissertation, University of Port Elizabeth, 1989

[8] D.K. Schroder, Semiconductor Material and Device Characterization, Arizona State University, Canada, 1998

[9] S.M. Sze, Physics of semiconductor devices, Bell Laboratories Murray Hill, New Jersey, 1981

[10] www.ni.com/Photovoltaic cell I-V Characterization theory and LabVIEW Analysis Code/ 25/03/2016, May 2012

[11] H. Desilvestro, What Physical Factors Affect Current-Voltage Characteristics of Dye solar cells, Dyesol Ltd, 2008

[12] Z. Dilli, Intrinsic and extrinsic semiconductors, Fermi-dirac distribution function, the Fermi level and carrier concentration, 2008

[13] D. Pearman, Electrical Characterization and modelling of Schottky barrier metal source/drain MOSFETs, University of Warwick, 2007

[14] www.NEED.org/HowSolarCellsWork, 2011

[15] A.M. Bagher, M.M.A. Vahid, M. Mohsen, Types of Solar Cells and Application, American Journal of Optics and Photonics, pp. 94-113, 2015

[16] K. Feron, W.J. Belcher, C.J. Fell, Organic Solar Cells: Understanding the Role of Forster Resonance Energy Transfer, CSIRO Energy Technology, Newcastle, Australia, 2012

[17] M. Eslamian, J.E. Newton, Spray-on PEDOT:PSS and P3HT:PCBM thin film for polymer solar cells, School of Engineering and computing sciences,Texas ,USA, 2014

[18] V.Shrotriya, G. Li, Y. Yao, Accurate Measurement and characterization of Organic Solar Cells,National Renewable Energy Laboratory, USA, 2006

[19] G.H. Kassier, The characterization of bulk as-grown and annealed ZnO by the Hall effect, University of Pretoria, 2006

[20] E.M.G. Rodrigues, V.M.F. Mendes, Simulation of a Solar Cell considering Dingle-Diode Equivalent Circuit Model, University of Beira Interior, 2012

[21] M. Bashahu, P. Nkundabakura, Solar Energy, 81, 2007

[22] P. Hersch, K. Zweibel, Basic Photovoltaic Principles and Methods, U.S Department of Energy, February 1982

[23] P.K. Nayak, J. Bisquert, D. Cahen, Assessing Possibilities and limits for Solar cells, Dept. of materials and interfaces, Weizmann, Isreal, 2011

[24] D. Cahen, J. Berry, T. Buonassisi, Hybrid Organic-Inorganic Perovskites(HOIPs): Opportunities and Challenges, 2015

[25] W. E. Meyer, Digital DLTS studies on radiation induced defects in Si,GaAs and GaN, University of Pretoria, 2006

[26] M. Lay, D. Hoxley, Deep-Level Transient Spectroscopy, Part 3 Labs, 2004

[27] A. Shakouri, Temperature Dependence of Semiconductor Conductivity, University of California Jack Baskin school of Engineering, 2004

[28] N.J. Jeon, J.H. Noh, W.S. Yang, Compositional engineering of perovskite materials for high-performance solar cells,2015

[29] K. Galkowski, A. Mitioglu, Deterination of the exciton binding energy and effective masses for the methyl-ammonium and formamidinium lead tri-halide perovskite family, Royal society of Chemistry,2015

[30] A.A. Zhumekenov, M.I. Saidaminov, Formamidinium lead Halide Perovskite crystals with unprecedented long carrier dynamics and diffusion length, Department of Chemistry, Mansoura University, Egypt, 2016

[31] K.A. Nagamatsu,S. Avasthi, J. Jhaveri, A 12% Efficient Silicon/PEDOT:PSS Heterojunction Solar Cell fabricated at <100C , IEEE Journal of Photovoltaics vol 4. NO1, 2014